Product Development Team
for
NEXRAD Algorithms

Quarterly Report – 4th Quarter FY 03

03.6.2 Polarization and Frequency Diversity

Algorithms based on polarimetry will meet the aviation needs for information about the volumetric extent of hail, freezing rain, snow, and icing conditions, as well as non-hydrometeor scatterers. The biggest potential payoff is enhanced data quality. For all practical purposes, polarimetric techniques will eliminate problems associated with sea-clutter, ground clutter, AP, and biological scatterers.

a) Current Efforts

(NSSL):

HCA development continues. Most of this work appears as appendices to this report. Appendix A contains the latest, complete description of the NSSL HCA, which fulfills deliverables 03.6.2.E6 and part of 03.6.2.E10 (recent progress on HCA). Appendix B contains a complete description of the sea-clutter elimination algorithm and fulfills requirements for deliverable 03.6.2.E13 (classification in marine environments). Appendix C contains a report on spectral whitening with range to improve spectrum moment estimation, which fulfills deliverable 03.6.2.E5.

(NCAR):

03.6.2.10 Winter storm case studies.

Analyses of video disdrometer observations collected from 11 events with snow and mixed-phase precipitation is continuing. The dataset includes temperature, dew point, wind, precipitation rate, and visibility data. A number of events have been selected for anaysis. Calibration procedures have been established to improve the disdrometer estimates of particle size, axis ratios, and terminal velocities.

Rain-snow discrimination and freezing rain detection is facil- itated by knowing if a freezing or melting layer exists. Also, hydrometer classification requires that the freezing level be known. NCAR's freezing level algorithm was upgraded to make it sensitive to changes in precipitation intensity. Early versions assumed fixed height depressions for the maximum melting layer signatures from the 0C level. In truth, the depressions increase as precipiation intensity increases. The upgrade is described in the report 03.6.2.E12 (below).

Freezing level designations can be made with an accuracy of 100-200m. Algorithm performance is described in a report in preparation which should be available shortly.

A report on progress entitled "Winter Storm Studies: Video Disdrometer Measurements" (Appendix D) is attached, which completes deliverable 03.6.2.E10.

03.6.2.11 Improved hail detection with NCAR's S-Pol radar.

Results from a field program conducted in Florida (PRECIP98) revealed that the raindrop size distributions were on occasion dominated by small drops. The small drops resulted in small values of differential reflectivity and caused false alarms with the hail detection algorithm proposed by Aydin et al. that is based on reflectivity and differential reflectivity measurements and NCAR's hydrometeor classification algorithm (HCA). Raindrop disdrometer measurements were used to redefine the boundary that is assumed to separate "rain-only" and "hail-comtaminated" radar measurements. The new boundary reduces the number of false alarms.

Methods for hail detection that are less sensitive to drop-size variations are under investigation. A possible approach is to use the consistency among measurements of reflectivity, differential reflectivity, and specific differential propagation phase. A possible hail detection method is to estimate the specific differential phase from measurements of reflectivity and differential reflectivity and compare this estimate with the measured value. Preliminary testing indicates that this approach may also yield information regarding hail size. The method also has fewer tunable parameters.

NSSL and NCAR will collaborate in the development of a comprehensive test of proposed polarimetric hail detection algorithms.

Appendix E contains a description of the upgraded algorithm using improved drop shapes and a proposed algorithm based on measurement consistency entitled "Hail Detection with Polarimetric Radar," fulfilling deliverable 03.6.2.E11.

03.6.2.12 Test NCAR's freezing level on a polarimetric WSR-88D.

NCAR's freezing level algorithm (FLA) was applied to a polarimetric dataset obtained with the NSSL radar (KOUN). The proposed upgrade to the WSR-88D does not allow for measurements of the linear depolarization ratio. Consequently, the algorithm was modified to run only with the reflectivity and correlation coefficient measurements. [Differential reflectivity and differential propagation phase measurements are deemed less attractive for freezing level retrieval because these parameters show more variablity.] The test indicated the algorithm should work well on WSR-88D data.

A brief report illustrating application of the NCAR FLA to the KOUN measurements entitled "Improvements to the NCAR Freezing-Level Algorithm" is attached as Appendix F and fulfills deliverable 03.6.2.E12

03.6.2.14 and 03.6.2E14 Polarimetric radar detection of icing conditions.

This work is on hold. Preliminary investigation with radar measurements obtained with NCAR's S-Pol radar during the IMPROVE field programs suggest that the radar may be capable of detecting icing conditions associated with embedded convection in stratiform precipitation and icing in the upper regions of stratiform precipitation. Unfortunately, the necessary verification data do not exist. We will attempt to obtain the necessary datasets during the WISP04 field program.

03.6.2.15 and 03.6.2.E15 Evaluation of radar and radiometer data collected during the IMPROVE field program.

A radiometer dataset from IMPROVE II was examined to determine if the radiometer could be used as a surrogate for aircraft observations of liquid water. The radiometer integrates the liquid water along the beam. Unfortunately, rain that occurred on the day chosen for analysis could not be separated from that potentially associated with icing conditions. We will attempt to obtain the necessary measurements during the WISP04 field program.

b) Planned Efforts

Continue HCA development and testing using available cases from appropriate platforms.

c) Problems/Issues

None.

d) Interface with other Organizations

None.

e) Activity Schedule Changes

None.

03.6.3 Circulations

Particularly violent or long-lived storms tend to possess certain notable qualities, including, for example, mesocyclones. The current WSR-88D algorithms have a very high false alarm rate. Controllers find such high false alarm rates unacceptable. To mitigate this problem, new more robust and reliable circulation detection algorithms will be developed. Algorithms that use circulations to diagnose storm severity or estimate storm longevity will be considerably improved by this work.

a) Current Efforts

NSSL continued development of the Linear Least Squares Derivatives technique for the diagnosis of rotational and divergent shear during FY03. This work consisted several steps:

·The code was rewritten and optimized to eliminate redundancy and to allow for use on multiple radar platforms (WSR-88D, TDWR);

·Models were developed to simulate Doppler radar data depicting vortices and divergence (downburst) signatures;

·LLSD products were tested in a real-time setting with operational users;

·Data collection for approximately 100 tornado event days was initiated;

·Confidence bounds were computed for the azimuthal shear component of the LLSD.

The LLSD technique was compared to traditional "peak-to-peak" calculations of azimuthal shear, such as diagnosed by the WSR-88D Mesocyclone Detection Algorithm (MDA). Fig.1 shows the 2500m wide LLSD kernel and peak-to-peak azimuthal shear estimates for a 5 km diameter simulated vortex with "half vorticity" of 0.01 s^{-1} and Gaussian noise of 2 m s^{-1}. In this case, the mean LLSD value is within about 20% of the true value out to about 140 km, with a much smaller variance than that of the peak-to-peak azimuthal shear calculations. These values drop with range because of the geometry of the radar beam - circulations are not well sampled at long ranges.

Because we use synthetic radar data, the true location of the center of the circulation is known. Range and azimuthal position errors were calculated for both the LLSD and peak-to-peak methods. For azimuthal shear, the center of circulation was considered to be halfway between velocity absolute maxima on each side of the circulation (such as the MDA). For the LLSD rotation, the center of circulation was considered to be at the LLSD derivativeThe errors in range (Fig. 2) for both methods are quite similar, although the variance is smaller for the LLSD estimate. However, the azimuthal distance errors (Fig. 3) for the peak-to-peak method are significantly larger than the LLSD. Additionally, the distribu-

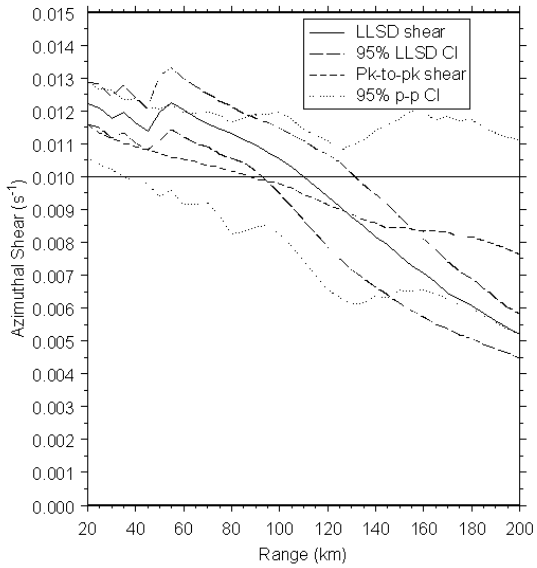

Figure 1. Mean and 95% confidence limits for LLSD and peak-to-peak estimates of azimuthal shear at the vortex center for a 5 km diameter vortex with half vorticity of 0.01 s^{-1}.

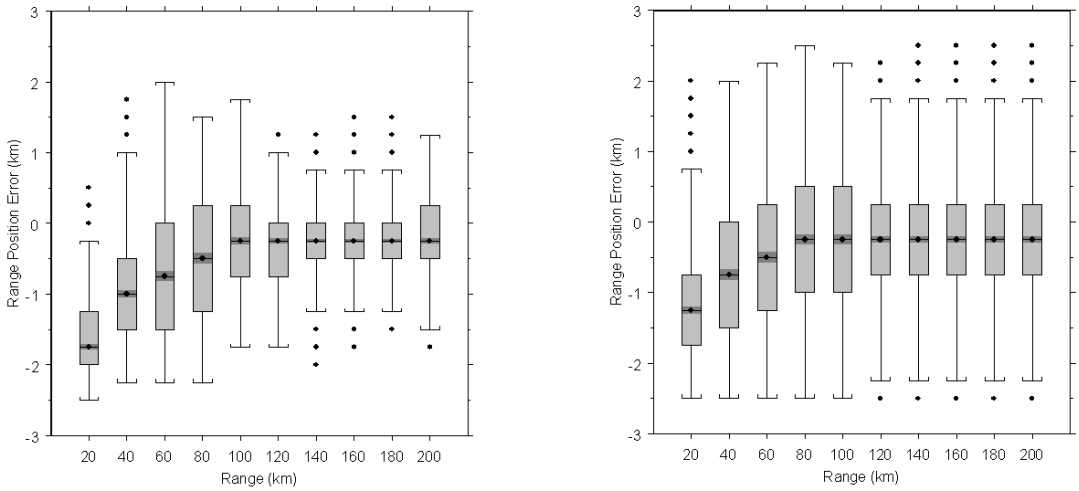

Figure 2. The distribution of range positional errors for the 2500 m LLSD kernel (left) and the peak-to-peak azimuthal shear estimate (right) for a 5 km diameter vortex. The center grey line is the median, the box is the interquartile range (IQR), the whiskers are the lesser of 1.5x(IQR) or the data range, and the single dots are outliers.

tion of the peak-to-peak location estimates is not Gaussian. This is illustrated in Fig. 4. While the LLSD position estimates are clustered around the center of the diagram, there are three distinct groupings for the peak-to-peak data. Because the peak-to-peak method only uses two data points in its calculations,

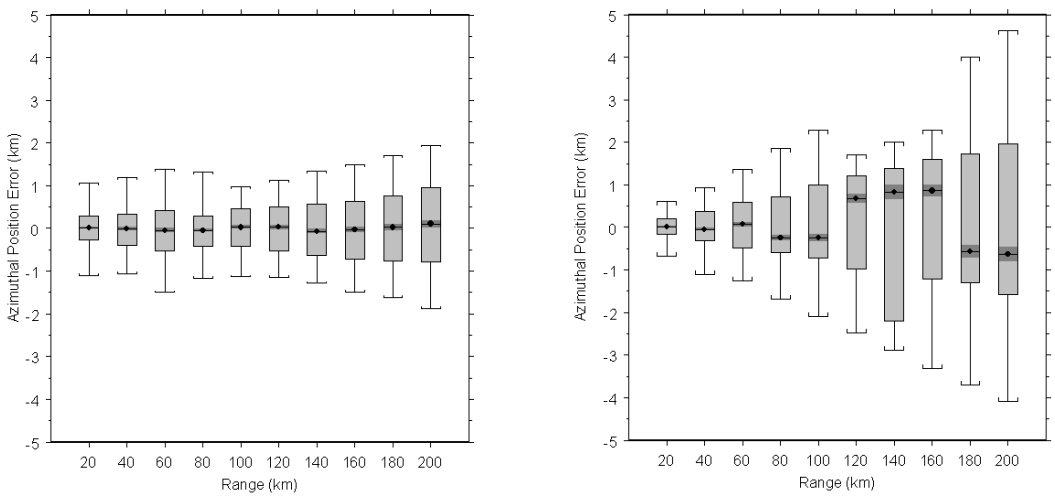

Figure 3. Same as Fig. 2, except for azimuthal position error.

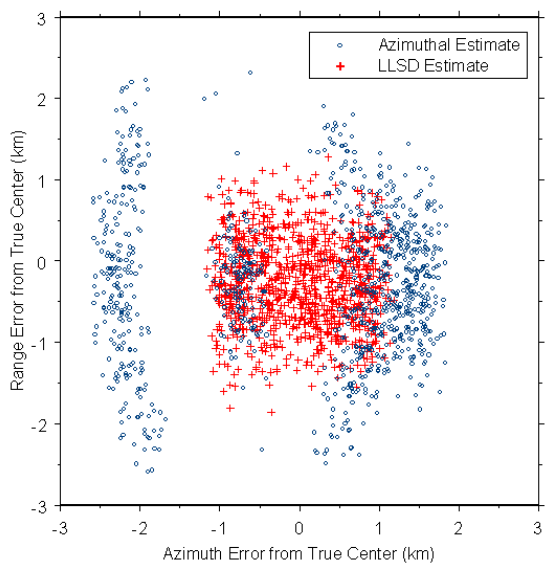

Figure 4. Scatter diagram of positional errors for the peak-to-peak azimuthal shear estimate and the LLSD estimate of the center of circulation for a vortex at 120 km range.

it is highly susceptible to errors caused by the radial offset from the center of the circulation and noise.

NSSL has developed a "rotation tracks" product based on the LLSD azimuthal shear output. This product has been successfully used operationally in two National Weather Service forecast offices during FY03. This product shows the 6-hour maximum of low-altitude circulations, which frequently corresponds to tornado or mesocyclone paths (Fig. 5). In order to improve the LLSD azimuthal

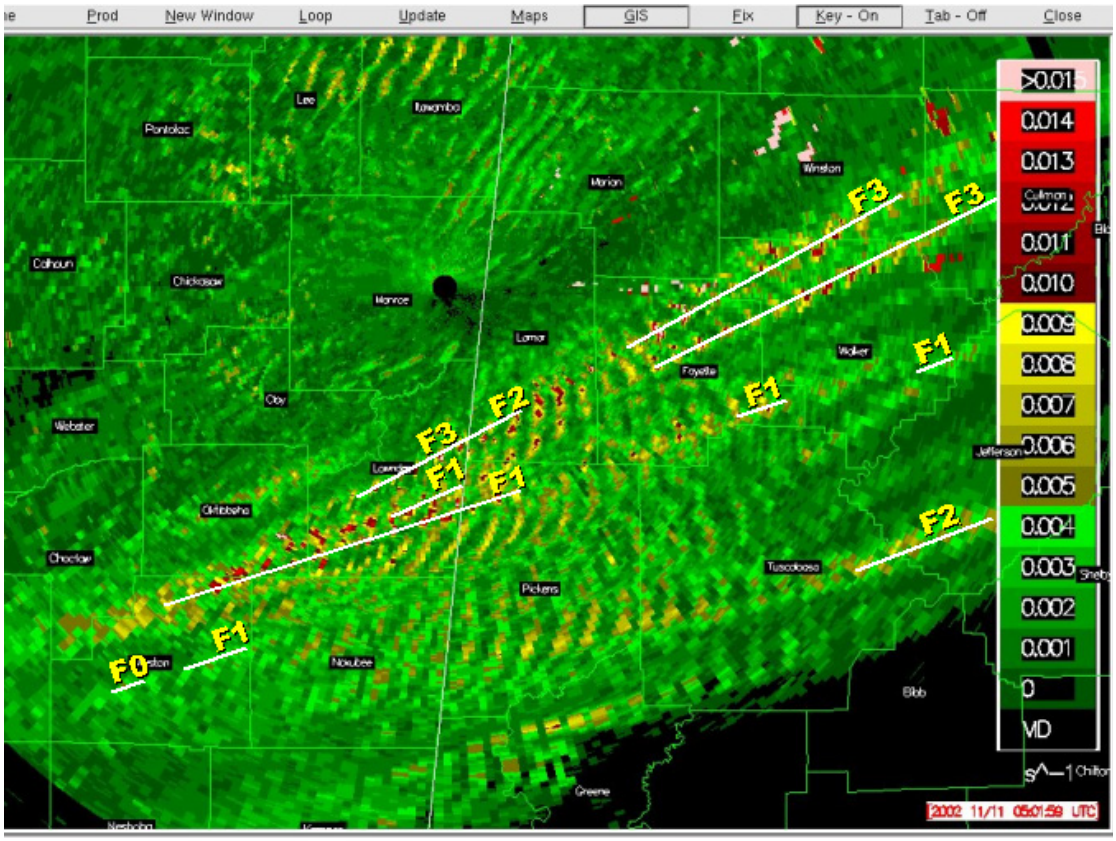

Figure 5. 6-hour maximum of rotational azimuthal shear (s-1), along with tornado paths and F-scale ratings, for the Nov 11, 2002 tornado outbreak from the KGWX (Columbus, MS) WSR-88D.

shear estimates shown in Fig. 1, a Cressman weighting scheme was introduced to smooth the response curve close to the radar, where a larger number of azimuths are required to meet the kernel width criteria.

A convergence/divergence radial velocity model was implemented in order to develop confidence bounds for the divergence portion of the LLSD. This model allows for variation of the size, intensity, range from the radar, and noise of radial velocity signatures of events such as microbursts. This model will be used to generate confidence bounds for the LLSD divergence calculations.

While this work displays results using tornadic storms, applications for LLSD extend well beyond such special cases. In particular, boundaries are surpisingly apparent in the derivative fields. In addition, th eoverall state of a storm might be diagnosed based on the profile of radial divergence associated with it. This last example requires better identification and tracking fo strom entities, which will become availabel with the implementation of the K-means clustering technique.

b) Planned Efforts

Continue development of enhanced, weighted LLSD techniques that also provide confidence limits for estimates.

c) Problems/Issues

None.

d) Interface with other Organizations

None.

e) Activity Schedule Changes

None.

03.6.4 Technical Facilitation

Technical facilitation supports the NEPDT algorithm development. There is currently no standard vehicle outside of NSSL for algorithm development support. The interface being developed at the NSSL, the WDSS-II, provides a way to develop, validate, verify and demonstrate the NEXRAD algorithms developed within this PDT. Additionally, WDSS-II provides a route into the Open Radar Product Generation (ORPG) system. WDSS-II will support and incorporate the MITRE Common Operations Development Environment (CODE). WDSS-II is an important ingredient for the overall success of the NEPDT because, in consonance with CODE, coding and testing standards at the application prototype level are enforced. Transfer of single-radar algorithms to the ROC will be straightforward, as anything within WDSS-II must also conform to CODE standards. Overall, NEPDT efforts will inevitably enhance the algorithms that have been accepted or will be implemented by the ROC as part of the WSR 88D system.

<u>a) Current Efforts</u>

1) Infrastructure support for research tasks:

a) We can now compute and display radar reflectivity at various temperature levels based on data from multiple radars and isotherms heights derived from the RUC2 model in real-time.(Fig. 6.

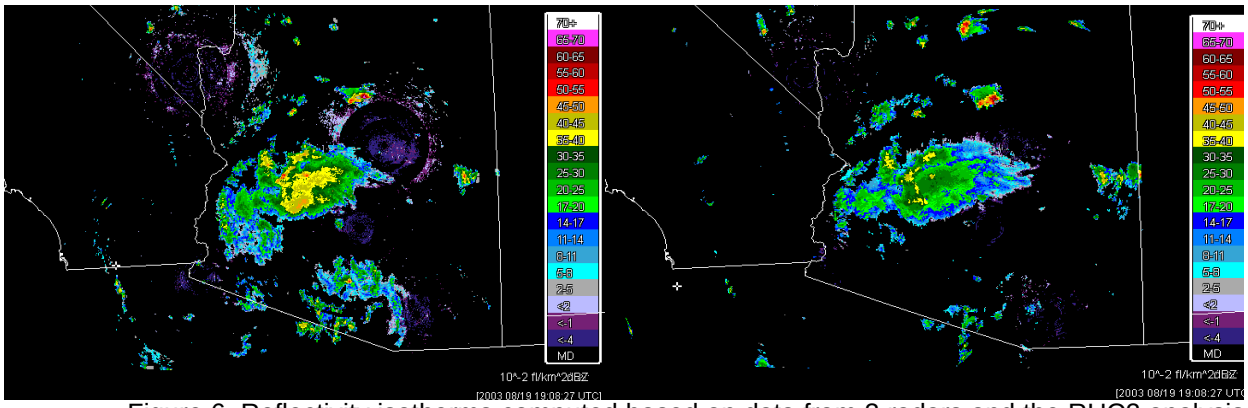

Figure 6. Reflectivity isotherms computed based on data from 3 radars and the RUC2 analysis grid in real-time. Left: Reflectivity at 0C. Right: Reflectivity at -20C.

b) We have developed gridded lightning product based on lightning flash density.(Fig. 7).

c) We now support data readout in *both English and Metric units* to support both scientific users (who want Metric) and real-time forecasters (who want English). The unit setting is changeable on the fly.

d) With the easier PRF-selection in ORPG Build 5, we envision that weather service forecasters will have different PRFs within the same tilt much more

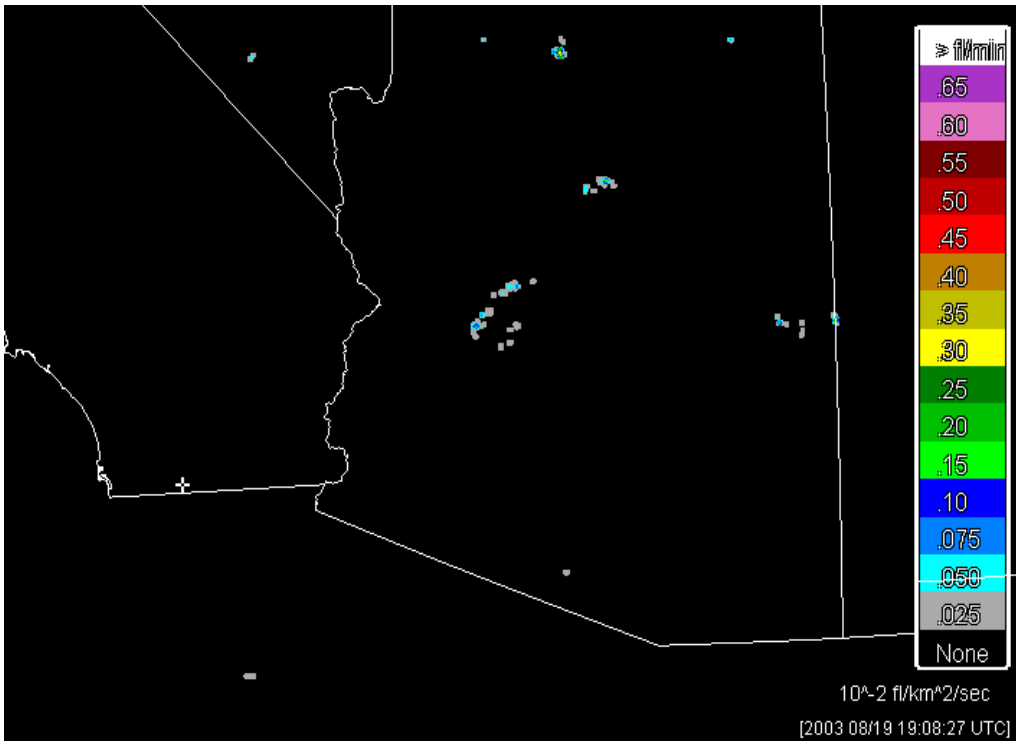

Figure 7. Gridded lightning data created from all the lightning flashes in a 15-minute interval..

often. Hence, we now support multiple ingest, display and dealiasing of data with *multiple Nyquist velocities in the same elevation scan*.

e) Display of data from the Mosaic and QPESUMS algorithms.

f) Display of several polarimetric radar algorithm products.

g) ORPG product display. We worked on displaying some data from the ORPG baseline to enable comparison of algorithm improvements with the baseline system. We can also display several ORPG Build5 products - this was used for verifying that the ORPG algorithms were correct. Products displayed included several table products: mesocyclone, storm tracks, hail index and some base data products (Fig. 8).

h) GRIB data display. Improved the ingest and display of GRIB data (model and analysis fields) by introducing region specification and improved colormaps (Fig. 9).

i) The multi-radar merger process was modified so that the blending of data from multiple radars uses a power-weighted averaging function. The difference is insignificant.

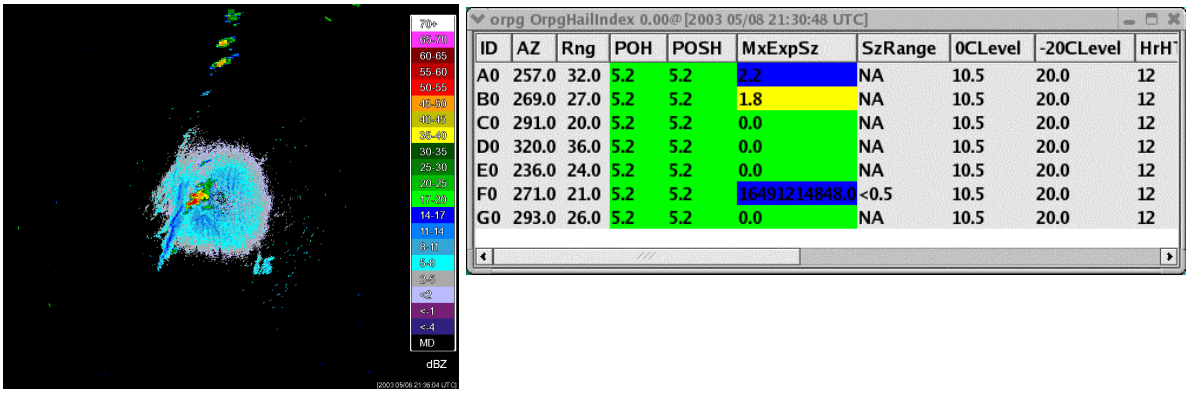

ID	AZ	Rng	POH	POSH	MxExpSz	SzRange	0CLevel	-20CLevel	HrH
A0	257.0	32.0	5.2	5.2	2.2	NA	10.5	20.0	12
B0	269.0	27.0	5.2	5.2	1.8	NA	10.5	20.0	12
C0	291.0	20.0	5.2	5.2	0.0	NA	10.5	20.0	12
D0	320.0	36.0	5.2	5.2	0.0	NA	10.5	20.0	12
E0	236.0	24.0	5.2	5.2	0.0	NA	10.5	20.0	12
F0	271.0	21.0	5.2	5.2	16491214848.0	<0.5	10.5	20.0	12
G0	293.0	26.0	5.2	5.2	0.0	NA	10.5	20.0	12

Figure 8. ORPG base reflectivity and HailIndex table products.

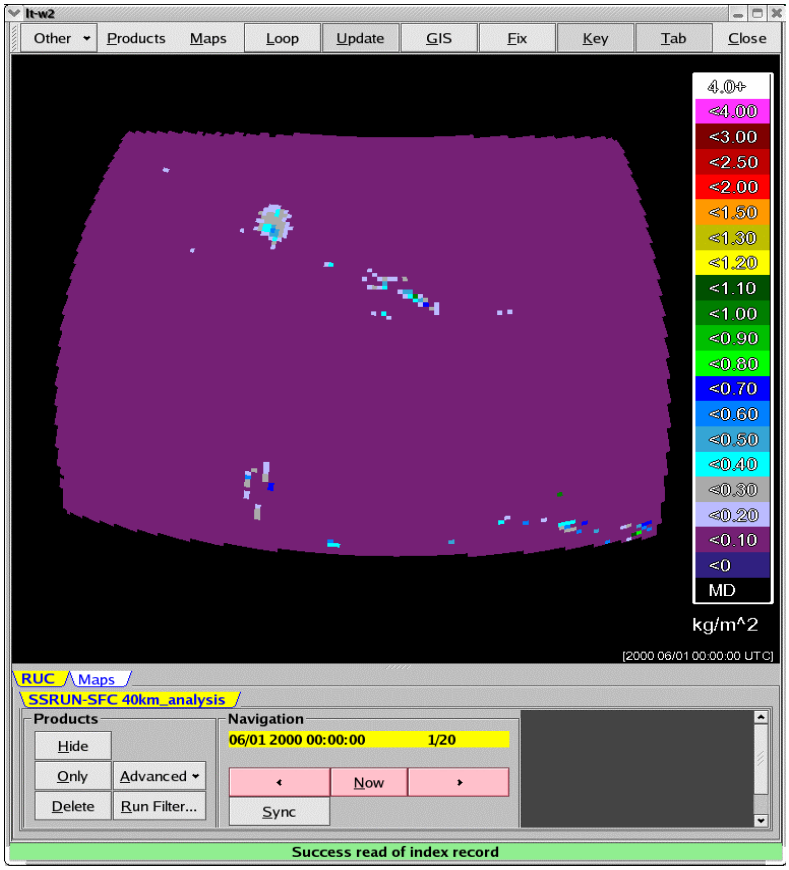

Figure 9. Model data from GRIB files.

2) Lightning Prediction Algorithm. We are developing a lightning-prediction algorithm that predicts lightning initiation based on reflectivity isotherms and past lightning activity. The lightning ingest algorithm was rewritten to avoid the use of a GUI, to aid automated use. In addition, a program to grid lightning flash data, and another program to compute reflectivity isotherm levels was written. These serve as inputs to the lightning prediction algorithm which uses a Linear

Radial Basis Function based on past history to make predictions of lightning initiation (Figs. 10 and 11).

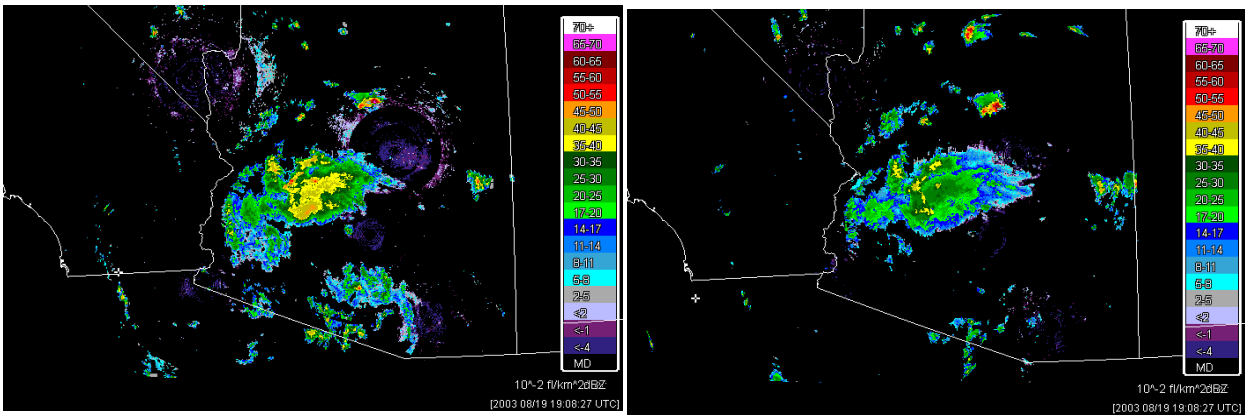

Figure 10. Reflectivity isotherms computed based on data from 3 radars and the RUC2 analysis grid in real-time. Left: Reflectivity at 0C. Right: Reflectivity at -20C. These are two of the inputs to the lightning prediction algorithm.

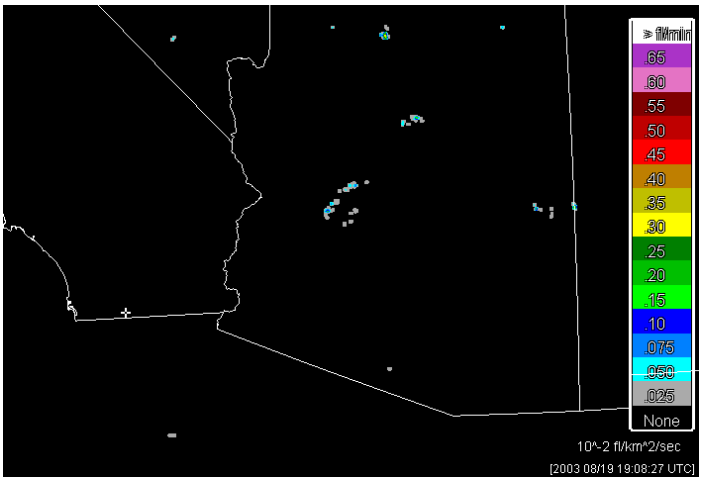

Figure 11. The lightning density over 15 minutes. This is used to train the Linear RBF in real-time, so that the lightning prediction algorithm automatically evolves with the environment.

3) Radar Quality Control (Appendix H). Several algorithms were modified to optionally use a neural network quality control reflectivity data as their input. This increases the skill of these other algorithms:

a) Meso-cyclone Detection Algorithm. The velocity data that is used by the modified MDA is not the entire velocity data, but a cut-out such that the MDA does not make any detections in data deemed to have reflectivity below 0dBZ. In the absence of quality control, the MDA finds several mesocylones in clear-air. When such clear-air echoes are removed by the QCNN, these false alarms are avoided, without any impact on the true detections (Figs 12 and 13).

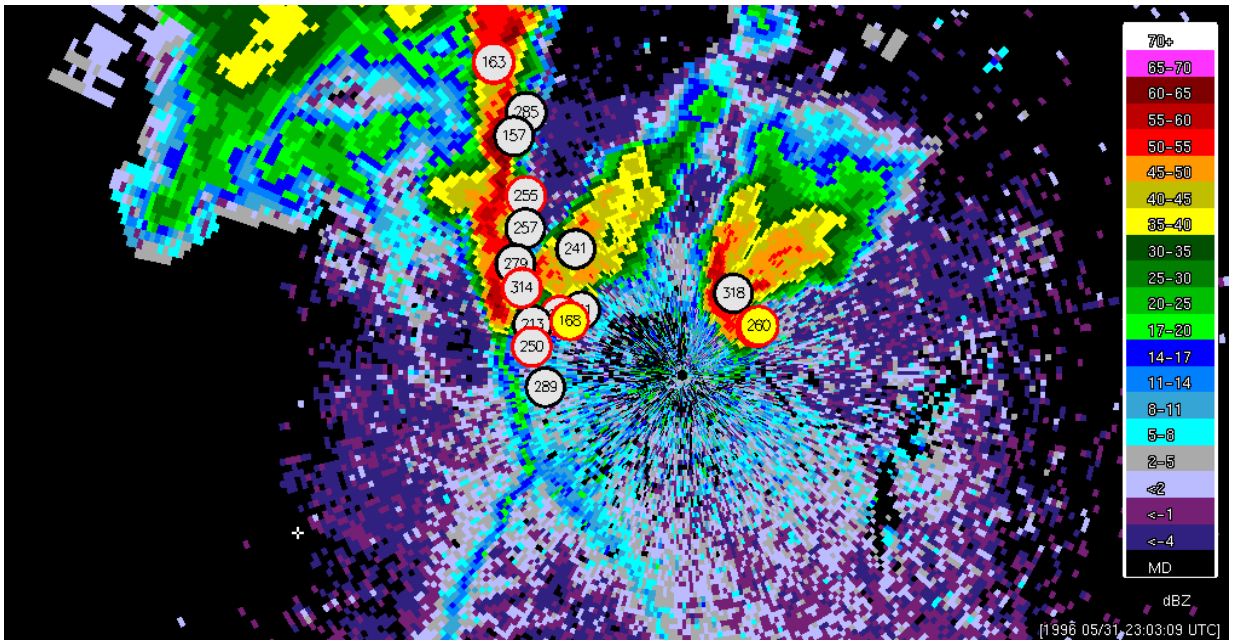

Figure 12. MDA performance in clear air.

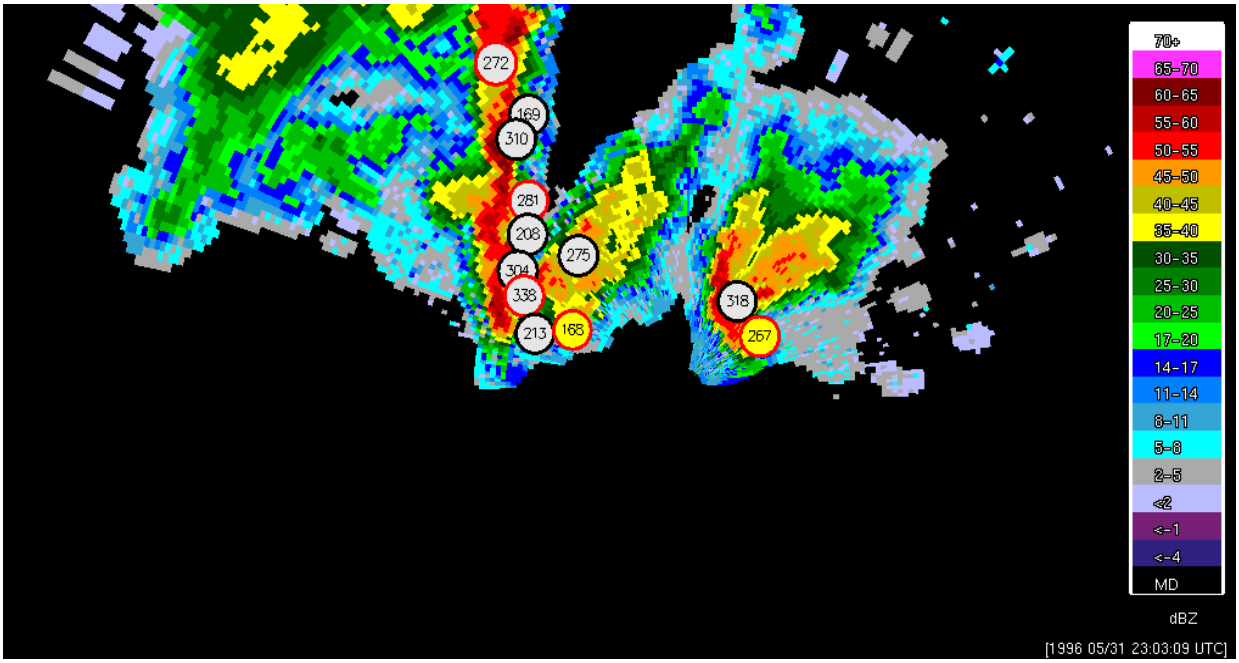

Figure 13. MDA performance on QC-ed data; there are now no false alarms in clear air.

b) Storm-cell Identification and Tracking Algorithm. Centroid estimates improve when there is some precipitation embedded inside an area of anomalous propagation (Appendix G).

c) Motion Estimation and Forecast: The quality of the forecasts improves when the motion estimation algorithm is run on QC'ed radar data. (Figs. 14 and 15).

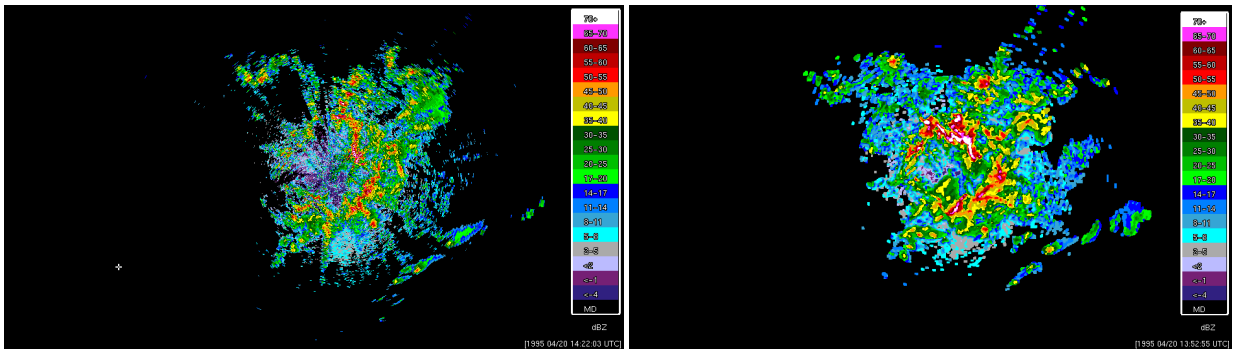

Figure 14. Left: What actually happened in 30minutes vs. the forecast of what would happen in 30 minutes when the input was the "raw" reflectivity data. Note how poor the forecast is, essentially because the AP pattern 30 minutes ago is also getting advected.

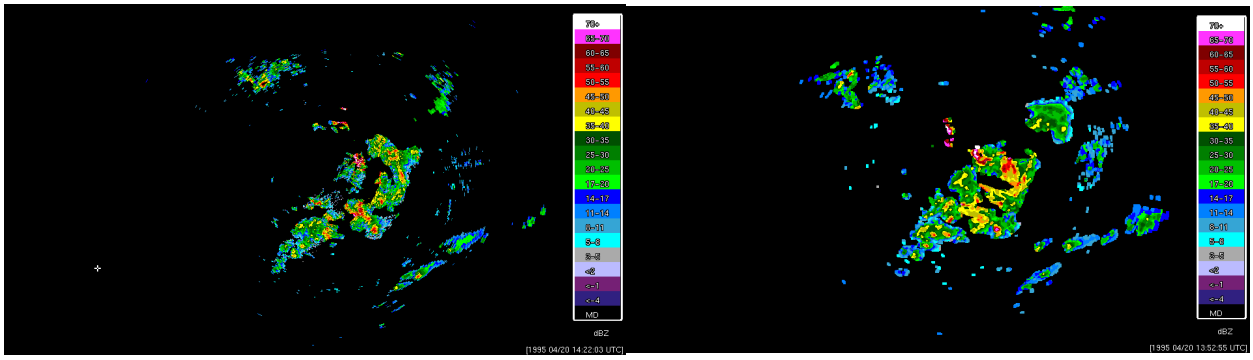

Figure 15. Left: What actually happened in 30minutes vs. the forecast of what would happen in 30 minutes when the input was the quality-controlled reflectivity data. Note how much better the forecast is, when the bad AP is removed before the motion estimates are computed.

d) Multi-radar mosaics. Multi-radar merged Reflectivity with quality-control of reflectivity and internal advection individual radar views, as well as the high-resolution merger of the quality-controlled data (Figs. 17 and 17). The basic mosaic process is identical to that used in the 3D gridded mosaic. Hence, this product will be merged with the 3D gridded mosaic product, to account for advection in FY04.

4) New Dealiasing Algorithm. A new dealiasing algorithm developed by Qin Xu et al. was implemented in real-time mode on both WSR-88D and TDWR data for easier comparison with the 88D routines. The algorithm performs better than the 88D dealiasing algorithm in certain situations. The 88D algorithm, in turn, was found to perform better (even on TDWR data) than the native-TDWR algorithm (Fig. 18).

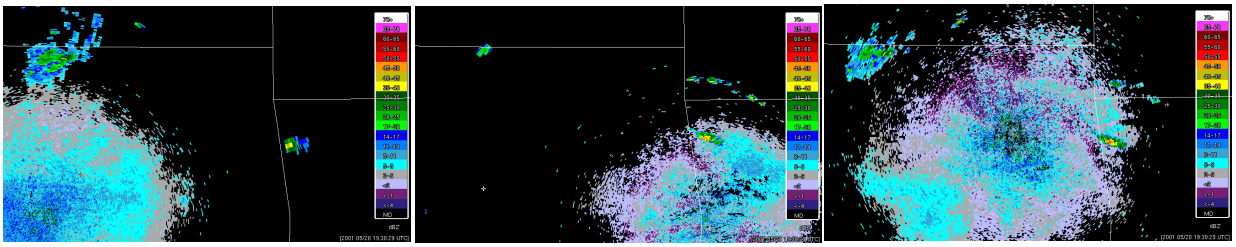

Figure 16. Views of the same storm from 3 different radars: KTLX, KINX and KSRX. Note the differing resolutions, as well as the extensive clear-air return. Compare with Figure 3d-2.

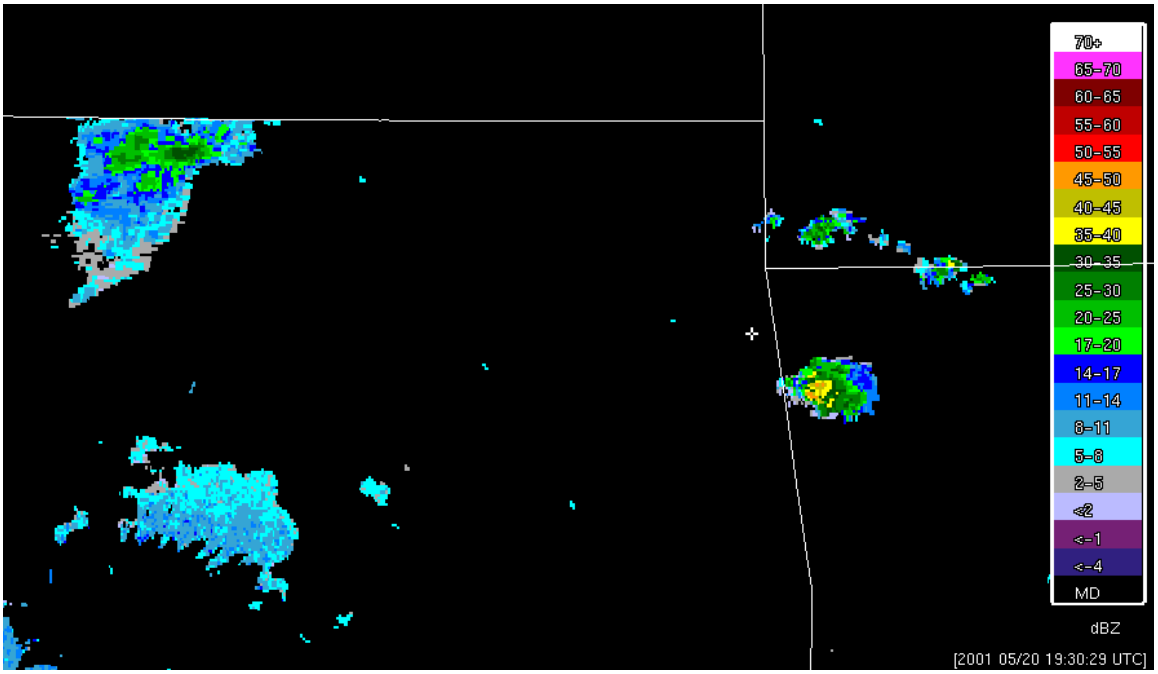

Figure 17. The same storm with the data from all 3 radars merged. The merged data has been quality-controlled using the QC neural network developed at NSSL. The storm cells are at high resolution, in the right spot, taking the time differences, and viewing angles of each of the radars into account. It is likely that with the QC'ed field, some storm cells that could get lost in the clear-air return from the individual radars are clearly visible.

5) Software was written that would compute the beam-blockage for every WSR-88D radar in the continental US, which can lead to a potentially significant imporvement in data quality. A Java display tool was created to view these beam-blockage patterns for use by the Weather Decision Training Branch (Figs. 19, 20 and 21). While developed for Weather Decision Training Branch, this capability stands to substantially enhance radar data quality overall.

6) Maintenance tasks:

Fixed problems in the following areas:

(a) the ORPG infrastructure (LB_read)

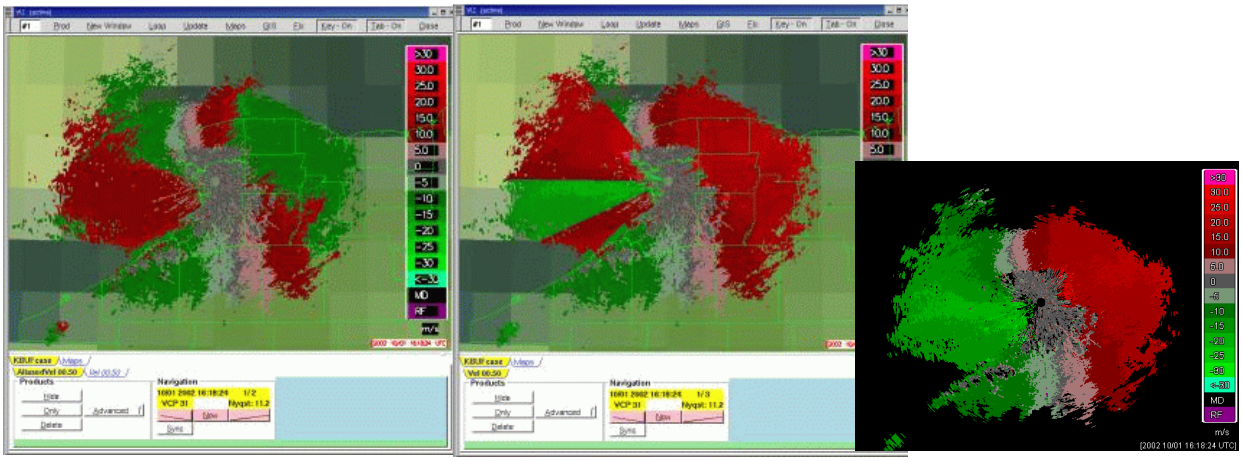

Figure 18. Comparision of dealiasing algorithms. (a) the original, aliased velocity data. (b) Performance of the 88D dealiasing algorithm (c) Performance of the new Qin Xu algorithm.

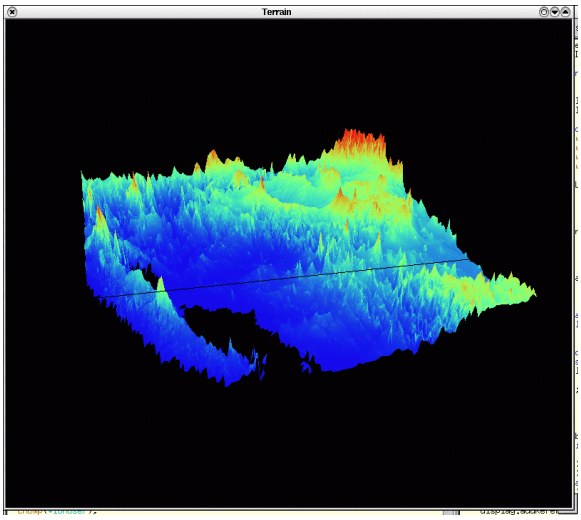

Figure 19. Terrain around the Phoenix Weather Service Radar.

(b) operational WDSS-II build, for Wichita WFO
(c) TDWR volume display
(d) Hide button functionality.

b) Planned Efforts

Continue merger of advection routine into 3D gridded mosaic.

c) Problems/Issues

None.

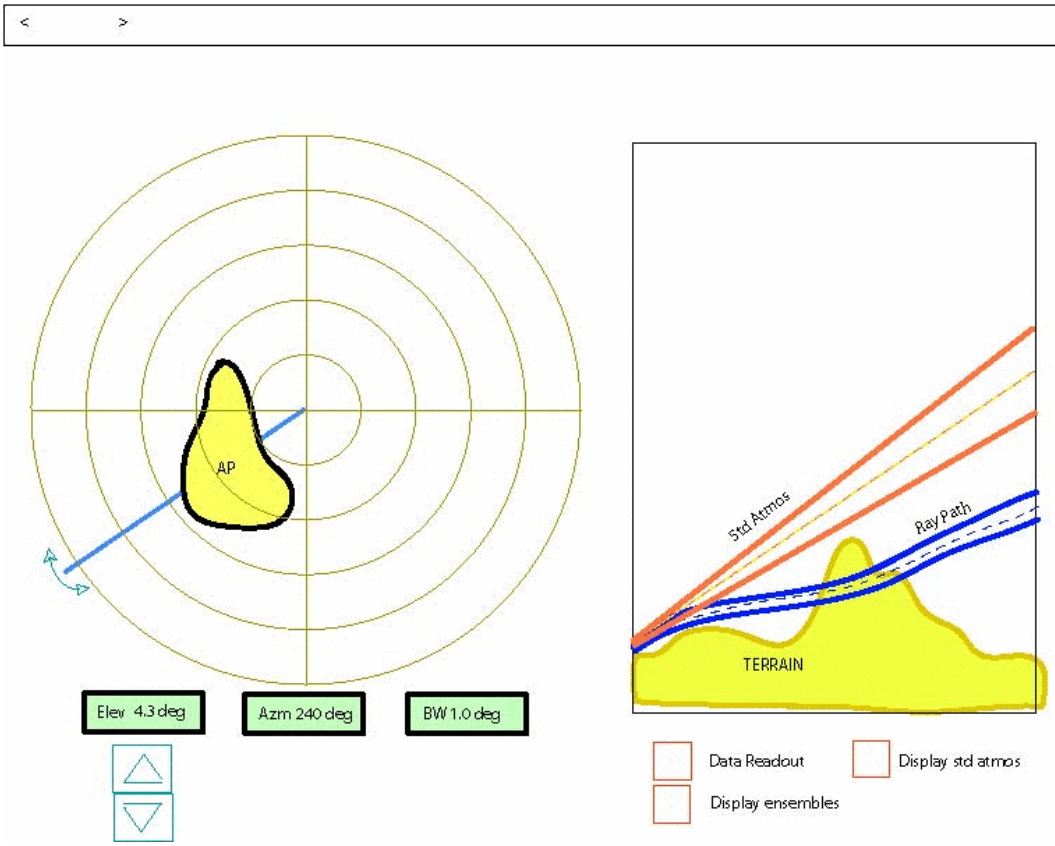

Figure 20. he newly developed tool aims to allow the user to trace different ray paths (other than standard atmosphere).

d) Interface with other Organizations

None.

e) Activity Schedule Changes

None.

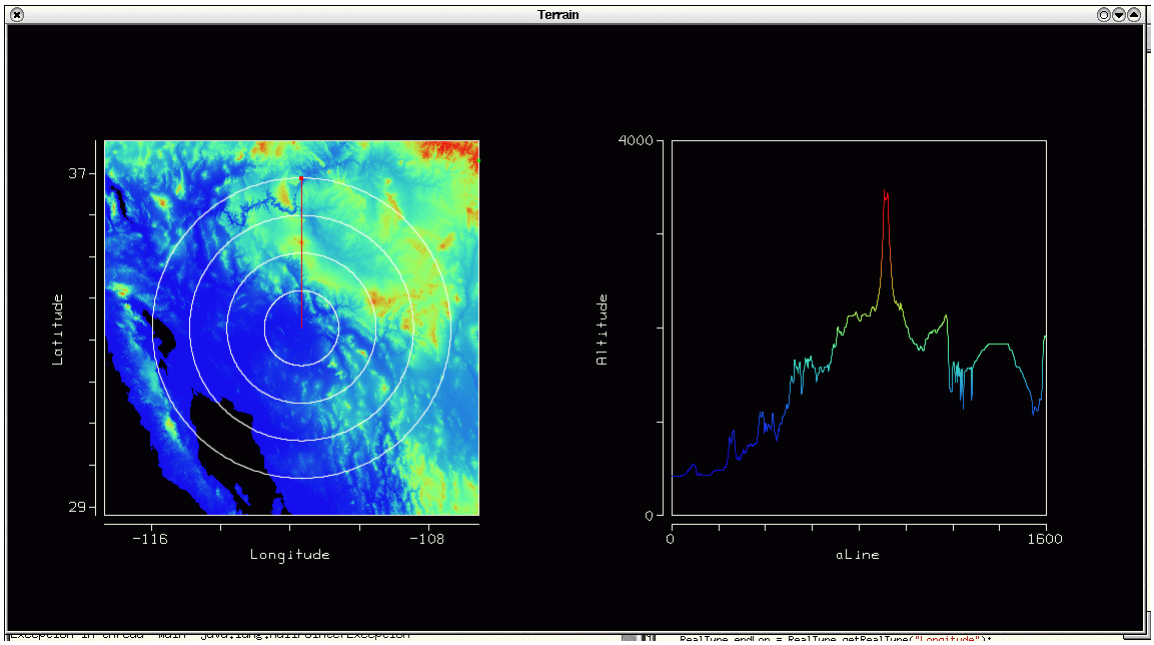

Figure 21. Visualizing the terrain along the path of a radial.

03.6.12 Product Implementation

Product implementation is a the process by which implementation paths are explored and defined within the aviation community systems that are best for NEPDT products. This process includes collaboration with other PDTs to help define the nature of WSR-88D they need. Technical facilitation also includes the low-level process of defining technical details (formats, data set file structures, etc.) of the products developed NEPDT.

a) Current Efforts

Development begun on National 3D gridded mosiac. Pursuit of an additional product to estimate refractivity has begun. Atmospheric refractive index can be used to help identifiy areas that are a combination of cool/dry or moist/warm, which should be useful for boundary identification.

Extensive meetings held at NCAR and ETL concerning future NAPDT organization and activities.

b) Planned Efforts

Continue efforst at implementing new work plans that include a boader range of weather radar product development.

c) Problems/Issues

None.

d) Interface with other Organizations

NCAR, MIT/LL, ETL.

e) Activity Schedule Changes

None

03.6.14 Multi-radar Composites

The area for which any arbitrary ARTCC has responsibility likely encompasses the coverage area of several WSR-88D installations. Neither the ROC nor the NWS has plans to treat the various WSR-88D installations as a single network, so there are no existing algorithms that use data from more than one radar. This is a serious limitation, because treating each radar separately leads to ambiguities when the radar data overlap. Currently, the users must independently mitigate these ambiguities, which requires significant knowledge about meteorological radar data and the nature of the algorithms that are run on these data. Aviation users generally do not possess this knowledge, so for the WSR-88Ds to be treated as a network, algorithms and techniques aimed specifically at multiple radar composites must be developed.

a) Current Efforts

03.6.14.1-2 Real-time, high resolution 3D reflectivity mosaic for the CIWS region.

The activities for this quarter include a system upgrade to the real-time CIWS mosaic computer. The upgrade increases security measures of the computer system such that they meet the NOAA computer security standards. The upgrade includes moving the computer from outside the NSSL firewall to inside and updating operating system from Linux RedHat7.3 to Linux RedHat9.0. The random access memory (RAM) on the machine is increased from 2GB to 8GB to alleviate memory shortage problems when wide spread precipitations occur in the CIWS domain.

The new enhanced 3D mosaic algorithm has been tested using various archive cases and it is implemented for the real-time CIWS domain. The enhancements are described below.

1) Product time stamps are modified to be more representative of observation times.

Time stamps of the previous 3D mosaic products used clock times (round up to the whole 5 minutes) when the 3D mosaic ran (see red arrows in Fig. 1). The 3D mosaic finds latest volume scans from all radars that are within a certain time window (default value is 15 min) and then mosaic them onto the analysis grid. When data latency is long, product time stamps are usually lagging the actual observation times (Fig.22), sometime by a significant amount. The new enhanced mosaic uses average times of all radar volume scans that go into the mosaic as product time stamp (see blue arrows in Fig. 22). This is more representative of when the mosaic analysis fields valid than the clock times.

2) New diagnostic products are created to show smoothing effect of the 3D mosaic scheme.

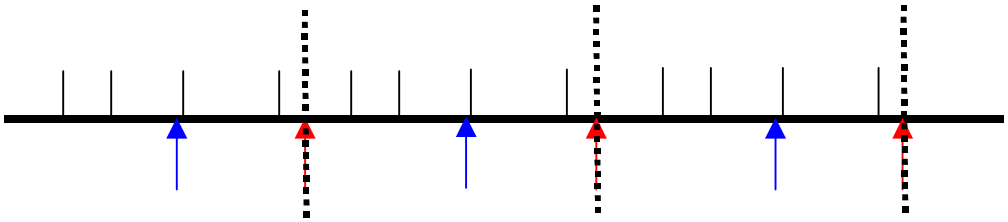

Figure 22. A schematic plot of the mosaic product time stamps. The legend is: Bold black line: time axis; Thin black lines: observational times; Dotted lines: clock times when the mosaic runs; Red arrows: product time stamps based on clock; Blue arrows: new product time stamps based on observations.

Many existing severe storm algorithms (e.g., storm cell identification and tracking, hail detection, mesocyclone detection, etc) use the maximum echo intensity of storms as a parameter. When radar reflectivities are analyzed onto Cartesian grids, storm intensities are usually damped due to smoothing in the analysis scheme. Therefore it is important to understand the smoothing effect of the 3D mosaic. In the new 3D mosaic, two composite reflectivity mosaic fields are generated. One is derived from the 3D reflectivity mosaic with the interpolation and gap-fillings. Another is derived by mapping vertical column maximum reflectivities from multiple radars onto the Cartesian grid without any interpolation and gap filling. A difference field between the two is also generated as a new product. Fig. 23a-c shows these results. Fig. 2c shows a difference field between the non-smoothed composite reflectivity field (Fig. 2a) and a composite reflectivity field from a 3D mosaic grid using a nearest neighbor analysis scheme. With the nearest neighbor analysis, the 3D mosaic only smoothes data in close ranges (usually <40km) where sizes of radar data bins are smaller than analysis grid cells (in this case 1km x 1km). The smoothing effect is not significant (<3dbz) unless within 10km range of the radar. Fig. 24 shows similar images as in Fig. 2 except for a 3D mosaic using a vertical interpolation

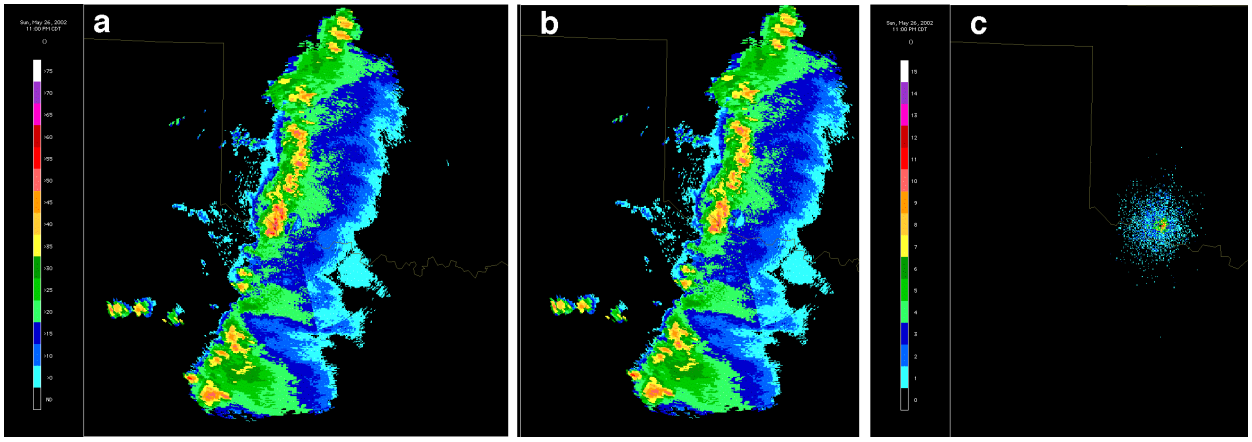

Figure 23. Non-smoothed composite reflectivity (a), composite reflectivity field derived from a 3D mosaic with a nearest neighbor analysis (b), and the difference between the two (c).

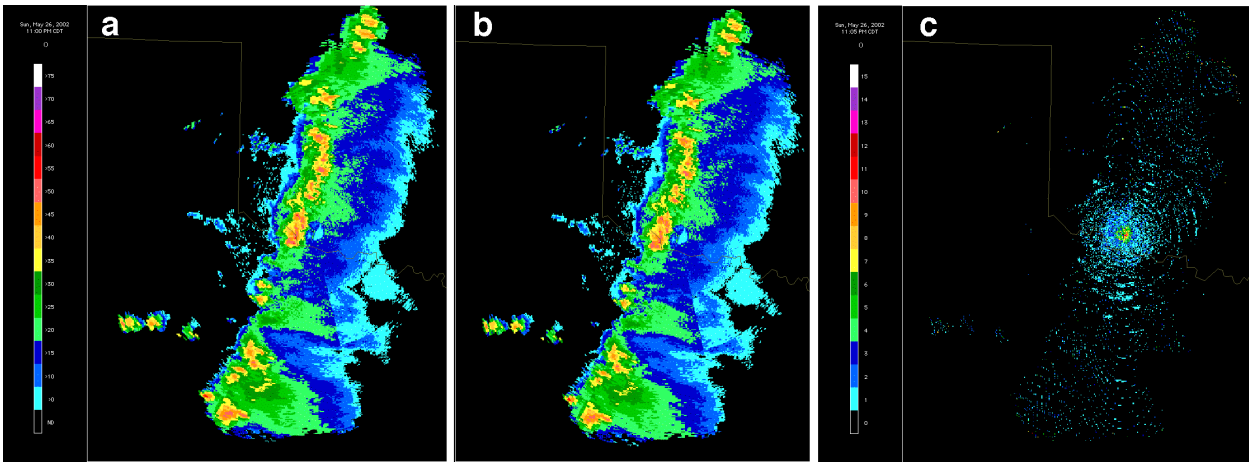

Figure 24. Non-smoothed composite reflectivity (a), composite reflectivity field derived from a 3D mosaic with a vertical interpolation scheme (b), and the difference between the two (c).

scheme. The interpolation caused damping not only in close ranges, but also in far ranges. Nevertheless, the damping is still not significant beyond 10km range. Given the fact that the nearest neighbor analysis causes discontinuities on constant height levels (Fig. 25), the vertical interpolation analysis is still a

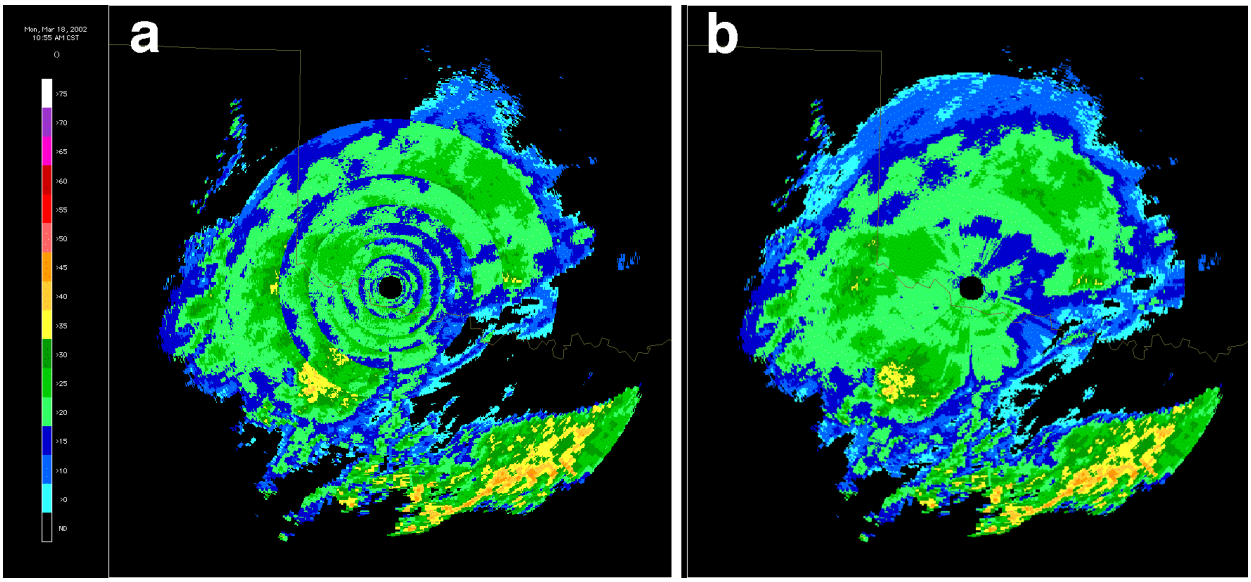

Figure 25. Horizontal cross section of reflectivity at 6km (msl) from 3D mosaic with a nearest neighbor scheme (a) and with a vertical interpolation scheme (b), respectively.

preferred mosaic scheme over the nearest neighbor scheme.

3) *Steeper mosaic weighting function is used for preserving high-resolution storm structure.*

The previous 3D mosaic uses a Cressman weighting function when combining multiple radar data at a same grid point. However, the Cressman weighting function is too flat and high-resolution storm observations near one radar can be smeared by low-resolution observations from another radar that is far away (Figs. 26a and c). After replacing the Cressman weighting function with a

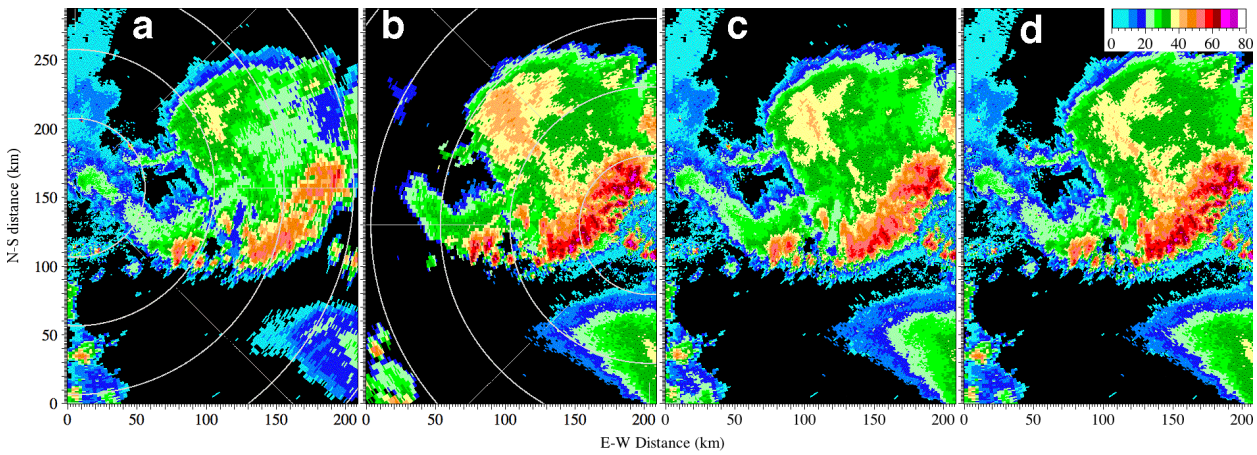

Figure 26. Composite reflectivities from KLOT (a), KIWX (b), mosaic of the two using the Cressman weighting function (c), and mosaic of the two using the exponential weighting function (d).

steeper exponential function (Fig. 27), the smear effects are significantly allevi-

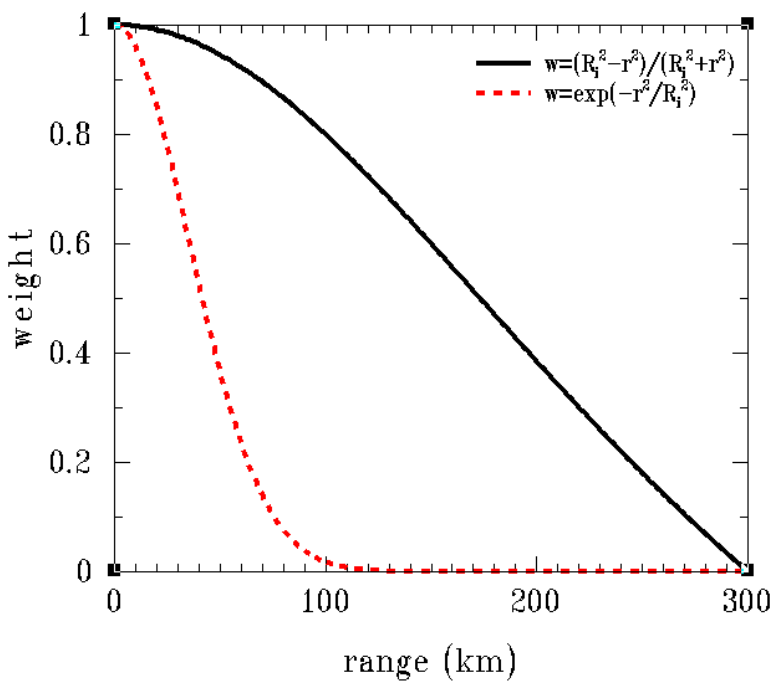

Figure 27. The Cressman and exponential weighting functions used to generate Figs 5c and 5d, respectively. Here Ri=300km for the Cressman function and Ri=50km for the exponential weighting function.

ated (Fig. 26d vs.b).

4) Modified gap-filling scheme to increase computational efficiency.

In the 3D mosaic scheme, a general vertical interpolation between tilts is performed for all cases. When a brightband is identified a gap-filling scheme is invoked and additional horizontal interpolation is performed to reconstruct stratiform echoes. In the previous 3D mosaic scheme, the gap-filling procedure is performed on the fly and is separate from the regular vertical interpolation. In the new mosaic, the gap-filling procedure is combined with the regular vertical interpolation and a unified lookup table is created for the polar-to-Cartesian coordinates transformations. Some code modifications are done to speed up the lookup tables generation process. The modifications dramatically reduced CPU usage (from ~1 hour to ~2 minutes per radar per domain) even though the RAM usage increased some (from ~300MB to ~500-600MB for a 1001x1001x21 grid). The modifications also reduced the CPU times for the 3D mosaic by ~20-50%.

This completes deliverable 03.6.14.E2.

03.6.14.6-7 A 4-D dynamic data analysis and visualization system.

Initial code has been developed for the 4-D dynamic grid (4DDG) and preliminary results are generated from a case study in Oklahoma on August 14, 2002. Fig. 28 shows the 4DDG domain for the case study. The domain covers south-

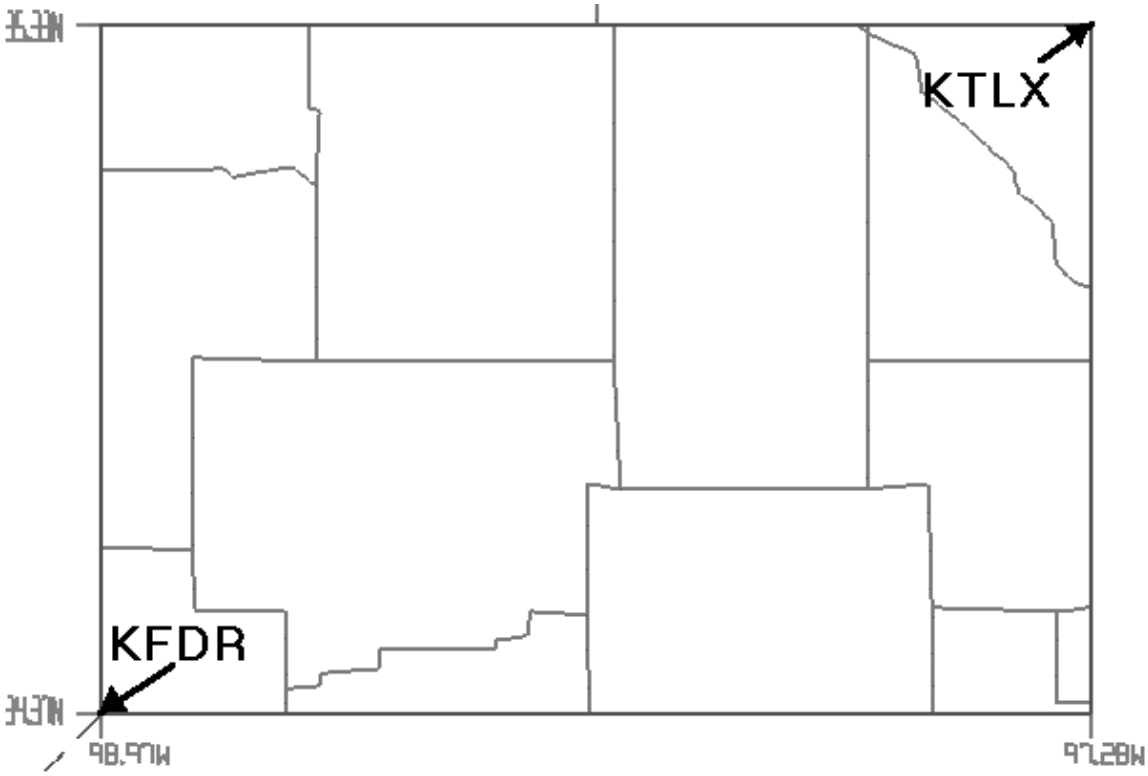

Figure 28. Example 4DDG domain.

west Oklahoma region, and KFDR and KTLX radars are located at the southwest and northeast corners of the domain, respectively.

Two movies are generated from the 4D dynamic reflectivity mosaic and the movies are available at http://cimms.ou.edu/~jzhang/4ddg/4DDG_Demo_1.gif and http://cimms.ou.edu/~jzhang/4ddg/4DDG_Demo_2.gif.

Both movies show a time series of a vertical cross section that cut through the two radars (with KTLX at the left corner and KFDR at the right). Note that in the 4DDG, the analysis is updated every time when a new tilt of data arrives. The first movie (4DDG_Demo_1.AVI) shows results where new data overwrite old data. The second movie (4DDG_Demo_2.AVI) shows results where an exponential time weighting function (wt = exp[-t2/T2], where T is a time decay scale with a value of 120 seconds) is used. It is apparent that the exponential time weighting produces a more consistent analysis than the new-overwriting-old scheme. It is also evident that range dependency of radar observations has large impact on the mosaic field. In the first movie, when the analysis grid was updated by KFDR data at frames 16, 18, and 20, the intensity of a storm cell close to KTLX (left corner) was greatly damped because the KFDR data were from farther ranges than were the KTLX data. This damping effect is not dominant in the second movie because the KFDR data are weighted both in time and in space, using an exponential weighting function wmosaic = exp [-r2/R2] (here R is a space length scale with a value of 50km). More case studies are needed to understand the spatial and temporal variations of different storm systems and their relationships with radar sampling and analysis schemes, and different time and space scale factors may be required for different weather regimes.

This completes deliverable 03.6.14.E6-7.

b) Planned Efforts

The development of a prototype 4-D dynamic grid will continue.

c) Problems/Issues

None.

d) Interface with other Organizations

Continue to provide the real-time 3D mosaic data to CWPDT, WWPDT and CIWS Project.

e) Activity Schedule Changes

None.

03.6.15 WARP Activities

The WARP is integral to AT controller displays. Warp is significant in that it shifts the burden of displaying weather radar returns to an instrument specifically designed as a weather radar: the WSR-88D. However, due to the nature of its mission and hardware, the WSR-88D cannot take the same approaches to data quality control as do the long-range L-band radars currently used by ATC. New approaches to data quality control need to be developed so the users have confidence in the weather data products displayed to them.

a) Current Efforts

NSSL has been providing guidance on the accuracy of ORPG AP (anomalous propagation) -mitigated composite reflectivity products for the Federal Aviation Administration (FAA) and The National Air Traffic Controllers Association (NATCA). NATCA has recently become very concerned about the accuracy of ORPG product 96 (0-70,000 ft composite reflectivity with AP mitigation) relative to ORPG product 36 (0-70,000 ft composite reflectivity without AP mitigation). An example from June 10th of this year (Figs. 29-31) shows how the reflectivity values from the composite reflectivity product are reduced (sometimes significantly) by the AP mitigation algorithm.

Fig. 29 shows numerous small (~20 km in diameter), individual convective cells exist east and northeast of the Corpus Christi, Texas WSR-88D (KCRP) on June 10, 2003, with many of the cells containing regions of >50 dBZ echoes. However, the AP-mitigation algorithm reduces the maximum reflectivity returns by 5-15 dBZ for most storms (Fig. 30). In this example, the reduction is very clear because there are numerous cells containing localized (~4 km) regions of >50 dBZ regions shown in red, while no cells contain regions of >50 dBZ in the AP-mitigated product.

The ORPG AP mitigation algorithm is based on an AP-edit/removal technique developed at Lincoln Labs (Smalley and Bennett 2001). However, one of the differences between the two methods is the use of a median filter by the ORPG product that is not used by the Lincoln Labs technique. It was found that the preferred operation of the AP-edit technique was not to use the median filter, but instead a scatter filter.

The median filter used by ORPG can be manually bypassed through modification of the ORPG code. Fig. 31 displays the result of the ORPG AP algorithm when not using the median filter. By comparing Figs. 30 and 31, it is clearly shown that the reduction of reflectivity magnitudes in ORPG product 96 is entirely attributable to the median filter. In fact, in this case, the AP algorithm identifies very few pixels that can be attributed to AP as seen by comparing Figs. 29 and 31. However, since the median filter is applied over the entire reflectivity field to produce ORPG product 96, the resultant reflectivity image is significantly modified.

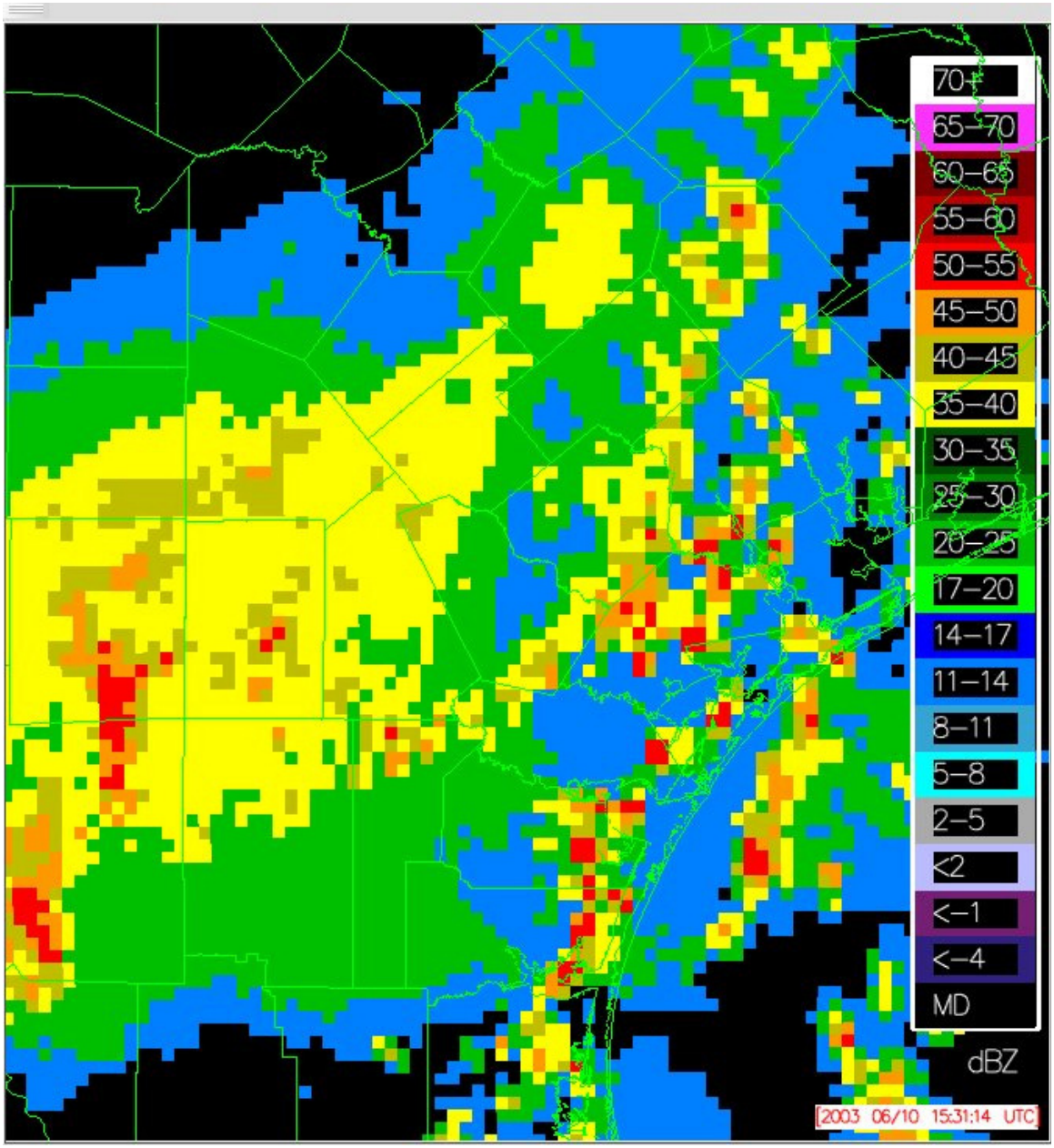

Figure 29. ORPG Composite Reflectivity Product 36 output for the Corpus Christi (KCRP) WSR-88D radar at 1531 UTC, June 10, 2003.

Smalley and Bennett (2001) outline how to use an optimal adaptation parameter set associated with the median filter so that it could respond more like the much preferred scatter filter. However, even with the use of these optimal settings, a very undesirable result is still obtained for the June 10, 2003 case. Possible solutions for this particular case are still being considered.

This completes deliverable 03.6.15.E4

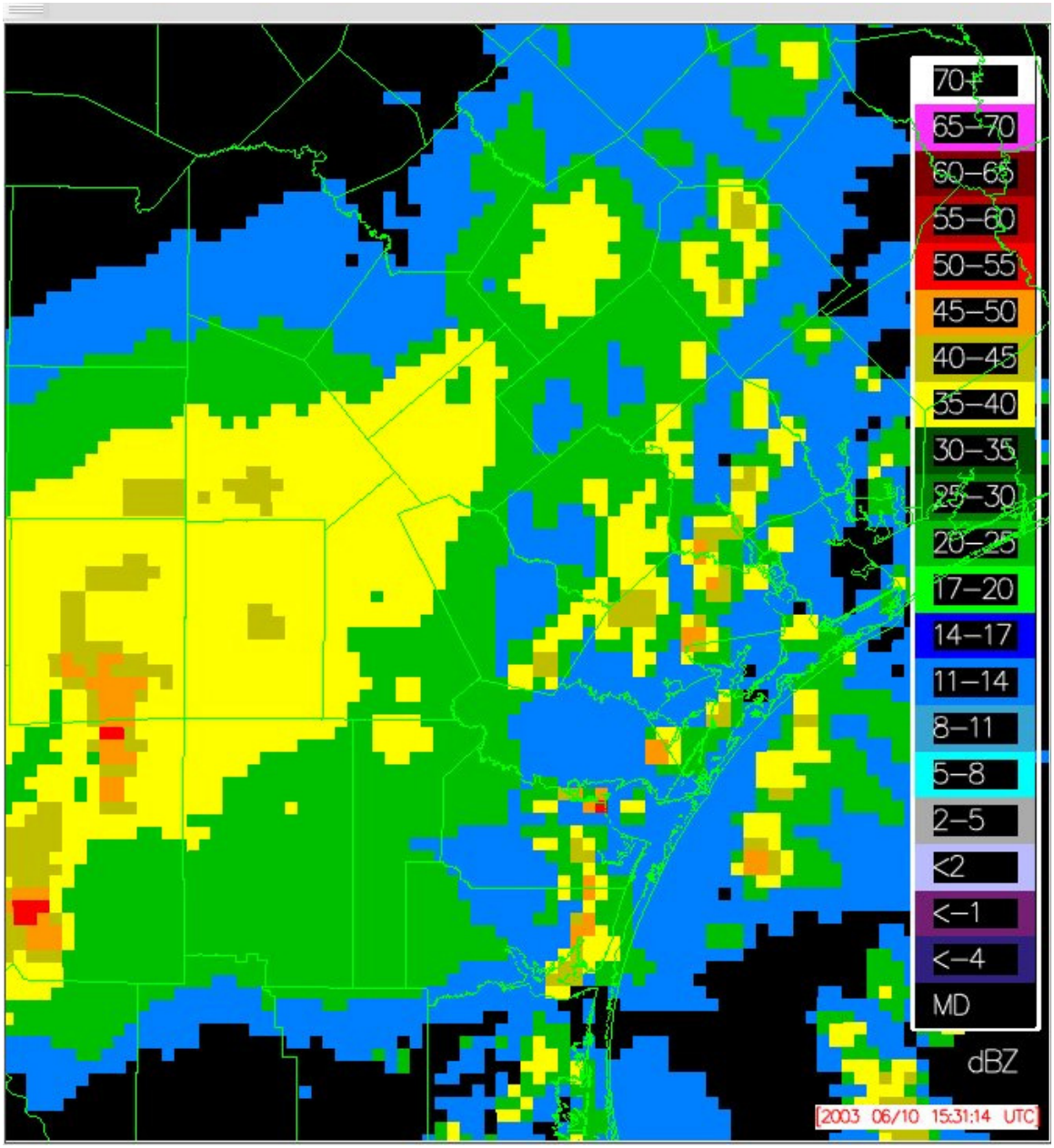

Figure 30. Same as Fig. 29 except for the ORPG AP-edited Composite Reflectivity Product 96.

Smalley, D. J. and B. J. Bennett, 2001: Recommended Improvements to the Open RPG AP-Edit Algorithm. Wx Project Memorandum No. 43PM Wx-0081, 45 pp.

b) Planned Efforts

Continue investigation of data quality issues as pertains to WARP applications.

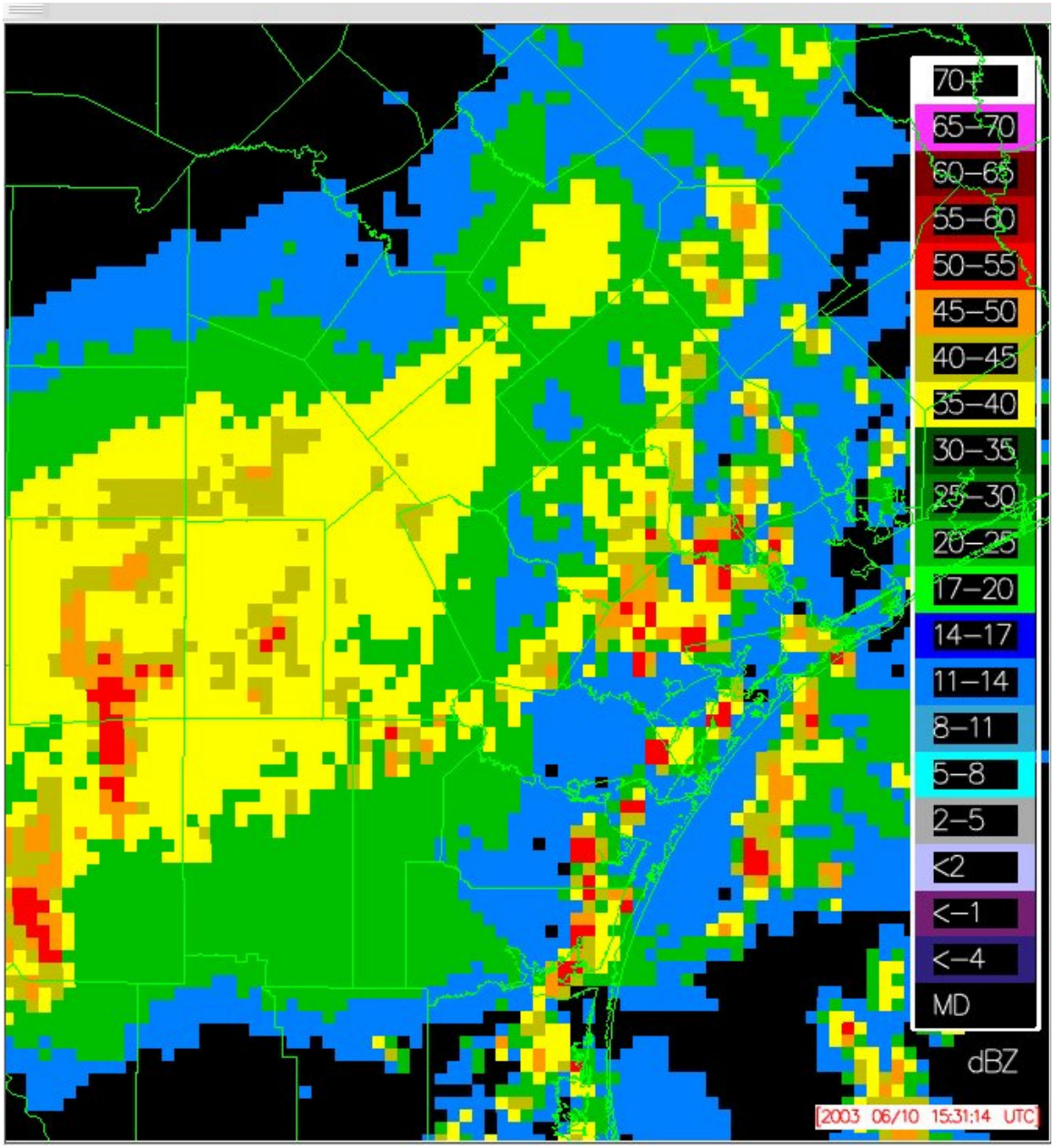

Figure 31. Same as Fig. 30 except that the median filter is not used.

c) Problems/Issues

None.

d) Interface with other Organizations

None.

e) Activity Schedule Changes

None.

1. Description of the classification algorithm

One of the important advantages of polarimetric weather radars is their ability to discriminate between different types of hydrometeor and non-hydrometeor radar scatterers. Our classification algorithm is based on the principles of fuzzy logic outlined in (Vivekanandan et al. 1999, Zrnic and Ryzhkov 1999, Straka et al. 2000, Liu and Chandrasekar 2000, Zrnic et al. 2001). According to fuzzy logic methodology, different hydrometeor classes are described by one-dimensional or two-dimensional membership functions that are expressed as follows:

$$F^{(i)}(V_j) = P^{(i)}(V_j) \qquad (1)$$

or

$$F^{(i)}(Z,V_j) = P^{(i)}(Z)\, P_Z^{(i)}(V_j) \qquad (2)$$

In (1) and (2), Z is the radar reflectivity factor at horizontal polarization and V_j is the value of the jth additional radar variable (polarimetric or non-polarimetric). One-dimensional unconditional membership functions $P^{(i)}(Z)$ and $P^{(i)}(V_j)$ characterize probability distributions of Z and V_j for the ith class, whereas the membership functions $P_Z^{(i)}(V_j)$ characterize conditional probability distribution of the variable V_j for the ith class for a given Z. The product of $P^{(i)}(Z)$ and $P_Z^{(i)}(V_j)$ represents the two-dimensional membership function characterizing joint probability distribution of Z and V_j in the Z – V_j plane for the ith class. One-dimensional membership functions generally have asymmetric trapezoidal shape with maximal value of 1 and minimal value of 0 (Fig. 1). These trapezoidal functions are described by 4 parameters: x1, x2, x3, and x4 as shown in Fig. 1.

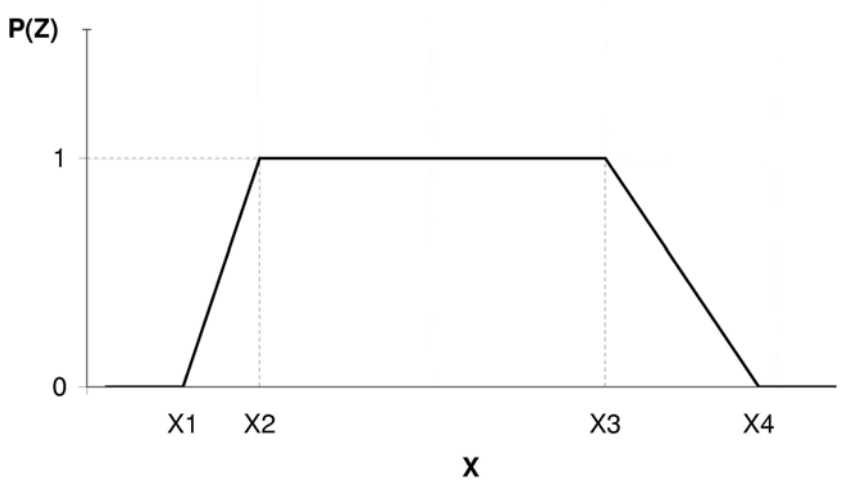

Fig. 1 Trapezoidal membership function

Aggregation value for each class is defined as:

$$Q_i = \sum_{j=1}^{M} W_j\, F^{(j)}(Z, V_j), \qquad (3)$$

where W_j is the weight assigned to the jth variable and M is the number of variables. Hydrometeor class is identified by the maximal aggregation value.

In our classification analysis, we use both Eq (1) and (2) to determine the membership functions $F^{(i)}$. The choice of Eq (2) is preferable if the probability distribution of the variable V_j strongly depends on the radar reflectivity as a parameter. This is usually the case for differential reflectivity Z_{DR} in rain, i.e., Z_{DR} increases with increasing Z.

Five radar variables have been used for automatic classification so far. They are: (1) radar reflectivity Z, (2) differential reflectivity Z_{DR}, (3) cross-correlation coefficient ρ_{hv} between horizontally and vertically polarized components of the radar return, (4) a texture parameter SD(Z) of the Z field, and (5) a texture parameter SD(Φ_{DP}) of the field of differential phase Φ_{DP}. The two latter variables are especially efficient for discrimination between meteorological and non-meteorological radar echoes. The parameters SD(Z) and SD(Φ_{DP}) characterize the depth of small-scale fluctuations of Z and Φ_{DP} along the radar ray. To obtain SD(Z), we average raw Z data (sampled every 0.256 km) along the radial using 1-km-width running average window and subtract the smoothed estimates of Z from their original values. Similar procedure is used for computing the parameter SD(Φ_{DP}) but with two times wider averaging window.

Two polarimetric variables, Z_{DR} and ρ_{hv}, are smoothed along the radial using averaging windows of 5 gates. Both Z_{DR} and ρ_{hv} should be corrected for noise prior to application of the classification algorithm. This is especially important for light rain, snow, and clear-air echoes caused by biological scatterers. Z_{DR} and ρ_{hv} are noticeably biased if signal-to-noise ratio (SNR) is less than 20 dB. Efficient correction of both variables can be made for SNR > 5 dB. If SNR < 5 dB, then correction is considered unreliable and no classification is performed at pixels with SNR < 5 dB.

Because the Sigmet RVP7 processor does not provide SNR directly, we estimate SNR from radar reflectivity factor Z and distance R using the following formula

$$\mathrm{SNR\ (dB)} = Z(\mathrm{dBZ}) - 20\log(R(\mathrm{km})) + C \quad , \qquad (4)$$

where the "constant" C is usually between 27 and 33. The value of C for a particular day of observations can be estimated using the scatterplots $\rho_{hv}^{(cor)}$ – SNR, where $\rho_{hv}^{(cor)}$ is the value of the cross-correlation coefficient corrected for noise as

$$\rho_{hv}^{(cor)} = \rho_{hv}\,(1 + 1/\mathrm{snr})\ . \qquad (5)$$

In (5) $\mathrm{snr} = 10^{0.1\ \mathrm{SNR\ (dB)}}$. If the constant C is estimated correctly, then the scattergram $\rho_{hv}^{(cor)}$ – SNR is "flat" , i.e., there is no apparent dependence of $\rho_{hv}^{(cor)}$ on SNR for SNR > 5 dB. Such tuning of the constant C is performed automatically during data processing.

Correction of Z_{DR} for noise is made according to formula

$$Z_{DR}^{(cor)}(\mathrm{dB}) = 10\log[(\alpha\ \mathrm{snr}\ Z_{dr})/(\alpha\ \mathrm{snr} + \alpha - Z_{dr})] \quad , \qquad (6)$$

where $Z_{dr} = 10^{\ 0.1\ \mathrm{ZDR(dB)}}$ and α is a ratio of noises in the horizontal and vertical channels. In the current version of the classification algorithm, $\alpha = 1.48$ and $10\log(\alpha) = Z_{DR}^{(noise)} = 1.7$ dB.

The classification procedure can be customized according to the user needs. Depending on the primary task, different sets of radar variables, different classes, and different weight vectors **W** can be used in the classification routine. For example, the algorithm can be optimized either for discrimination between meteorological and non-meteorological scatterers (meteo versus non-meteo) or for distinguishing different categories of meteorological echo (e.g., rain versus hail or snow).

At the moment, we use three different versions of the polarimetric classification algorithm with different degree of sophistication. Classification is performed with the data collected at one or two lowest elevations (0.5º and 1.5º). The same classification principles can be applied to the data obtained in vertical cross-section. However, since the RHI antenna scanning is not accepted in the NEXRAD mode of operation, the identification of radar echoes at two lowest PPI scans was our primary task during JPOLE.

1.1. Version 1. Meteorological versus non-meteorological scatterers.

Version 1 represents a simplest type of the classification algorithm that proves to be very efficient to discriminate between radar echoes caused by meteorological and non-meteorological scatterers such as ground clutter / anomalous propagation (AP), insects, birds, bats, and chaff. Three classes are identified according to this classification scheme: (1) hydrometeors of meteorological origin, (2) ground clutter / AP, and (3) non-meteorological scatterers in atmosphere (insects, birds, bats, and chaff). All five radar variables are used for identification. The parameters x1 – x4 describing five one-dimensional membership functions for three classes are presented in Table 1. These functions are also displayed graphically in Fig. 2.

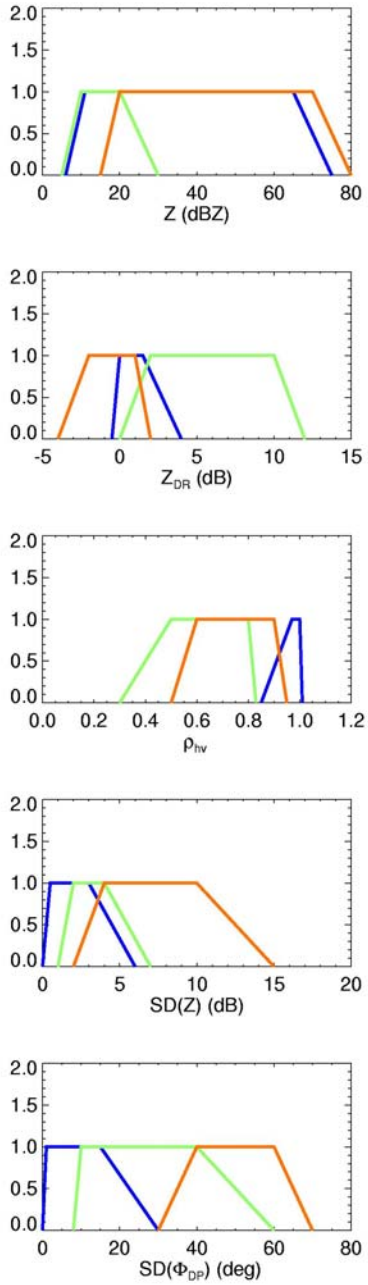

Fig. 2 Membership functions characterizing three classes: (1) meteorological scatterers (blue lines), (2) biological scatterers (green lines) , and (3) ground clutter / anomalous propagation (red lines) with 5 radar variables.

Table 1. Parameters of the membership functions for three classes.

P(Z)			
	GC/AP	BS	MS
X1 (dB)	15	5	5
X2 (dB)	20	10	10
X3 (dB)	70	20	65
X4 (dB)	80	30	75
$P_Z(Z_{DR})$			
X1 (dB)	-4	0	fl – 0.3
X2 (dB)	-2	2	fl
X3 (dB)	1	10	fh
X4 (dB)	2	12	fh +0.3
$P(\rho_{hv})$			
X1	0.5	0.3	0.85
X2	0.6	0.5	0.97
X3	0.9	0.8	1.0
X4	0.95	0.83	1.01
P(SD(Z))			
X1 (dB)	2	1	0
X2 (dB)	4	2	0.5
X3 (dB)	10	4	3
X4 (dB)	15	7	6
$P(SD(\Phi_{DP}))$			
X1 (deg)	30	8	0
X2 (deg)	40	10	1
X3 (deg)	50	40	15
X4 (deg)	60	60	30

In Table 1, GC/AP stands for ground clutter /anomalous propagation, BS – for biological scatterers, and MS – for meteorological scatterers; fl and fh are functions of radar reflectivity

$$fl = -0.50 + 2.50\ 10^{-3}\ Z + 7.50\ 10^{-4}\ Z^2 \qquad (7)$$

$$fh = 0.08 + 3.64\ 10^{-2}\ Z + 3.57\ 10^{-4}\ Z^2 \quad , \qquad (8)$$

where Z is expressed in dBZ.. One –dimensional membership functions $F^{(i)}(V_j)$ as defined by Eq (1) are used for all variables and all classes. The only exception is made for the membership function $F(Z,Z_{DR})$ of the meteorological scatterers that is defined according to (2). Equal weights are given to all five radar variables in Eq (3).

1.2 Version 2. The "summer" classification algorithm

Version 2 of the classification algorithm enables discrimination between radar echoes caused by (1) ground clutter and AP, (2) biological scatterers, (3) "big drops", (4) light rain, (5) moderate rain, (6) heavy rain, and (7) rain / hail mixture. Notification "big drops" is used for rain that is characterized by the dominance of big drops and deficit of small drops in raindrop spectrum. This very special type of drop size distribution (DSD) is usually observed in the zones of rapidly developing convection and has important prognostic value for weather forecasters. Three radar variables: Z, Z_{DR}, and ρ_{hv} are used for classification. Historically, this is the earliest version of the classification algorithm and several examples of classification presented in section 4 of this report were obtained using this version of the algorithm. Two texture variables, SD(Z) and SD(Φ_{DP}), will be added later.

Two-dimensional membership functions $F^{(i)}(Z,V_j)$ determined from (2) are used in this version of the classification algorithm. The parameters of the membership functions for all 7 classes are presented in Table 2.

Table 2. Parameters of the membership functions for seven classes in the "summer" classification algorithm.

P(Z)							
	GC/AP	BS	BD	LR	MR	HR	R/H
x1 (dB)	25	5	15	5	30	40	45
x2 (dB)	35	15	20	10	35	45	50
x3 (dB)	75	20	45	35	45	55	75
x4 (dB)	85	30	50	40	50	60	80
$P_Z(Z_{DR})$							
x1 (dB)	-5	1	fh-0.3	fl-0.3	fl-0.3	fl-0.3	-0.3
x2 (dB)	-3	3	fh	fl	fl	fl	0
x3 (dB)	0	7	fb	fh	fh	fh	fl
x4 (dB)	2	9	fb+0.3	fh+0.3	fh+0.3	fh+0.3	fl+0.3
$P_Z(\rho_{hv})$							
x1	0.45	0.45	0.89	0.89	0.89	0.89	0.84
x2	0.55	0.55	0.90	0.90	0.90	0.90	0.85
x3	0.80	0.80	1.00	1.00	1.00	1.00	0.96
x4	0.90	0.90	1.01	1.01	1.01	1.01	0.97

In Table 2, GC/AP stands for ground clutter / anomalous propagation, BS – for biological scatterers, BD – for big drops, LR – for light rain, MR – for moderate rain, HR – for heavy rain, R/H – for rain/hail mixture; fl and fh are defined by (7) and (8); fb is another function of radar reflectivity:

$$fb = -0.20 + 0.108\, Z - 6.43\, 10^{-4}\, Z^2 \quad , \qquad (9)$$

where Z is expressed in dBZ. Equal weights $W_1 = 1$ and $W_2 = 1$ are given to the membership functions associated with Z_{DR} and ρ_{hv} in Eq (3).

Note that the parameters of similar membership functions in Table 1 and Table 2 might be different because the classification procedure continuously evolved during the JPOLE period. Therefore, earlier and later versions of the classification algorithm differ in details. For each classification example in this report, we clearly specify particular version of the classification routine.

1.3 Version 3. The "winter" classification algorithm.

In the version of the classification algorithm that was used for cold season weather events, we add two categories of snow particles, dry and wet snow, to the list of classes and use the texture parameter of the Z field SD(Z) together with Z, Z_{DR}, and ρ_{hv}. This version of the classification algorithm enables discrimination between radar echoes caused by (1) ground clutter and anomalous propagation, (2) biological scatterers (including insects and birds), (3) dry snow, (4) wet snow, (5) stratiform rain, (6) convective rain, and (7) rain/hail mixture.

Table 3 contains parameters of the membership functions for the "winter" classification algorithm. As in version 2, the two-dimensional membership functions defined from (2) are utilized.

Table 3. Parameters of the membership functions for seven classes in the "winter" classification algorithm.

P(Z)							
	GC/AP	BS	DS	WS	SR	CR	R/H
x1 (dB)	25	5	5	15	5	38	48
x2 (dB)	35	15	10	25	10	43	53
x3 (dB)	75	20	25	35	43	53	75
x4 (dB)	85	30	30	45	48	58	80
$P_Z(Z_{DR})$							
x1 (dB)	-5	0	-0.3	0.6	fl-0.3	fl-0.3	-0.3
x2 (dB)	-3	3	0	1.0	fl	fl	0.0
x3 (dB)	0	7	0.3	1.8	fb	fb	fl
x4 (dB)	2	10	0.6	2.2	fb+0.3	fb+0.3	fl+0.3
$P_Z(\rho_{hv})$							
x1	0.45	0.45	0.93	0.83	0.97	0.96	0.84
x2	0.55	0.55	0.94	0.85	0.98	0.97	0.85
x3	0.70	0.70	0.97	0.94	1.00	1.00	0.96
x4	0.80	0.80	0.98	0.96	1.01	1.01	0.97
$P_Z(SD(Z))$							
x1 (dB)	4	1	-0.5	0	-0.5	-0.5	-0.5
x2 (dB)	6	2	0.5	1	0.5	0.5	0.5
x3 (dB)	30	4	3	3	2.5	2	2
x4 (dB)	32	5	4	4	3.5	3	3

In Table 2, GC/AP stands for ground clutter / anomalous propagation, BS – for biological scatterers, DS – for dry snow, WS – for wet snow, SR – for stratiform rain, CR

– for convective rain, and R/H – for rain / hail mixture; functions fl(Z) and fb(Z) are defined by Eq (7) and (9).

Several classes of radar scatterers have very distinctive polarimetric properties and can be recognized easily if the fuzzy logic methodology is applied on a pixel-by-pixel basis. This means that no analysis of general pattern or surrounding pixels of data is needed. Ground clutter / AP, insects, birds, chaff, hail, wet snow (bright band) belong to this category of scatterers. All of them are characterized by anomalously low values of cross-correlation coefficient. Differential reflectivity is mainly negative for ground clutter / AP, very high positive for biological scatterers and chaff, and moderately high for wet snow. Combination of high Z and relatively low Z_{DR} is a distinctive feature of hail or rain/hail mixture. SD(Z) is usually much higher for non-meteorological scatterers (especially for ground radar returns) than for any weather hydrometeors.

A major problem is discrimination between stratiform rain and dry aggregated snow for which membership functions in the fuzzy logic formalism are heavily overlapped. Both classes are characterized by relatively low Z and Z_{DR} combined with high ρ_{hv} (Ryzhkov and Zrnic 1998). Furthermore, there is no distinction in terms of the texture of the Z field as well.

Fig. 3 illustrates three scatterplots of Z versus Z_{DR} obtained from the measurements with the KOUN radar for three different types of snow. Dry aggregated

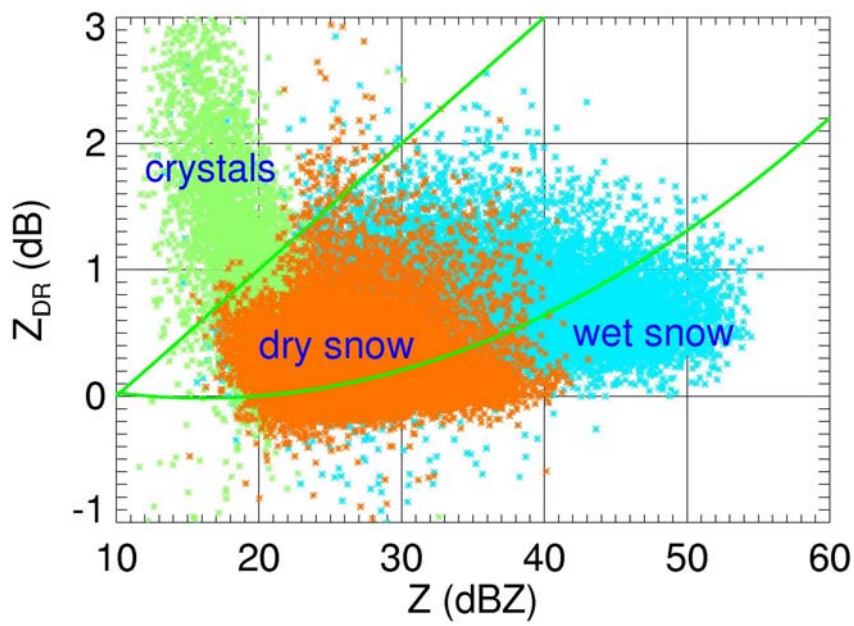

Fig. 3 Z – Z_{DR} scatterplots for different types of snow. Two curves confine "rain" area.

snow was observed on 6 February 2003 between 15 and 16 Z over the whole state of Oklahoma. Seven hours later, dry aggregated snow changed to more crystallized snow in a very cold air NW of the radar. It was characterized by much higher Z_{DR} and lower Z. Heavy convective snowfall occurred on 24 February 2003 in southern Oklahoma. The corresponding Z – Z_{DR} scatterplot for the period between 22 and 24 Z is also displayed in Fig. 3. Radar reflectivities over 50 dBZ are unusually high for snow in the latter case, but corresponding values of Z_{DR} are relatively low compared to the ones typically observed at the bottom of the bright band. The region between two curves in Fig. 3 represents

locations of $Z - Z_{DR}$ pairs for pure rain as derived form the multi-year statistics of DSD measurements in central Oklahoma.

It is evident that rain and snow are heavily overlapped in the $Z - Z_{DR}$ plane for reflectivities between 20 and 40 dBZ. There is no clear distinction between these two classes in K_{DP} and ρ_{hv} as well. A clue for successful discrimination between these classes lies in the fact that stratiform rain and aggregated snow are usually separated by the bright band that has very pronounced polarimetric signatures and can be easily detected. Therefore, rain / snow delineation is contingent on reliable identification of the bright band.

Although it is easier to perform bright band identification at RHI, we have to do classification at PPIs because RHI antenna scanning is not accepted in the NEXRAD mode of operations. Fig. 4 and 5 demonstrate how the melting level is exhibited in the fields of Z, Z_{DR}, and ρ_{hv} at two lowest elevation tilts: 0.5 and 1.5° in the case of a stratiform rain with relatively low bright band.

At both elevations, radar reflectivity gives little clue about location and height of the melting level. The bright band signature is more pronounced in the Z_{DR} fields, particularly at higher elevation. However, the best indication of the melting level is given by ρ_{hv} at 1.5°. The cross-correlation coefficient drops abruptly from 0.99 to less than 0.96 at the slant range where a radar beam intersects the bottom of the melting layer. After dropping in the melting layer, ρ_{hv} tends to increase in dry snow aloft. This increase, however, might be masked with a general decrease of ρ_{hv} with range due to weakening of radar signal and broadening of the radar beam. It can be shown that ρ_{hv} is negatively biased if signal-to-noise ratio is less than 20 dB. The same is true for Z_{DR}. Thus, the appropriate correction of ρ_{hv} and Z_{DR} at low SNR is crucial for rain / snow discrimination.

In the current version of the classification algorithm, slant ranges separating rain and melting snow are determined at every azimuth from the radial profiles of corrected ρ_{hv} at the elevation of 1.5°. After some editing and median filtering in azimuth, the "bright band contour" is generated at 1.5°. The corresponding "bright band contour" at lower elevation is obtained from the one at 1.5° using simple geometric considerations and an assumption of horizontal uniformity. Then traditional "fuzzy logic" approach is applied for classification on a pixel-by-pixel basis at both elevations using all available radar variables. However, categories of rain and non-meteorological scatterers are prohibited beyond the "bright band contour" where snow is expected. Similarly, snow is not allowed to appear below bright band.

The bottom panel of Fig. 5 represents results of rain / snow discrimination for the case of 10/24/02.

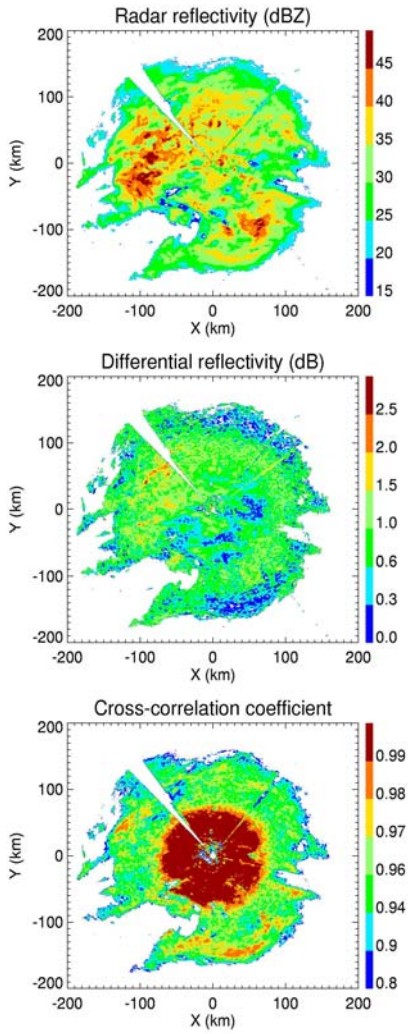

Fig. 4 Composite plot of Z, Z_{DR}, and ρ_{hv} at El = 1.5º for stratiform rain on 24 October 2002 (1832 Z).

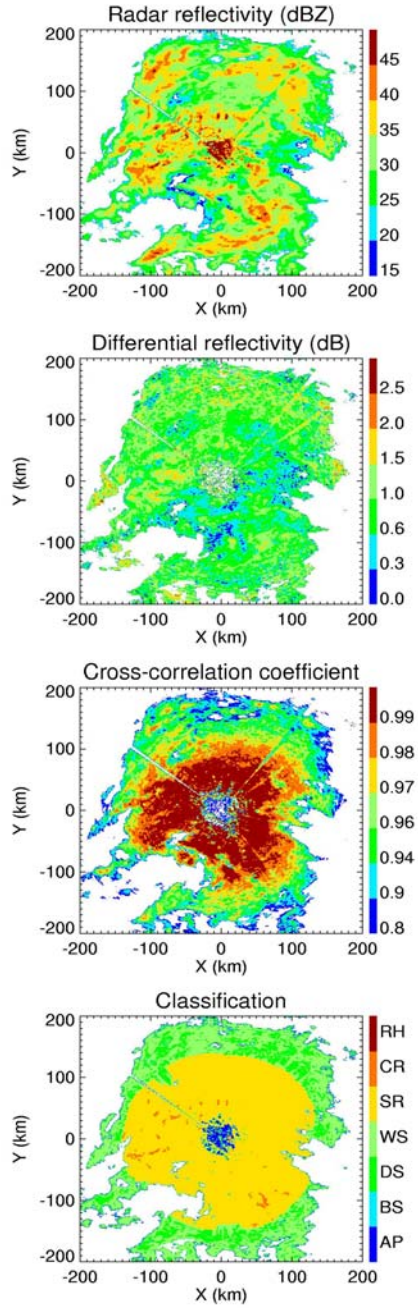

Fig. 5 Composite plot of Z, Z_{DR}, ρ_{hv} and results of classification at El = 0.5º for stratiform rain on 24 October 2002 (1832 Z).

2. Improvement in data quality

There are several data quality issues that can be addressed with a dual-polarization radar. Here we mention at least three of them for which we claim apparent improvement judging from the JPOLE data.

2.1 Filtering out non-meteorological echoes.

In most weather-related applications the users prefer to work with the fields of radar variables that are not contaminated with echoes of non-meteorological origin such as ground clutter / AP, insects, birds, bats, chaff, etc. Meteorological and non-meteorological scatterers possess very distinctive polarimetric properties. A detailed description of polarimetric contrasts between weather and non-weather radar echoes with several supporting examples is given in section 4.5.

In order to assess the capability of the KOUN radar to classify meteorological and non-meteorological scatterers, we have selected 8 cases with extensive areas of radar echo caused by either AP or biological scatterers. A list of these cases is presented in Table 4. Additional information about the selected cases can be found at (Pam's web site)

Table 4. List of the JPOLE cases with the most pronounced non-meteorological echoes.

Number	Date	Time (UTC)	Description
1	06/13/2002	3 - 9	AP in the rear side of MCS
2	08/13/2002	9 - 11	AP and Bio mixed with rain
3	08/24/2002	6 - 9	AP and Bio mixed with rain
4	08/28/2002	11 - 14	Widespread AP, no rain
5	09/15/2002	1 - 8	Migratory birds and rain
6	10/27/2002	2 - 9	Migratory birds and rain
7	10/29/2002	5 - 13	Migratory birds and light rain
8	05/01/2003	9 - 12	Very strong and extended AP

For each case, we perform echo classification every 6 to 15 minutes at the two lowest elevation tilts, 0.5º and 1.5º, using the version 1 of the classification algorithm. Three classes of radar echo: hydrometeors, biological scatterers, and ground clutter / AP are distinguished. The radar data and results of classification for both elevations are displayed and stored for the 400 x 400 km area in Cartesian format with resolution 2 x 2 km. For each event, we examined animations of the fields of classified echoes to check spatial and temporal continuity of the classification results. This visual continuity test shows good spatial / temporal "coherency" of the classification fields and their consistency with what one has to expect from common sense.

To our knowledge, there is no well established methodology for quantitative assessment of the performance of such classification procedures. Accurate ground truth validation is not possible because of lack of verification data at such small spatial and temporal scale. Rain gage information can be useful just to determine fact of rain in the close proximity of the gage. Satellite data analysis is another option to assess the

possibility of rain or AP over large areas (however, with coarse spatial and temporal resolution). Validation information regarding biological scatterers and their flying habits is also very limited. In some previous studies (Moszkovicz et al. 1994) an "assessment of well-trained radar operator" was used as a ground truth to validate different techniques for AP detection and mitigation. This criterion is quite subjective and, unfortunately, there is no simple way to avoid certain degree of subjectivity for such type of validation. Our approach to validate the capability of the classification scheme to recognize meteorological and non-meteorlogical echo is also not void of subjectivity.

We select certain areas of the radar echo at both elevation tilts which should contain only weather or non-weather echoes and count the number of 2 x 2 km pixels identified as "meteo" or "non-meteo" in these areas. The distances too close from the radar and the areas of complex mixture of the echoes from AP, biological, and meteorological scatterers have been avoided. We have identified such "test" areas practically for all examined events and examine multi-hour statistics of classification for each of these areas. The number of pixels identified as "non-meteo" in pure rain areas was usually less than 1% of the total number of pixels for which SNR > 10 dB. Similar proportion of misclassification (less than 1 %) was found in an opposite situation - "meteo" pixels in the AP areas - provided that SNR is again higher than 10 dB. The quality of classification deteriorates with decreasing SNR (up to 5% of misclassified pixels in several cases if SNR > 5 dB). This deterioration is attributed to the fact that key polarimetric variables Z_{DR} and ρ_{hv} are biased by noise and their reliable correction for noise is possible only for SNR > 5 – 10 dB. The use of total differential phase Φ_{DP} which is not affected by noise is more promising at relatively weak signals. This option will be carefully exploited in the near future. The major problem, however, will be the separation of the contributions from the forward scattering and backscattering effects in the total differential phase. Only the "backscattering portion" of Φ_{DP} should be used for classification.

2.2 The accuracy of radar reflectivity measurements.

Once the sources of radar echo are identified and "unwanted" echoes are filtered out, the next problem is to ensure high accuracy of the radar reflectivity measurements. Radar reflectivity factor Z can be biased due to radar miscalibration, partial beam blockage, and attenuation in rain and hail. The latter factor was usually widely ignored at S band. Ryzhkov and Zrnic (1995) showed that for extended regions of heavy precipitation typical for Great Planes the Z bias due to attenuation can be significant. It was shown, that in pure rain (without hail) such bias at S band can be approximately estimated from Φ_{DP}:

$$\Delta Z \text{ (dB)} = 0.04\ \Phi_{DP} \text{ (deg)} \qquad (10)$$

Those observational results were supported by theoretical simulations by Bringi et al. (1990). Measured differential phases exceeding 100º are very common for precipitation in Oklahoma. This means that negative biases of Z over 4 dB in magnitude occur quite frequently at long propagation paths in precipitation. Such biases cause in about two times underestimation of rain rate if the conventional NEXRAD relation is utilized and

poor hail detection at large distances form the radar. Good example of significant attenuation along a squall line passing the KOUN radar is presented in Fig. 6. In this

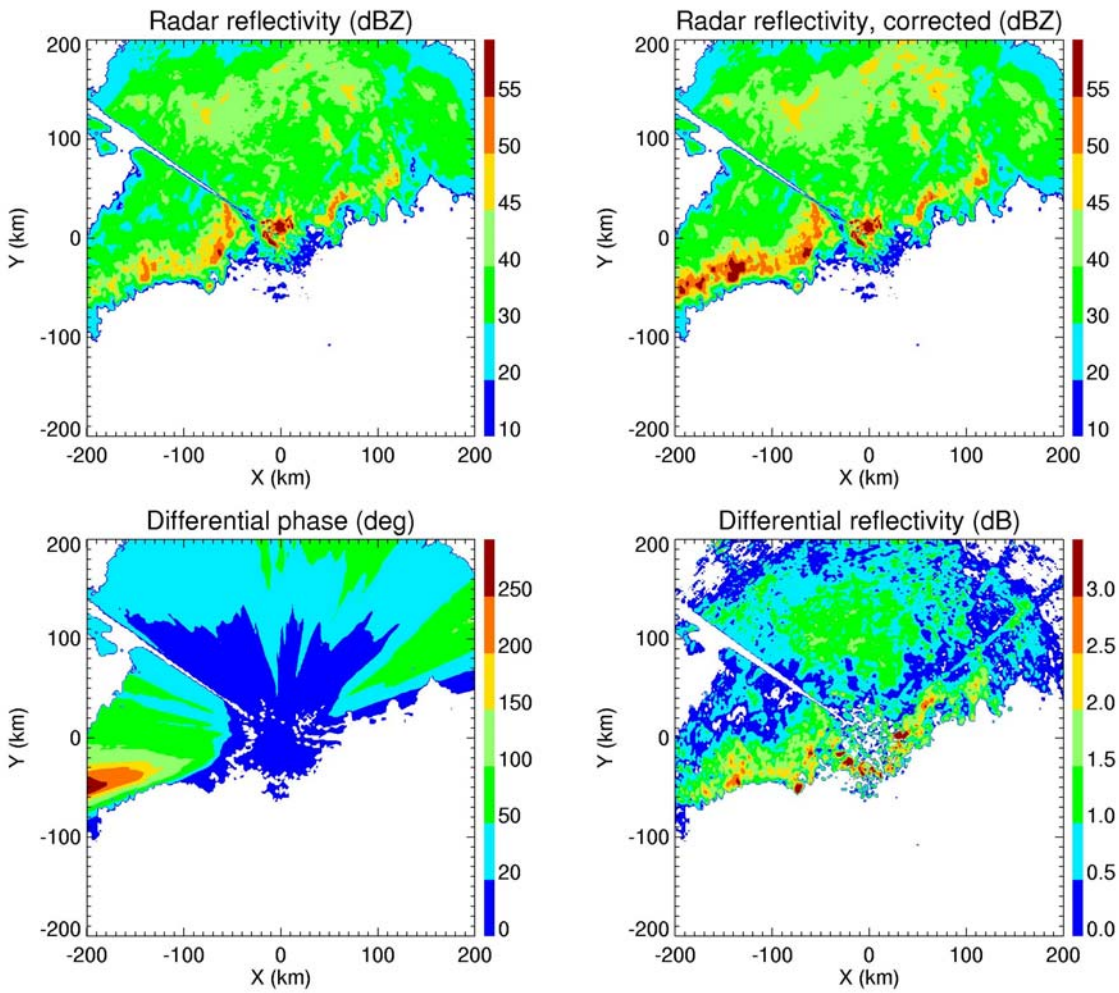

Fig. 6. Correction of radar reflectivity for attenuation using differential phase. 16 June 2002, 0201 UTC, El = 0.5º

example differential phase exceeds 250º in the western part of a squall line and the corresponding bias of Z is larger than 10 dB! Gradual decrease of Z with range along the squall line is quite obvious in Fig. 6a. As a result, hail at large distances from the radar is not identified. The problem is fixed if radar reflectivity is corrected according to Eq (10) (Fig. 6b). Attenuation in hail is much more significant than in rain and the coefficient of proportionality in (10) is even higher in the presence of hail on the propagation path.

Accurate calibration of radar reflectivity factor still remains a serious problem at the WSR-88D radar network. Recent findings by Gourley et al (2003) show that the Z biases of 2 – 3 dB are quite common. The problem of accurate measurements of Z is further exacerbated at lowest elevations whereby a radar beam can be partially blocked. One of the great advantages of a dual-polarization radar is its capability to measure specific differential phase K_{DP} that is immune to radar system miscalibration, beam blockage, and attenuation in precipitation. In (Goddard et al. 1994, Gorgucci et al. 1999),

the idea of self-consistency among Z, Z_{DR}, and K_{DP} was suggested to assess possible biases in Z. According to this approach, Z, Z_{DR}, and K_{DP} are not independent variables in rain, and Z at horizontal polarization can be roughly estimated from Z_{DR} and K_{DP} using the following relation

$$Z = a + b \log(K_{DP}) + c\, Z_{DR}\,, \qquad (11)$$

where Z is expressed in dBZ, Z_{DR} - in dB, and K_{DP} – in deg/km. The coefficients a, b, and c in (11) depend on a radar wavelength and are relatively insensitive to the drop size distribution (DSD) variations. We used the multiyear statistics of DSDs in central Oklahoma measured with the 2D-video disdrometer to compute radar variables at the wavelength of 11 cm and obtained the following coefficients in (11): a = 48.5, b = 11.4, and c = 0.94. In a companion report (Ryzhkov et al. 2003), we examined the performance of the suggested polarimetric consistency technique for radar reflectivity calibration via direct comparisons of reflectivities measured by the KOUN radar and operational KTLX radar located at the distance of 20.3 km from the polarimetric one. For 19 rain events (out of total 22 examined) the difference between two estimates (polarimetric and direct) was within 1 – 1.5 dB. We believe that, after some additional refinements, the polarimetric consistency technique will provide the accuracy of the radar reflectivity measurements within 1 dB.

Specific differential phase K_{DP} does not require calibration, whereas differential reflectivity Z_{DR} does. However, since Z_{DR} is a relative parameter (a ratio), it is easier to calibrate Z_{DR} than Z. As shown by Melnikov et al. (2003), the bias of Z_{DR} was kept under 0.2 dB for the KOUN measurements during JPOLE. According to the consistency relation (11), the Z_{DR} measurement error of 0.2 dB causes the corresponding error of Z calibration less than 0.2 dB. Differential reflectivity measurements can be biased more significantly if the radar beam at lowest elevation is partially blocked (Ryzhkov et al. 2002). This is the case for the NSSL's research Cimarron polarimetric radar. Ryzhkov et al. (2002) have developed methodology for calibration of Z_{DR} in the presence of severe beam blockage. After Z_{DR} is appropriately calibrated, Eq (11) can be applied to obtain unbiased radar reflectivity factor even in the case of substantial blockage of the radar beam (Ryzhkov et al. 2003).

2.3 Doppler wind measurements in clear air

All methods for Doppler wind measurements in clear atmosphere assume that clear-air radar scatterers are ideal tracers of wind and turbulence, i.e., they do not have their own component of motion. Biological scatterers like insects, birds, and bats represent overwhelming majority of the clear-air scatterers (along with small-scale nonuniformities of refractive index caused by turbulence). If these biological scatterers are strong flyers, they produce a bias in Doppler wind estimates that needs to be eliminated from meteorological analysis. It is important to distinguish between passive (mostly insects) and non-passive tracers of winds (birds and bats) in order to guarantee acceptable quality of radar wind retrievals in clear atmosphere such as VAD (Velocity – Azimuth Display). It is very common that the VAD wind profiles obtained during peaks of nocturnal bird migration in spring and fall are heavily contaminated. Zrnic and

Ryzhkov (1998) were the first who showed significant differences in polarimetric properties of small Rayleigh scatterers like insects and big non-Rayleigh scatterers like birds. Birds usually have much larger differential phase upon scattering δ and lower differential reflectivity Z_{DR} than insects.

At the moment, all versions of our classification algorithm do not make distinction between insects and birds and both types of biological scatterers are combined in the same class "biological scatterers". One of the reasons for that is that polarimetric signatures of birds and insects have very pronounced azimuthal dependence and at certain azimuths (usually close to the main wind direction) Z_{DR} and δ for birds and insects are very similar. Therefore, their discrimination based on pixel-to-pixel fuzzy logic approach might not be efficient at these azimuthal directions. Nevertheless, there are extended areas of radar echo where such classification can be performed in very clear and straightforward way. In other words, the areas of high δ (of the order of 70 - 100º) and relatively small Z_{DR} (usually lower than 3 dB) associated with birds can be easily identified and the corresponding sectors of wind fields retrieved using the VAD technique should be flagged.

Section 4 contains more detailed description of polarimetric signatures of insects and birds as well as some graphical examples of the differences between them.

3. Winter storms

The KOUN radar collected polarimetric data for 4 snow storms during JPOLE: on 3 – 4 December 2002, 6 February 2003, 23 February 2003, and 24 February 2003. These snow events encompass wide variety of different snow types including heavy convective wet snow associated with intense electrical activity (24 February 2003), crystallized snow in very cold air pool (6 February 2003), and more common aggregated dry snow observed on 3 – 4 December 2002 and 23 February 2003. Some results of preliminary polarimetric analysis of the snow storms occurred on 3 – 4 December 2002 and 24 February 2003 are reported by Ryzhkov and Zrnic (2003), Scharfenberg and Maxwell (2003), and Miller and Scharfenberg (2003).

The performance of the classification algorithm is demonstrated for the winter storm on 3 – 4 December 2002 (Fig. 7). This storm was associated with the passage of a cold front accompanied by the transition from rain to freezing rain and snow in the Oklahoma City metropolitan area. During this event, the melting layer was slowly subsiding with much lower height of the bright band in the cold air pool N – NW from the radar. This feature is manifested by the pronounced asymmetry of the "rain" area with respect to the radar location.

At 1803 Z (12/03/02), differential reflectivity gives clear indication of the bright band in the northern sector. More precise determination of the bright band localization was possible from the ρ_{hv} data at the elevation of 1.5°. About nine hours later, the height of the melting layer remained almost the same in the southern sector, but noticeably decreased to the north from the radar (right column in Fig. 7). Note the bright band signature in the Z field associated with increase of Z_{DR} and drop in ρ_{hv} in that direction.

At 0302 Z (12/04/02), rain was recognized up to the distances 50 – 60 km at the lowest elevation scan NW from the radar. At the same time, surface temperature fell

below zero and freezing rain was reported on the ground. This freezing rain caused significant damage in the Oklahoma City metropolitan area.

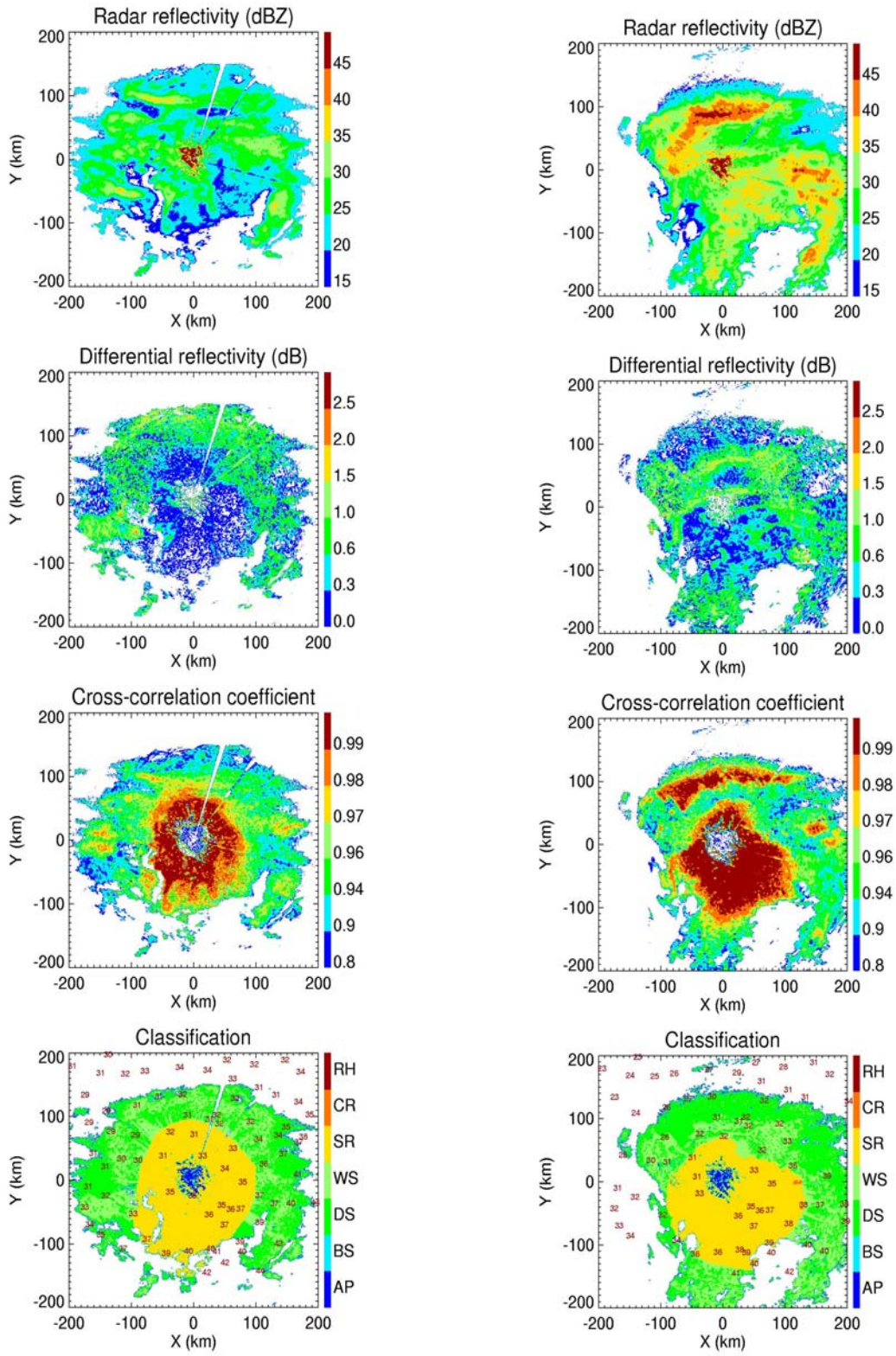

Fig. 7. Composite plots of Z, Z_{DR}, ρ_{hv}, and results of classification at El = 0.5º for the 3 – 4 December snow event (12/03/02, 1803 Z – left column, 12/04/02, 0302 Z – right column). Surface temperatures (Fº) are shown in the classification images.

Note that after dropping in the melting layer, the cross-correlation coefficient restored high values exceeding 0.99 at higher levels aloft where snow is dry (Fig. 8c). Corresponding lower values of Z_{DR} in dry snow are very similar to those observed in rain below the melting level. This again underlines importance of the bright band identification for separation between dry aggregated snow and light rain.

More detailed meteorological interpretation of polarimetric variables and its use by the forecasters at the Norman NWS office for this winter storm is described in the paper of Scharfenberg and Maxwell (2003).

4. Non-meteorological scatterers

The capability of the polarimetric radar to discriminate between meteorological and non-meteorological scatterers is demonstrated using the version 1 of the classification algorithm. As mentioned in section 1.1, this version allows discrimination between three classes of radar scatterers: meteorological, biological, and ground clutter / AP. Five radar variables are used for classification: radar reflectivity Z, differential reflectivity Z_{DR}, cross-correlation coefficient ρ_{hv}, the texture parameter of the radar reflectivity field SD(Z), and the texture parameter of the differential phase field SD(Φ_{DP}). The corresponding membership functions are represented graphically in Fig. 2. These membership functions were obtained after careful analysis of the scatterplots of multiparameter data collected for many hours during several days of observations.

All three classes are heavily overlapped in the Z domain (Fig. 2a). They are much better separated in terms of other four variables. Differential reflectivity of non-meteorological scatterers varies in wide range. Very high positive Z_{DR} values unambiguously signify biological scatterers (primarily insects), whereas negative Z_{DR}s indicate ground clutter / AP. The separation between the three classes based on the sole Z_{DR} is problematic if the measured Z_{DR} is between 0 and 2 dB (Fig. 2b)

The use of cross-correlation coefficient yields very good separation of meteorological and biological scatterers (Fig. 2c). The distinction between weather echoes and ground clutter /AP is not as clear in the ρ_{hv} domain. This can be explained by the fact that non-fluctuating radar signals from man-made targets are characterized by ρ_{hv} very close to 1 (similar to meteorological scatterers), whereas natural land covers (trees, grass, etc.) have very low ρ_{hv}. The cross-correlation of the mixture of man-made and natural scatterers depends on their relative contribution to the radar return in the particular radar resolution volume.

The texture of radar reflectivity (SD(Z)) that is widely used for AP detection with non-polarimetric radars (Kessinger et al. 2001, Steiner and Smith 2002) apparently has value to distinguish meteorological scatterers and ground clutter / AP, but it is not of a great help to isolate the radar echoes from precipitation and insects and birds. The texture of differential phase SD(Φ_{DP}) is more promising than SD(Z) for delineation of precipitation and AP and shows less overlap between meteorological and biological scatterers (Fig. 2d,e).

Although none of the five radar variables enables perfect delineation between three classes, their combination is very efficient if the fuzzy logic approach is used for classification. This complementary character of multiparameter information is illustrated in Fig. 8 where the fields of 6 variables are displayed at the lowest elevation tilt of 0.5º

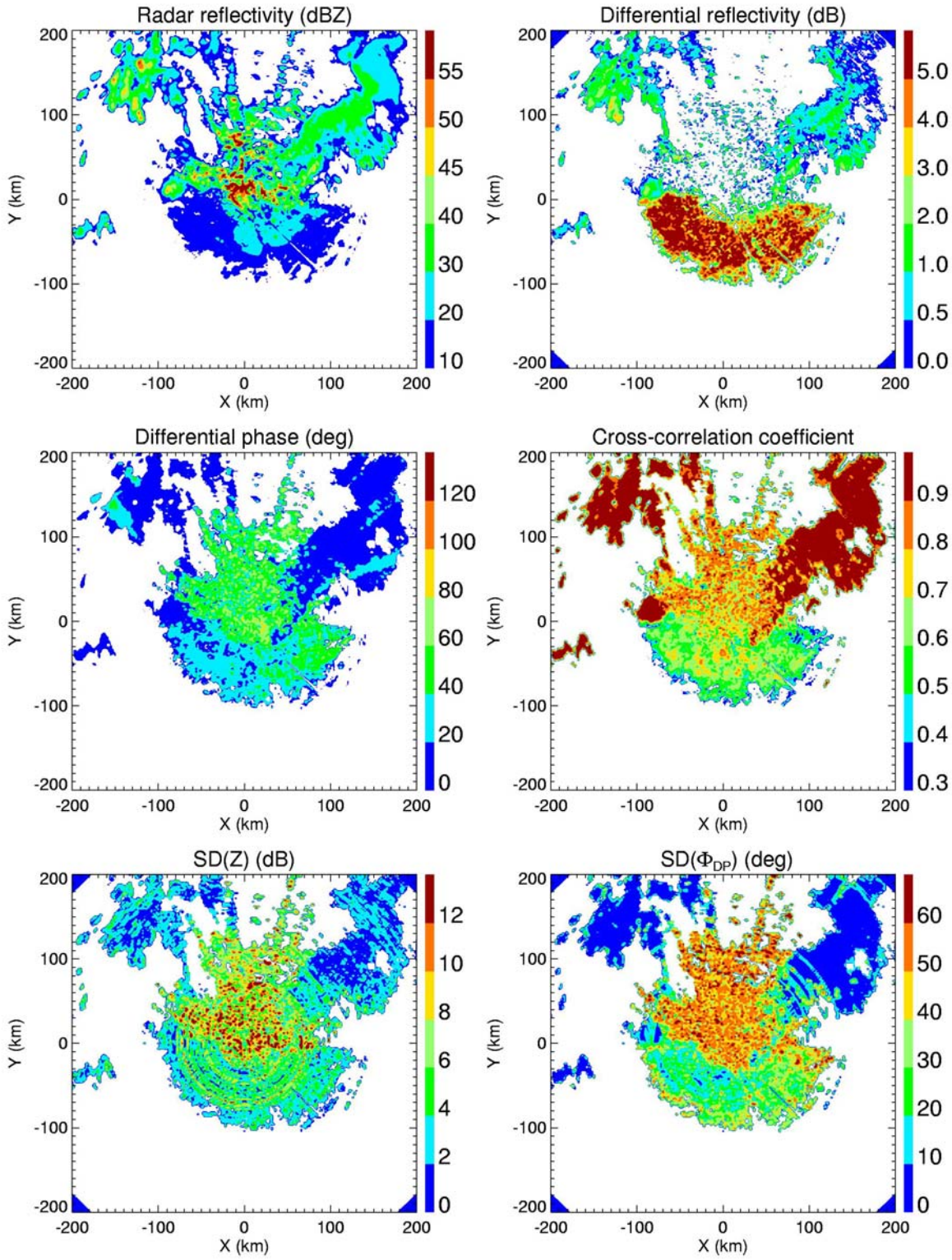

Fig. 8. Composite plot of Z, Z_{DR}, ρ_{hv}, Φ_{DP}, SD(Z), and SD(Φ_{DP}) at El = 0.5º on 13 August 2002, 1024 Z.

for the case of 13 August 2002 when all three sources of radar echo produced significant radar returns. Differential phase Φ_{DP} is displayed in addition to the five radar variables mentioned above. We plan to add Φ_{DP} to the classification scheme in the near future. Differential phase promises to be a very valuable recognition variable provided that (a) the forward and backward propagation components are separated in Φ_{DP} and (b) the differential phase is measured unambiguously between 0º and 360º.

The latter requires some explanation. An intrinsic differential phase of the radar signal due to ground clutter and AP is almost randomly distributed within the interval where the phase is measured (0º – 180º in the RVP7 processor). After radial averaging over 9 successive gates is made, the originally random Φ_{DP} tends to bunch around the middle of the phase interval, i.e., 90º (Fig. 10). Unfortunately, the radar signals backscattered from birds have almost the same differential phase (within 70 - 100º). If differential phase is measured in the 0º - 360º interval, then the predominant Φ_{DP} for ground clutter / AP is about 180º and better separation between ground clutter and birds would be achieved.

Examples of classification for the cases of 24 August 2002 and 1 May 2003 are presented in Fig. 9 and 10. In the first case, all three types of radar echoes are mixed together and the radar reflectivity image gives no clue for identification. The classification algorithm identifies extended regions of AP embedded in precipitation. Animation of the classification fields shows high degree of spatial / temporal "coherency" of these fields and gives us more confidence in the performance of the classification scheme. It is interesting to note a difference between regions likely associated with insects (south of the radar) and birds (x = 100, 200 km, y = -150, -30 km) in the SE sector of the image. "Birds" have lower Z_{DR} and higher Φ_{DP} (not shown) than "insects". Also, the "bird" signatures are observed at larger distances and higher altitudes (about 3 km) which are quite unlikely for insect-related echoes. Mean value of Φ_{DP} for "insects" is about 40º which is substantially lower than the one for "birds".

Fig. 10 illustrates the case with extremely strong AP echo in the SW sector. This echo persisted for about 3 hours and was observed also at the elevation angle of 1.5º, although with lesser spatial extension. No rain was recorded by the Oklahoma Mesonet and ARS Micronet gages in this area. Again, radar reflectivity field gives an impression of strong convective precipitation in the SW sector. Moreover, the presence of AP at higher elevation might confuse traditional AP mitigation schemes based on the Z texture and vertical continuity of the radar echo. The fuzzy logic classification algorithm unambiguously identifies the source of this echo as AP. Less than 1% of radar pixels in this area were wrongly classified as "precipitation" during all three hours of observation of this extreme AP event. At the same time, thin line of rain in the NE sector was correctly identified as precipitation.

As mentioned in section 3, the quality of classification deteriorates with decreasing signal-to-noise ratio (SNR). In all figures, results of classification are displayed for SNR > 5 dB. The use of differential reflectivity (not biased by noise) in the classification algorithm (together with existing radar variables) will hopefully allow us to lower the SNR threshold for reliable classification.

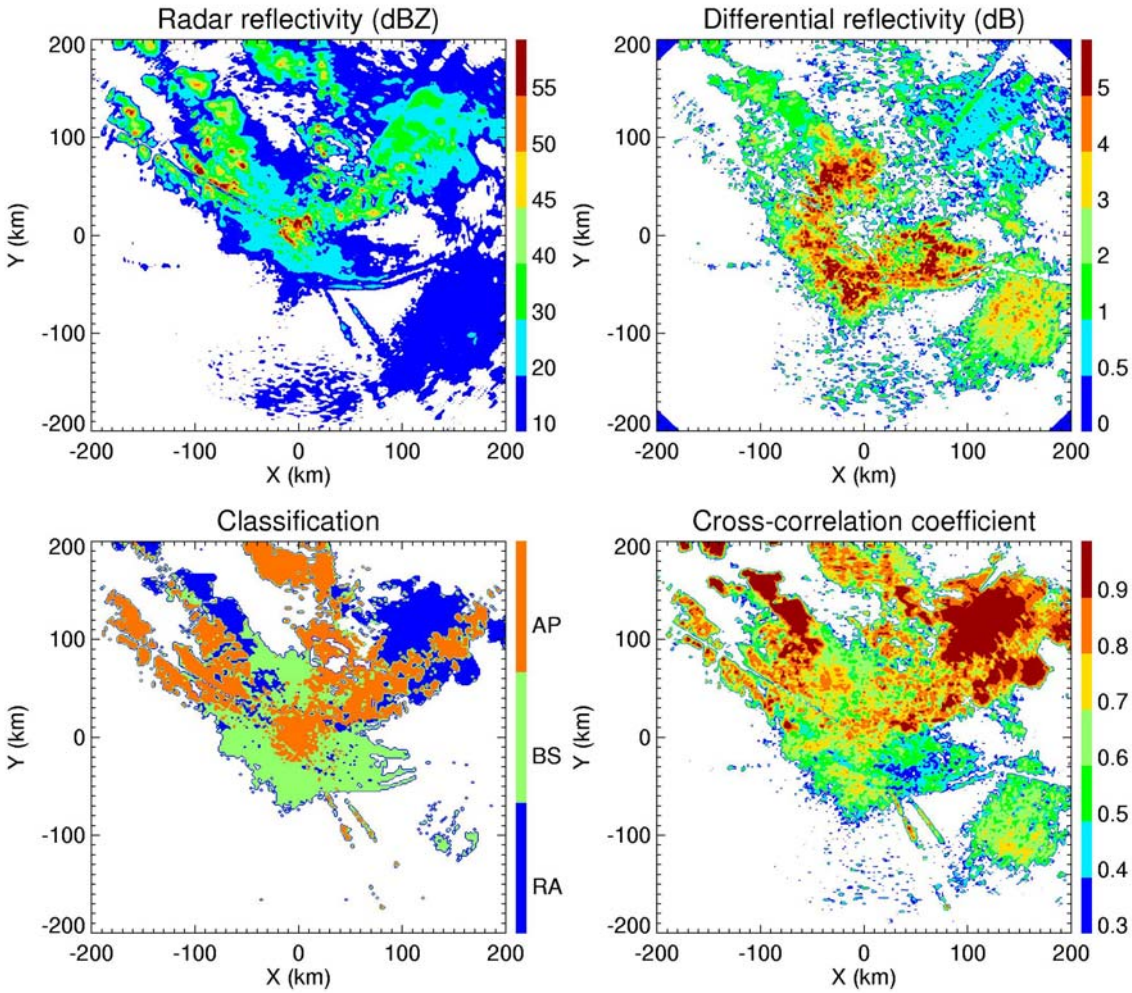

Fig.9. Composite plot of Z, Z_{DR}, ρ_{hv}, and results of classification at El = 0.5º on 24 August 2002, 0734 Z.

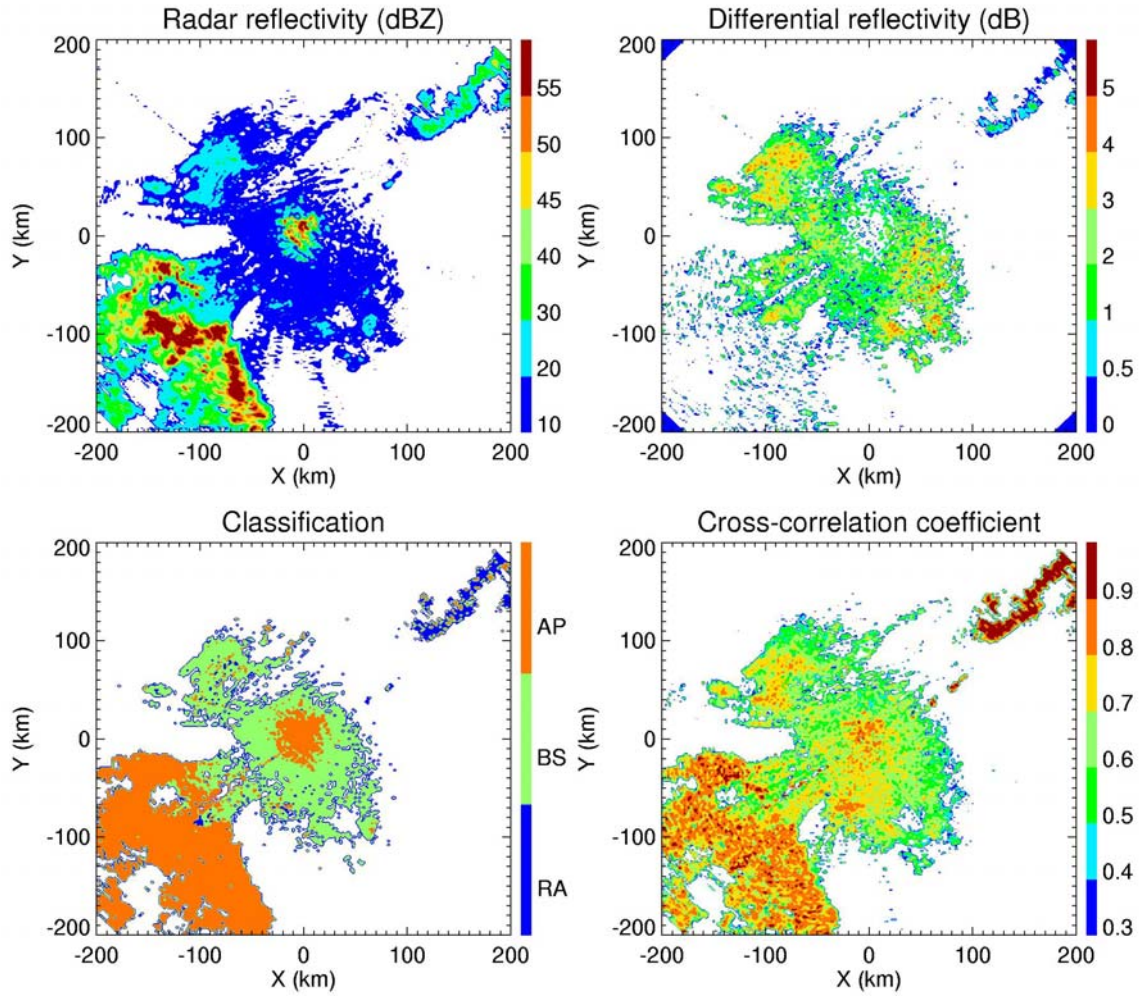

Fig. 10. Composite plot of Z, Z_{DR}, ρ_{hv}, and results of classification at El = 0.5º on 1 May 2003, 1107 Z.

References

Bringi, V,N., V. Chandrasekar, N. Balakrishnan, and D. Zrnic, 1990: An examination of propagation effects on radar measurements at microwave frequencies. J. Atmos. Oceanic Technol., 7, 829 – 840.

Goddard, J., J. Tan, and M. Thurai, 1994: Technique for calibration of meteorological radars using differential phase. *Electronic Letters*, **30**, 166 – 167.

Gorgucci, E., G. Scarchilli, and V. Chandrasekar, 1999: A procedure to calibrate multiparameter weather radar using properties of the rain medium, *IEEE Trans. Geosci. Remote Sensing*, **37**, 269 – 276.

Gourley, J., B. Kaney, and R. Maddox, 2003: Evaluating the calibrations of radars: a software approach. Preprints, *31st International Conference on Radar Meteorology,* Seattle, 459 – 462.

Kessinger, C., S. Ellis, and J. Van Andel, 2001: NEXRAD data quality: the AP clutter mitigation scheme. Preprints, *30th International Conference on Radar Meteorology,* Munich, Germany, 707 - 709

Liu, H. and V. Chandrasekar, 2000: Classification of hydrometeors based on polarimetric radar measurements: development of a fuzzy logic and neuro-fuzzy systems, and in situ verification, *J. Atmos. Oceanic Technol*., **17**, 140-164.

Melnikov, V., D. Zrnic, , R. Doviak, and J. Carter, 2003: Calibration and performance analysis of NSSL's polarimetric WSR-88D. NSSL's report, 15 May, 77 pp.

Miller, D. and K. Scharfenberg, 2003: The use of polarimetric radar data in the winter weather warning decision making process: a case study. Preprints, *31st International Conference on Radar Meteorology,* Seattle, 976 – 979.

Moszkowicz, S., G. Ciach, and W. Krajewski, 1994: Statistical detection of anomalous propagation in radar reflectivity patterns. *J. Atmos. Oceanic Technol*., **11**, 1026 – 1034.

Ryzhkov, A., and D. Zrnic, 1995: Precipitation and attenuation measurements at a 10 cm wavelength. *Journal of Applied Meteorology,* **34**, 2121-2134

Ryzhkov, A., and D. Zrnic, 1998: Discrimination between rain and snow with a polarimetric radar, *J. Appl. Meteor*., **37**, 1228-1240.

Ryzhkov, A., T. Schuur, D. Zrnic, 2002: Testing a polarimetric rainfall algorithm and comparison with a dense network of rain gauges. Submitted to the special issue of *Hydrological Resources* on Hydrological Applications of Weather Radar

Ryzhkov, A.., S. Giangrande, D. Zrnic, 2002: Using multiparameter data to calibrate polarimetric weather radars in the presence of a partial beam blockage. Proc. IGARSS 2002, Toronto, Canada, 2820 – 2822.

Ryzhkov, A. and D. Zrnic, 2003: Discrimination between rain and snow with a polarimetric NEXRAD radar. Preprints, *31st International Conference on Radar Meteorology,* Seattle, 635 - 638.

Scharfenberg, K., and E. Maxwell, 2003: Operational use of a hydrometeor classification algorithm to detect the snow melting level. Preprints, *31st International Conference on Radar Meteorology,* Seattle, 639 – 641.

Steiner, M., and J. Smith, 2002: Use of the three-dimensional reflectivity structure for automated detection and removal of nonprecipitating echoes in radar data. *J. Atmos. Oceanic Technol*., **19,** 673 – 686.

Straka, J., D. Zrnic, and A. Ryzhkov, 2000: Bulk hydrometeor classification and quantification using multiparameter radar data. Synthesis of relations. *Journal of Applied Meteorology,* **39**, 1341 - 1372.

Vivekanandan, J., D. Zrnic, S. Ellis, D.Oye, A. Ryzhkov, J. Straka, 1999: Cloud microphysics retrieval using S-band dual-polarization radar measurements. *Bulletin of the American Meteorological Society,* **80**, 381-388.

Zrnic, D., and A. Ryzhkov, 1998: Observations of insects and birds with a polarimetric radar. IEEE Transactions on Geoscience and Remote Sensing, **36**, 661-668.

Zrnic, D., and A. Ryzhkov, 1999 Polarimetry for weather surveillance radars. *Bulletin of the American Meteorological Society,* **80**, 389 - 406.

Zrnic, D.S., A.V. Ryzhkov, J. Straka, Y. Liu, and J. Vivekanandan, 2001: Testing a procedure for automatic classification hydrometeor types. *Journal of Atmospheric and Oceanic Technology,* **18**, 892 - 913.

.

Appendix B

DISCRIMINATION BETWEEN WEATHER AND SEA CLUTTER USING DOPPLER AND DUAL-POLARIZATION WEATHER RADARS

ABSTRACT

The results of automatic discrimination between weather and sea clutter using S-band dual-polarization Doppler weather radar are presented. The data were collected with the NCAR SPOL radar located in the Pacific shoreline near Seattle, USA. The multiparameter dataset includes backscattered power P (or radar reflectivity Z), Doppler velocity V, spectrum width σ_v, differential reflectivity Z_{DR} (polarization ratio), differential phase Φ_{DP}, linear depolarization ratio LDR, and cross-correlation coefficient ρ_{hv}. Two versions of classification algorithm based on fuzzy logic are explored. One of them utilizes only Doppler radar variables (P and V), whereas the other makes use of both Doppler and polarimetric measurands.

INTRODUCTION

Algorithms for automatic classification of different meteorological and non-meteorological scatterers based on the use of multiparameter data from Doppler polarimetric weather radars have been developed during recent years. These classification schemes utilize ideas of fuzzy logic and prove to be very efficient for hail detection, rain/snow discrimination, identification of ground clutter (including anomalous propagation), birds, and insects [1]. In this study, we apply this methodology to distinguish between sea clutter, precipitation, and marine boundary layer clouds observed with coastal or shipborne S-band radars.

We have examined Doppler polarimetric radar data obtained from the IMPROVE I Field Experiment: Offshore Frontal Precipitation Study conducted by the University of Washington west of the Seattle, WA, area during the period 4 January – 14 February 2001. The data were collected with the NCAR SPOL 10-cm dual-polarization radar located on the Pacific shoreline at the height of 10m above sea level. The multiparameter dataset includes backscattered power P (or radar reflectivity Z), Doppler velocity V, spectrum width σ_v, differential reflectivity Z_{DR}, differential phase Φ_{DP}, linear depolarization ratio LDR, and cross-correlation coefficient ρ_{hv}.

NCAR SPOL is a very sensitive radar capable detecting Z = -15 dBZ at ranges up to 50 km [2]. The radar has a pencil beam of 0.93º. Raw data are sampled every 0.15 km along a range up to 180 km with an azimuthal resolution of 1º. Five days of observations have been examined so far. The multiparameter data from three elevation tilts: 0.0º, 0.5º, and 1.5º, have been thoroughly analyzed with the major focus on the PPIs at the lowest tilt where the problem of discrimination between weather and sea clutter is the most challenging.

OBSERVATIONS

Four types of radar echo in the sea sector of PPI are easily distinguished. The first of them is "normal" sea clutter with a range extension determined by the height and strength of evaporation duct [3]. The second is "anomalous" sea clutter likely caused by multipath propagation attributed either to reflections from elevated layers or to strong local non-uniformities of the evaporation duct. The third is the weather echo associated with the marine boundary layer stratiform clouds (MBLSC) that exist almost all the time in the US Pacific coast area and cover about 25% of the World Ocean. These are shallow clouds consisting of cloud-size or drizzle-size droplets. The height of the cloud top is usually between 0.5 and 1.5 km, and radar reflectivity Z is usually less than –5 to 0 dBZ. Most often these clouds do not produce precipitation, or produce very light drizzle-type rain near sea surface. These clouds are important objects of climatological studies because of their omnipresence and strong effect on radiative transfer. The fourth type of radar echo is caused by precipitating clouds that are most often associated with atmospheric fronts.

Figure 1 illustrates a case where at least three types of echo coexist: (1) "normal" sea clutter, (2) MBLSC, and (3) convective precipitation. The PPI fields of returned power and mean Doppler velocity at the 0.0º elevation angle are displayed in Fig. 1a,b. The radar is located at the point (0,0). Simple visual analysis of the P and V images points to convective precipitation as the most likely origin of isolated echoes that are immersed in a uniform background of extended echoes that can be attributed either to weather or sea scatterers. Only detailed examination of multiparameter data provides a clue about the possible origin of the extended radar echo. Example of such data along the azimuthal

Appendix B

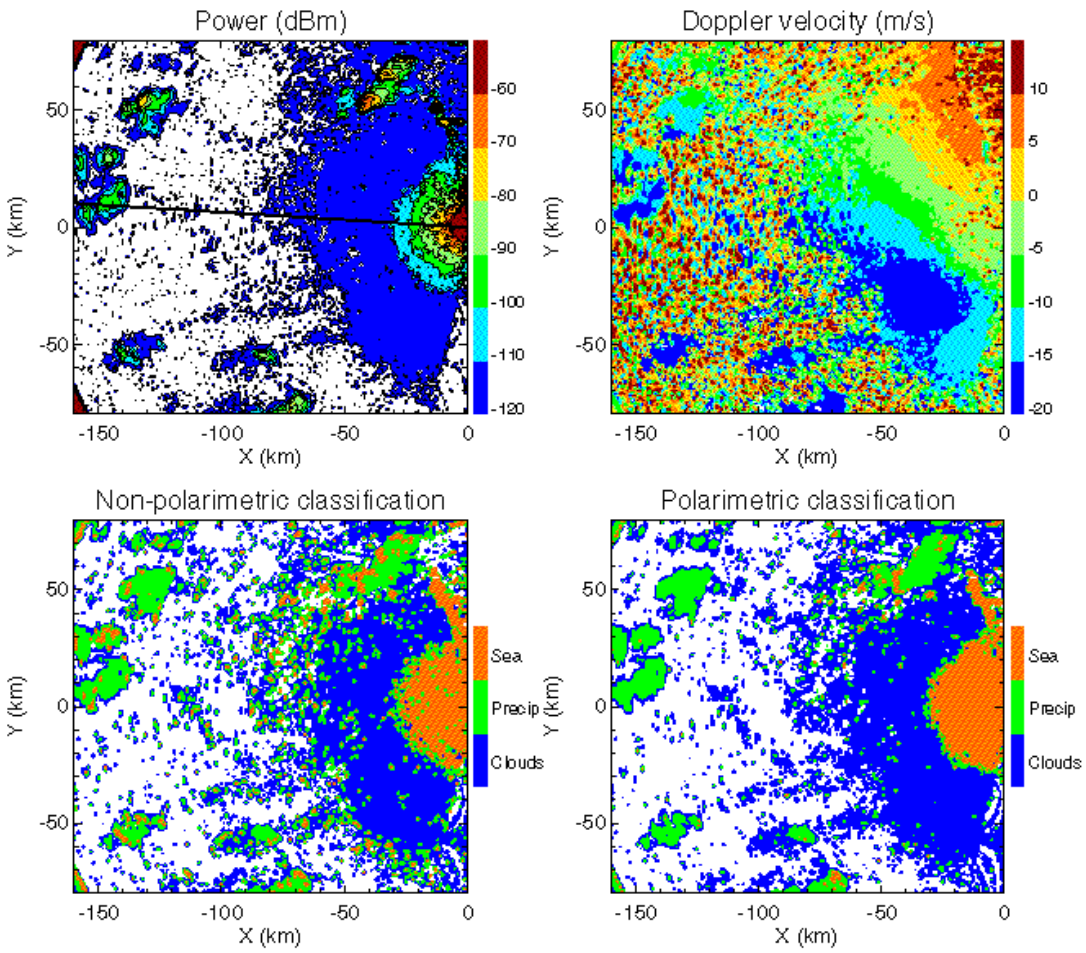

Fig. 1 Combined plot of the fields of returned power *P*, mean Doppler velocity *V*, and results of non-polarimetric and polarimetric classification for data at 0.0º elevation on 2 February 2002 (16:10 UTC). The NCAR SPOL radar is located at (0,0). Solid line corresponds to the direction for which raw multiparameter data are displayed in Fig. 2.

direction 273.7º (depicted as a solid line in Fig. 2a) is shown in Fig. 2. There are three range intervals that are characterized by distinct Doppler and polarimetric signatures. The echo from convective precipitation in the 140-160 km range is recognized by low *LDR*, high ρ_{hv}, large negative values of *V*, and very small spatial variations of Z_{DR} and Φ_{DP}. The high reflectivity region close to the radar (0 – 30 km) has much higher *LDR*, lower ρ_{hv}, smaller values of *V*, and large spatial variations of Z_{DR} and Φ_{DP} that are likely associated with echoes from the sea surface. The low reflectivity zone between 30 and 60 km has properties that are somewhere in between convective rain and sea clutter. These echoes are likely to be from shallow marine boundary layer stratiform clouds (MBLSC). In this particular case, the echoes are confined within the 0 – 500 m height interval. Because the echoes from these clouds are relatively weak and signal-to-noise ratio (SNR) is low, such polarimetric variables as Z_{DR}, *LDR*, and ρ_{hv} are significantly biased by noise. Therefore, the contrast between sea clutter and MBLSC is not as clear as between sea clutter and precipitation from convective clouds. Measurements of differential phase and Doppler velocity are not affected by noise (at least for SNR > -5 dB) and are particularly useful for distinguishing MBLSC from the sea clutter. Differential phase provides amazingly sharp delineation between sea and weather echoes at the distance of 30 km (Fig. 2). The sea – weather transition is also marked by a pronounced change in the magnitude of Doppler velocity. Our analysis of the Doppler

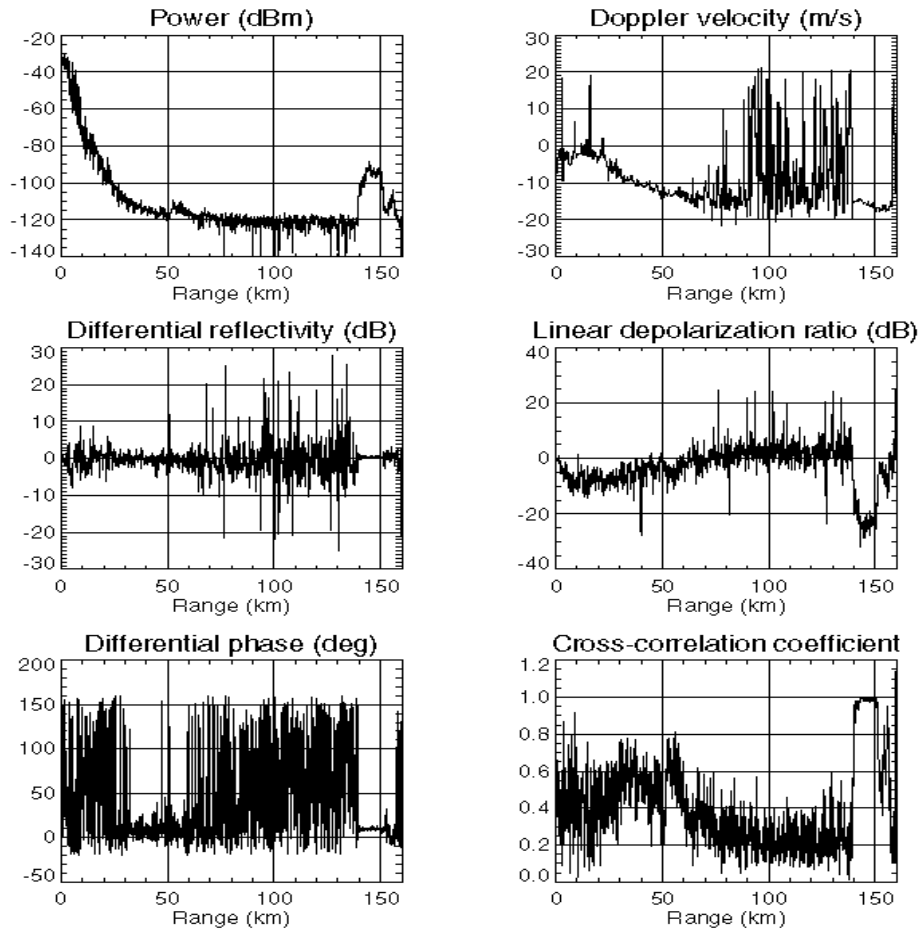

Fig. 2 Radial dependencies of P, V, Z_{DR}, LDR, Φ_{DP}, and ρ_{hv} at the azimuthal direction shown in Fig. 1a.

velocity data for all 5 days of observations shows that the magnitude of V for sea echoes is usually less than 5 m s^{-1}, whereas any Doppler velocities within the unambiguous range ±22 m s^{-1} are possible for meteorological echoes.

FUZZY LOGIC CLASSIFICATION

Fuzzy logic classification method requires knowledge of membership functions for different variables and classes. In order to determine membership functions, we analyzed scattergrams of measured radar variables versus mean power of returned signal (or signal-to-noise ratio) separately for weather and sea clutter. We examined such scattergrams for different days of observations and found that they do not differ much from case to case. In Fig.3, some of these scatterplots for the 2 February 2001case are represented. Black and grey dots correspond to sea clutter and weather clutter respectively. In addition to the ρ_{hv} – SNR, LDR – SNR, and Z_{DR} –SNR scattergrams, we display the $SD(P)$ – SNR scattergram, where $SD(P)$ is the standard deviation of P that characterizes the texture of the P field.

To obtain $SD(P)$, we average raw P data (sampled every 0.15 km) along the radial using 1-km-width running average window and subtract the smoothed values of P from their original raw values. A similar procedure was used to estimate $SD(\Phi_{DP})$ that characterizes the texture of the Φ_{DP} field.

It is evident from Fig. 3, that despite overlapping for SNR < 10 dB, sea and weather clutter are very well separated in terms of ρ_{hv}, LDR, and $SD(P)$. The separation is even better for $SD(\Phi_{DP})$ (Fig. 1). As in the case of Doppler velocity, the two classes of echo are well overlapped in the Z_{DR} - SNR plane although the corresponding scattergrams have very different widths. Noticeably larger values of $SD(P)$ for sea clutter reflect the fundamental fact that an amplitude distribution of the echoes from the sea surface is much wider than the one from hydrometeors.

We consider two versions of classification scheme: polarimetric and non-polarimetric ones. The polarimetric classification algorithm utilizes $SD(\Phi_{DP})$, ρ_{hv}, LDR, Z_{DR}, V, and $SD(P)$, whereas only $SD(P)$ and V are used in the non-polarimetric version. Once discrimination between sea and weather clutter is made, a simple threshold of Z = -5 dBZ is

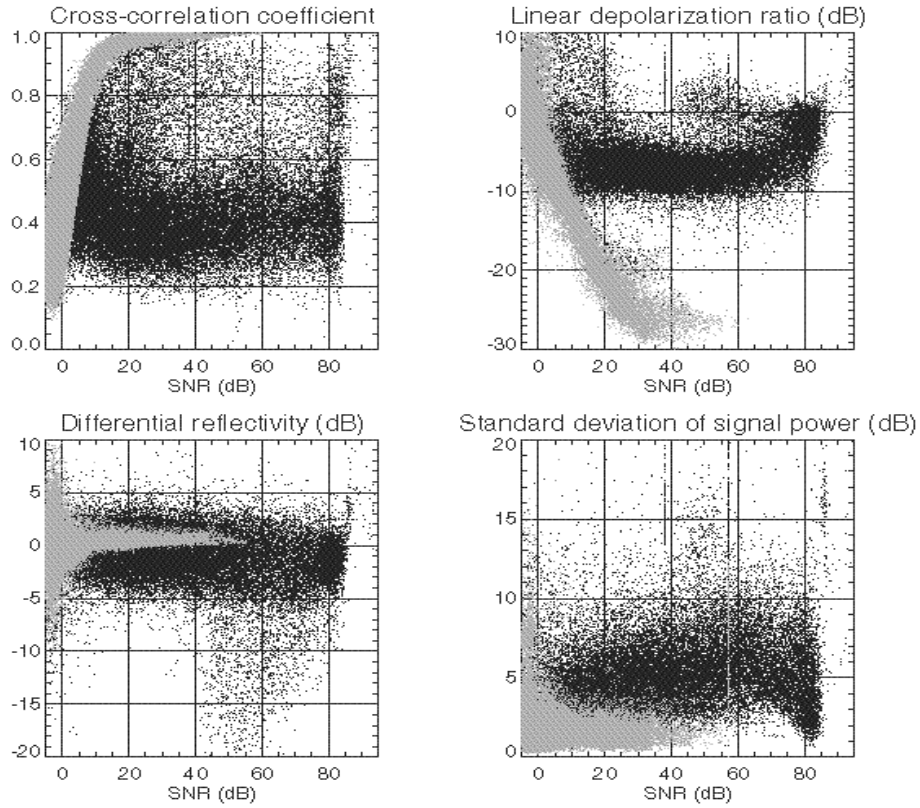

Fig. 3 Scattergrams of ρ_{hv}, *LDR*, Z_{DR}, and *SD(P)* versus SNR for (a) sea echoes (black dots) and (b) weather echoes (grey dots). The data are taken at the elevation angle of 0.0º on 2 February 2001.

used to distinguish between MBLSC (denoted as "clouds" in Fig. 1c,d) and convective precipitation (marked as "precip"). Results of automatic classification are displayed in Fig. 1 c,d. As expected, polarimetrric algorithm exhibits superior performance. Although non-polarimetric version produces more speckles, it delineates quite well sea clutter and both types of weather echoes.

POSSIBLE PRACTICAL APPLICATIONS

The need for partitioning the near-surface radar echo leads to very important practical implications regarding the technique for estimating evaporation duct heights from sea echoes [3]. Discrimination between sea and weather echoes has to be performed prior to application of the mentioned technique.

There are many National Weather Service WSR-88D S-band radars operating in the coastal regions of US. The standard technique for ground clutter rejection based on filtering around zero Doppler frequency doesn't work for sea clutter because the latter has essentially non-zero mean Doppler velocity. This study provides an alternate approach for sea clutter detection and rejection.

REFERENCES

[1] J. Vivekanandan, D. Zrnic, S. Ellis, R. Oye, A. Ryzhkov, and J. Straka, "Cloud microphysics retrieval using S-band dual-polarization radar measurements", *Bull. Amer. Meteor. Soc*., vol. 80, pp. 381-388, March 1999

[2] R.J. Keeler, J. Lutz, and J. Vivekanandan, "S-Pol: NCAR's polarimetric Doppler research radar", *IGARSS-2000*, Honolulu, 2000.

[3] T. Rogers, C. Hattan, and J. Stapleton, "Estimating evaporation duct heights from radar sea echo", *Radio Science*, vol. 35, pp. 955-966, July 2000.

Appendix C

WHITENING IN RANGE TO IMPROVE WEATHER RADAR SPECTRAL MOMENT ESTIMATES

PART II: EXPERIMENTAL EVALUATION

Igor R. Ivić[1,2], Dušan S. Zrnić[2], and Sebastián M. Torres[1,2]

1) Cooperative Institute for Mesoscale Meteorological Studies, University of Oklahoma

2) National Severe Storms Laboratory, Norman, Oklahoma

August 22, 2002

Corresponding Author:

Igor Ivić

National Severe Storms Laboratory

1313 Halley Circle

Norman, OK 73069

tel. (405) 366-0574

fax. (405) 579-0850

e-mail: igor.ivic@nssl.noaa.gov

submitted to the *Journal of Atmospheric and Oceanic Technology*

ABSTRACT

Demonstration of a method for improved Doppler spectral-moment estimation is made on the NOAA's research and development WSR-88D in Norman, Oklahoma. Time series data have been recorded using a commercial processor and digital receiver whereby the sampling frequency is several times larger than the reciprocal of the transmitted pulse width. The in-phase and quadrature-phase components of oversampled weather signals are used to estimate the first three spectral moments by suitably combining weighted averages in range with usual processing at fixed range locations. The weights are chosen in such a manner that the resulting signals become uncorrelated. Consequently, the variance of estimates decreases significantly as is verified by this experiment.

1. Introduction

There are compelling scientific and practical reasons to rapidly acquire volumetric radar data. For example, observations at minute intervals are required to understand the details of vortex formation and demise near the ground. Even faster rates of volumetric data are needed to determine the presence of transverse winds (Shapiro et al. 2001). Fast update rates would also yield more timely warnings of impending severe weather phenomena such as tornadoes and strong winds. Even rainfall measurement would be better if radar data were available at shorter intervals than the current 6 minutes (Fabry et al. 1994).

Surveillance weather radars have a mechanical control of beam position and dwell

a relatively long time (~ 50 ms) to obtain sufficient number of independent echo samples for accurate estimates of Doppler spectral moments (Doviak and Zrnić 1993). Thus, the volume update times are dictated by two limitations: 1) the inertia of the mechanically steered antenna, and 2) the correlation time of weather signals. Phased array radars promise to increase the speed of volume coverage. Reports about simultaneous use of phased array radar for tactical application and weather observation indicate that a radial of data can be obtained from only two transmitted pulses as opposed to over 40 on the WSR-88D (Owen et al. 1998). Closer examination of this success reveals that rapid beam swinging is not the main contributor to such fast updates; rather, it is the pulse compression. Pulse compression requires wide transmitter bandwidth that is not available to the operational weather radar community. Hence the dilemma of how to increase the data acquisition speed and fully utilize the rapid beam steering afforded on phased array radars. An improvement by a factor of two is possible by "beam multiplexing", where the data from different directions are collected in a repetitive time-shared pattern (Doviak et al. 2001). This, however, falls short of the desired capability.

A very different scheme to process weather radar data has recently been proposed. Koivunen and Kostinski (1999) suggest to decorrelate (whiten) the time series of weather echoes and then process these to obtain better estimates of powers. To achieve this type of whitening, prior knowledge of the weather signal correlation coefficient is required (Schultz and Kostinski 1997). Consequently, the spectrum should be known or rather tight constraints on the range of its values must be imposed, neither of which is practical. These issues are discussed in the cited and other references (Kostinski and Koivunen 2000).

Torres and Zrnić (2003) capitalize on the known behavior of weather signals in range and present a viable method for reducing variance of spectral moment estimates. They propose to sample the signal in range at time intervals L times smaller than the pulse duration. Then, by a linear transformation, whiten the L samples, compute various autocovariances (or Doppler spectra) of the samples, and combine these to obtain spectral moment estimates. The underpinning assumption is that the oversampled weather signals are wide-sense stationary over the pulse depth. This assumption is implicit in standard processing of weather signals whereby a matched filter precedes spectral processing. An in-depth analysis of the scheme is documented elsewhere (part I of this paper, also Torres 2001), whereas herein we present a sample of a test on the NOAA research and development WSR-88D radar to demonstrate its practicality.

2. Theoretical Background

If the returned echoes are sampled more frequently in range than once per pulse duration, it is possible to reduce the variances of estimates. Averaging of L oversampled estimates reduces the variance by a factor L_I known as the effective number of independent samples, which is computed from

$$L_I^{-1} = \sum_{l=-(L-1)}^{L-1} \frac{L-|l|}{L^2} |\rho_S(l)|, \tag{1}$$

where $\rho_S(l)$ is the correlation coefficient of the variable averaged to obtain the estimates (Doviak and Zrnić 1993). Note that the maximum possible reduction in variance through averaging is by L, which is achieved only if signals are uncorrelated. Thus, if samples are correlated, simple averaging does not lead to an optimum variance reduction. As an

example, consider a rectangular transmitted pulse and a receiver with infinite bandwidth for which the magnitude of the correlation coefficient of oversampled complex signals in range is (Doviak and Zrnić 1993)

$$\rho(l) = \begin{cases} 1 - |l| / L & |l| < L \\ 0 & otherwise \end{cases}. \tag{2}$$

The correlation coefficient for oversampled powers is $|\rho(l)|^2 = |\rho_S(l)|$. Substituting this $\rho_S(l)$ in (1), one finds that $L_I = 2$ in the limit for very large L. Therefore, a reduction of at most two in variance is possible by directly averaging the oversampled power estimates.

A different scheme to process the samples and achieve a significantly smaller variance of estimates is described in part I of this paper. It entails decorrelating the oversampled signals in range and then processing these in the usual manner. That is, powers of the uncorrelated signals (in range) are averaged to obtain the reflectivity, and estimates of the autocovariance in sample time are averaged to retrieve the mean Doppler velocity and spectrum width.

If the reflectivity is uniform on a distance of two pulse depths, the correlation coefficient of oversampled signals along range time is a function of the pulse shape and the receiver impulse response (Doviak and Zrnić 1993). This range-time correlation coefficient can be measured on data or by passing the (attenuated) transmitted pulse through the receiver and recording the response. It can then be used to whiten the samples as described in the formulation of part I.

It is instructive to compare the variances of estimates obtained by averaging in range autocovariances of oversampled signals with those obtained from averages of whitened signals. If noise effects are not taken into consideration, in the case of a

rectangular pulse, the ratio of the two variances is

$$\frac{\mathrm{var}(E_{correlated})}{\mathrm{var}(E_{whitened})} = \frac{L^2+1}{2L}, \tag{3}$$

where $E_{correlated}$ stands for the estimate obtained by averaging L autocovariances from oversampled signals and $E_{whitened}$ is the estimate obtained by averaging L autocovariances from whitened oversampled signals (Torres 2001).

3. Experimental Set Up

For validation of the theoretically-predicted variance reductions we used the Sigmet RVP7 digital processor passively coupled to the research and development WSR-88D weather radar in Norman, Oklahoma. The RVP7 incorporates a digital receiver at intermediate frequency (IF) and has an inherent capability to sample signals at higher rate than the reciprocal of the pulse width. In addition, it can record a limited amount of time series data (I and Q). An antialias filter centered on the intermediate frequency (f_{if} ~ 57 MHz) and with a bandwidth of about 8 MHz precedes the digital receiver. The IF signal was tapped ahead of the existing matched filter at a point where the receiver bandwidth was about 15 MHz and was passed through the antialias filter. Hence, the frequency response at the input to the digital receiver is primarily shaped by the antialias filter. The WSR-88D can easily switch between two pulse lengths: short equal to 1.57 μs (250 m range resolution) and long equal to 4.71 μs (750 m range resolution). The scheme was tested on both of these.

Constraints on the RVP7 around which we designed the experiment are as

follows. The sampling frequency f_s for the intermediate frequency (f_{if}) signal is $(5/8)f_{if}$. After sampling, a digital down-conversion is combined with a finite impulse response (FIR) filter (RVP7 User's Manual). The filter has a variable number of taps W, and the spacing of output digital samples is D/f_s which is also variable (Fig. 1). The weights on the FIR filter can be programmed for a desired frequency response; we chose a uniform set. The digital sinusoid for down-conversion starts with the same phase every D/f_s seconds and therefore has a variable phase relation (from sample to sample) with respect to the IF signal unless D is a multiple of five. It is not possible to set D to an odd number, and the minimum allowable even multiple of five for D is 20. Phase discontinuities among output range samples render the whitening algorithm ineffective, thus we chose D = 20 (corresponding to gate spacing of 83.3 m) and the same value was used for the number of taps W. With this D, the number of samples L is 3 within the short pulse and 9 within the long pulse.

As mentioned before, the processor can record time series data (I and Q) from a limited number of range gates. In the experiment we recorded data from 101 consecutive range locations spaced 83.3 m apart; each set of 101 samples from one transmitted pulse form a radial, and 128 radials constitute one record (due to the constraints imposed by RVP7 there is a gap of about one second between records).

4. Measurements and Analysis of Results

Several sets of data from weather events and ground clutter were recorded in both the short (regular) and the long pulse mode. The whitening-transformation-based (WTB) estimates were obtained from these data sets.

Appendix C

a. Correlation Coefficient

Implementation of the whitening transformation requires knowledge of the autocorrelation function of oversampled signals along range. One robust way to compute the set of autocorrelation coefficients is from the oversampled weather data itself. The magnitudes and phases of the correlations obtained in this manner are given in Figs. 2 and 3 for both pulse lengths. These curves are averages of sample autocorrelation coefficients in both range and time. The number of range locations for averaging was $\lfloor 101/L \rfloor$; the number of averages in time was 1280 (i.e., 1280 samples were averaged at each lag). At every range location the signal-to-noise ratio (SNR) was larger than 35 dB. For both pulse lengths the magnitude of the autocorrelation (Figs. 2*a* and 3*a*) has a fairly triangular shape, which is expected from a rectangular pulse. The deviation from straight lines is likely due to the non-vertical leading/trailing edges of the pulse and the effects of the overall radar system filter. The correlation coefficient of samples was also computed after the application of the whitening transformation (Eq. 3, part I) . The result is a noise-like peak at lag zero and insignificant values at other lags (Figs. 2*b* and 3*b*).

We draw attention to the phases of the correlation coefficients. Note that the phase is non-trivial for the non-zero values of the magnitude. This phase shift is caused by the amplitude modulation to phase modulation (AM to PM) conversion whereby the voltage variations of the transmitted pulse envelope (primarily rise and decay and secondarily small ripples) are converted into phase variations of the RF carrier frequency. This effect is inherent to the klystron amplifier and it was found to be repetitive.

b. Spectral Moments

Mean power, mean Doppler velocity, and Doppler spectrum width were computed using estimators given in part I (equations 14, 16, and 19) in the following three ways:

1) From regularly spaced range locations (at 83.3 m) first by averaging in range the in-phase and quadrature-phase (I, Q) components, and then by processing the autocovariances to produce the moments. The coherent averaging of samples over the pulse duration (3 samples for short pulse and 9 for long pulse) is a digital matched filter which approximates its analog counterpart fairly well. Henceforth, this procedure is called the matched-filter-based (MFB) processing.

2) From averages of autocovariances of oversampled signals. The number of averages in range was 3 for the short pulse and 9 for the long pulse. We call this procedure the oversampling-and-average-based (OAR) processing. It is a straightforward extension of the MFB processing, and about the best one can achieve with correlated oversampled data.

3) From averages of autocovariances of oversampled and whitened data. The same number of averages as in 2) was used, and we call this procedure the whitening-transformation-based (WTB) processing.

Each initial autocovariance estimate (including at lag zero for power) was obtained from 32 contiguous time samples (I and Q components), which corresponded to dwell times of 31.57 ms for the short pulse and 71.68 ms for the long pulse. The pulse repetition frequencies were 1013.51 Hz for the short and 446.43 Hz for the long pulse.

For the real data used in the experiment the true values of estimates are not known

but are required for calculation of variances. Consequently, these "true" values had to be estimated as well. To achieve this, short term (local) estimates of the mean values of autocovariances and corresponding spectral moments were obtained from 10 consecutive records of data. Because we had 100 records, ten variances at each range location obtained from local mean estimates were averaged, and their square roots (standard deviations) are plotted herein for comparisons. Short term averaging was necessary to mitigate the effects of radial changes (in the structure of the spectral moments) due to advection and evolution. Plots of the spectral moments vs. range for records spaced by 20 s indicate progressive systematic changes in details (Figs. 4, 5 and 6, obtained from OAB estimates). The reflectivity features (Fig. 4) have clearly advected towards the radar by about 1 km during the time of 111 s (i.e., 100 records). Similar advection is present in the other two spectral moments. Advection across the beam and evolution are likely the cause of other changes in these features.

There are different ways to deal with the fact that the correlation coefficient is complex (attributed to the phase shift produced by the AM to PM conversion in the klystron amplifier). One is to use it directly in Eq. 4 of Torres and Zrnić (2003). The other is to take out the progressive phase shift within the pulse that the AM to PM conversion causes, and then use the magnitude of the correlation coefficient in the aforementioned equation to decorrelate the samples. We opted for the latter.

We paired the plots of estimated standard deviations with "theoretical" values of standard deviations at each range location and for each procedure. By "theoretical" we mean prediction from analytic formulas and derivations applied thereof. The analytic formulas can be found in Doviak and Zrnić 1993 (equations 6.10, 6.21, and 6.30a) along

with the conditions under which those are valid (equations 6.20a and 6.20b). They contain summations of correlation coefficient at various lags, as well as noise effect terms. The sample-time autocorrelation coefficient was obtained by fitting a Gaussian shape to the autocorrelation estimated from data. Because the accuracy of estimates is inversely proportional to the lag number an adaptive fit was used. It starts from the peak of the correlation estimate (at lag zero) and proceeds to smaller values (larger lag values) dynamically averaging the width of the fit to closely match the observed autocorrelation shape. The process stops when the difference between the fitted and estimated correlation is larger than a threshold of 30 % (Fig. 7). This determined the value of the width which was then used to calculate the autocorrelation at subsequent lags. In all of our examples the signal to noise ratio was larger than 35 dB hence the noise enhancement effects were negligible (Torres and Zrnić 2003). Consequently, the noise was set to zero in theoretical computations. The standard deviation (SD) of power estimates was converted to a dB scale by the equation

$$SD(\hat{P}) = 10\log\left(1 + \frac{\sqrt{\mathrm{var}(\hat{P})}}{P_o}\right), \tag{4}$$

where $\hat{P}$ is the power estimate and P_o is the estimate of the local mean value of power. Figures 8, 9, and 10 illustrate the standard deviations of spectral moments as a function of range for the oversampling factor $L = 3$.

The standard deviation of normalized power estimates obtained from whitened samples is consistently smaller than its counterparts (Fig. 8). All these estimates exhibit a maximum at approximately 79 km and 83.5 km. It is at these range locations that the spectrum width (see Fig. 6) exhibits a local minima. The spectrum width formula

(Doviak and Zrnić 1993) shows that a lower spectrum width corresponds to a higher autocorrelation in sample time. Therefore, the signal autocorrelation along sample time reaches its local maxima at these ranges. Consequently, this decreases the equivalent number of independent samples (L_I) resulting in a higher variance for power estimates. Although whitening has decreased the SD($\hat{P}$) the maximum value of about 1.5 dB is still larger than the 1 dB WSR-88D specification for a 1 km average. If the oversampling factor is increased to 8 (possible but not available on the RVP7 processor) the SD($\hat{P}$) over the 250 m pulse depth would be below the 1 dB specification. Note that theoretical values of SD (Fig. 8b) are in good agreement with the experimental data in Fig. 8a.

The experimentally determined SDs of mean Doppler velocity estimates (Fig. 9a) are in a reasonable agreement with the corresponding theoretical curves given in Fig. 9b. Both experimental (Fig. 10a) and theoretical (Fig. 10b) curves for the Doppler spectrum width show the expected improvements with the OAB, and the WTB techniques. Nonetheless, these are not well matched as there are considerable differences in the values of SDs. This could be attributed to the fact that the theoretical values are based on fitting a Gaussian spectral shape to data which is not always Gaussian, and the spectrum width estimator sensitivity to the spectral shape. In the case of the velocity SD, the two local minima are at approximate ranges (79 km and 83.5 km) where the spectrum width reaches a local minima (Fig. 6) and the SDs of the reflectivity reach a local maxima. This is because the lower spectrum width corresponds to higher autocorrelation in sample-time, which produces smaller variance of velocity estimates (Doviak and Zrnić 1993). As the correlation increases L_I decreases, but the effect in case of velocity estimates is a net decrease in the variance. The SD(v) for both oversampling and averaging and

oversampling and whitening satisfy the WSR-88D requirements (less than 1 m s^{-1}). The same requirement on the SD(F) is fully met only if oversampling and averaging is applied.

Reduction in SDs for L = 9 are presented next (Figs. 11, 12, and 13). Changes due to advection and evolution were comparable to the ones in Figs. 4, 5 and 6 but more pronounced. This is expected, as the time to collect data was 186 seconds (compared to 111 s for L = 3). Data was collected on the same day but from a different location in the storm and there was about 15 minutes of time difference between the two sets of records. The 1 dB error requirement for the reflectivity factor is met only in the case of oversampled and whitened data. In this example, the requirements for the velocity and spectrum width estimates are met with all three techniques. This is no surprise as the reflectivity is most stringent and dictates the dwell time. The improvement in spectral moment estimates due to whitening is more pronounced in the long pulse mode because the oversampling factor (L = 9) is three times larger than in the short pulse mode. Observe that the theoretically obtained SDs are somewhat smaller than the experimental ones. This is likely due to the increased pulse depth (in range) of 750 m. Hence, further departure from the assumption of uniform reflectivity within the pulse, resulting in incomplete whitening (Torres and Zrnić 2003).

Scatter plots (Figs. 14, 15, and 16) of the OAB versus WTB estimates show significantly larger dispersion of results in the case of spectrum width (even though negative values were approximated with the adjacent non-negative estimates). The overplot line is the best straight line fit in the least mean squares sense and is obtained by minimizing the perpendicular offsets. In case of reflectivity and velocity, the fit is well

balanced and shows no bias of the WTB estimates. The spectrum width fit exhibits no consistent bias, but is slightly tilted in the counter-clockwise direction. This effect along with the higher dispersion could be caused by the previously mentioned sensitivity of the spectrum width estimator to the non-Gaussian shape of the weather signal spectra that occurs in nature.

Finally, a comparison of variances of the estimates obtained by the three procedures and for the short pulse (L = 3) is summarized in Table 1. The theoretical values (based on equations 6.10, 6.21, and 6.30a in Doviak and Zrnić 1993) are also included. The variances have been obtained by averaging in both range (over 99 range locations) and time (1280 pulses or radials). Overall, the measured (in odd columns) and theoretical (even columns) ratios of variances agree very well, and the variances from whitened data are smallest.

5. Conclusion

Definite demonstration of a novel procedure to process weather radar signals has been made. It was accomplished on actual time-series data recorded on the NOAA research and development radar while the antenna was stationary. This radar is an augmented WSR-88D. For this paper, the pertinent addition is a commercial processor capable of sampling radar signals several times per pulse duration.

Processing consisted of decorrelating the oversampled signals in range and applying standard procedures to the whitened samples. The standard deviations of whitening based estimates were compared to the ones obtained by regular (matched filter) processing and to the ones from simple averages of autocovariances. Variance reduction

equal to the number of oversampled points was achieved with the novel scheme as predicted by the theory. This verification was done on weather signals with large (> 35 dB) SNR.

The implications of this conceptual proof could be far reaching. Because errors of estimates are inversely proportional to the volume scanning times, it follows that weather phenomena can be surveyed faster, while maintaining the same level of accuracy as present processing methods. Alternatively, variance of estimates can be improved at the current volume scanning times. The method has no requirements for transmitter bandwidth other than the usual ones for pulse Doppler radars, and it allows traditional processing (i.e., matched filter) which is advantageous at low SNRs. Further, the tests demonstrate that the technique is completely compatible with the WSR-88D and thus could be implemented on the US national network of weather radars (Torres and Zrnić 2002).

Acknowledgments

The WSR-88D research radar is maintained by Mike Schmidt and Richard Wahkinney. Dr. Valery Melnikov was instrumental for data collection, recording, and manipulation of the RVP7 processor. The National Weather Service has and continues to provide help in maintaining the radar, and the Radar Operation Center of the NWS was responsible for installing and supporting the RVP7 processor. Dr. Richard Passarelli and Mr. Alan Sigia of Sigmet gave us valuable guidance concerning the intricacies of the RVP7 processor. Funding for this research was provided under NOAA-OU Cooperative Agreement #NA17RJ1227. The Federal Aviation Administration provided support for part of this work through Interagency Agreement DTFA 03-01-X9007.

References

Doviak, R.J., and D.S. Zrnić, 1993: Doppler radar and weather observations, Academic Press, San Diego, p. 562.

Doviak, R.J., D.S. Zrnić, and A. Shapiro, 2001: Phased array weather radar – benefits and challenges, Preprints 30th International Conference on Radar Meteorology, AMS, Munich, 202-204.

Fabry, F., A. Bellon, M.R. Duncan, and G.L. Austin, 1994: High resolution rainfall measurement by radar for very small basins: The sampling problem reexamined. *J. Hydrology,* **161**, 415-428.

Koivunen A.C., and A.B. Kostinski, 1999: The feasibility of data whitening to improve performance of weather radar. *J. Appl. Meteor.,* **38,** 741-749.

Kostinski A.B., and A.C. Koivunen, 2000: On the condition number of Gaussian sample-covariance matrices. . *IEEE Tr. Geoscience and Remote Sensing,* **38,** 329-332.

Owen H., H. Urkowitz, J. Melody, J. Stephans, J. Kanefield, and S. Katz, 1998: Collection and Processing of Environmental Data Using A Tactical Shipboard Radar. Proceedings of the 14th International Conference on Interactive Information and Processing Systems (IIPS) for Meteorology, Oceanography and Hydrology, Phoenix, Az, AMS, 316-120.

Shapiro A., P. Robinson, and J. Wurman, 2001: Single-Doppler velocity retrievals with rapid-scan data. Preprints 30th International Conference on Radar Meteorology, AMS, Munich, 194-196.

Schultz, J.T, and A. B. Kostinski, 1997: Variance bounds on the estimation of reflectivity and polarization parameters in radar meteorology. *IEEE Tr. Geoscience and Remote Sensing,* **35,** 248-255.

SIGMET, 1999: RVP7 Digital receiver and Doppler signal processor user's manual., p 5-4.

Torres, S.M., 2001: Estimation of Doppler and polarimetric variables for weather radar. Ph.D. dissertation, The University of Oklahoma, Norman, OK.

Torres, S., and D.S. Zrnić, 2003: Whitening in range to improve weather radar spectral moment estimates. Part I: Formulation and Simulation. Submitted for publication to the *Journal of Oceanic and Atmospheric Technology.*

Zrnić, D.S., and S.M. Torres 2002: Efficient estimation of spectral moments and the polarimetric variables on weather radars, sonars, sodars, acoustic flow meters, lidars, and similar active remote sensing instruments. US patent 6,448,923 B1.

Appendix C

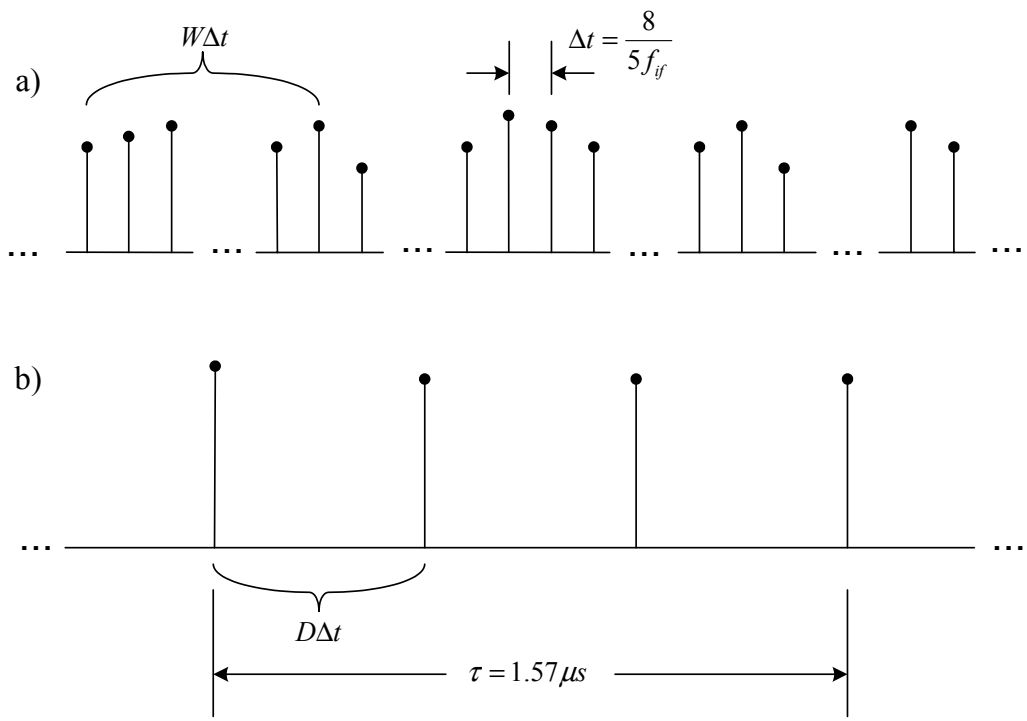

Figure 1. Samples of (*a*) digitized IF signal and (*b*) baseband *I* and *Q* signal for the short pulse in RVP7.

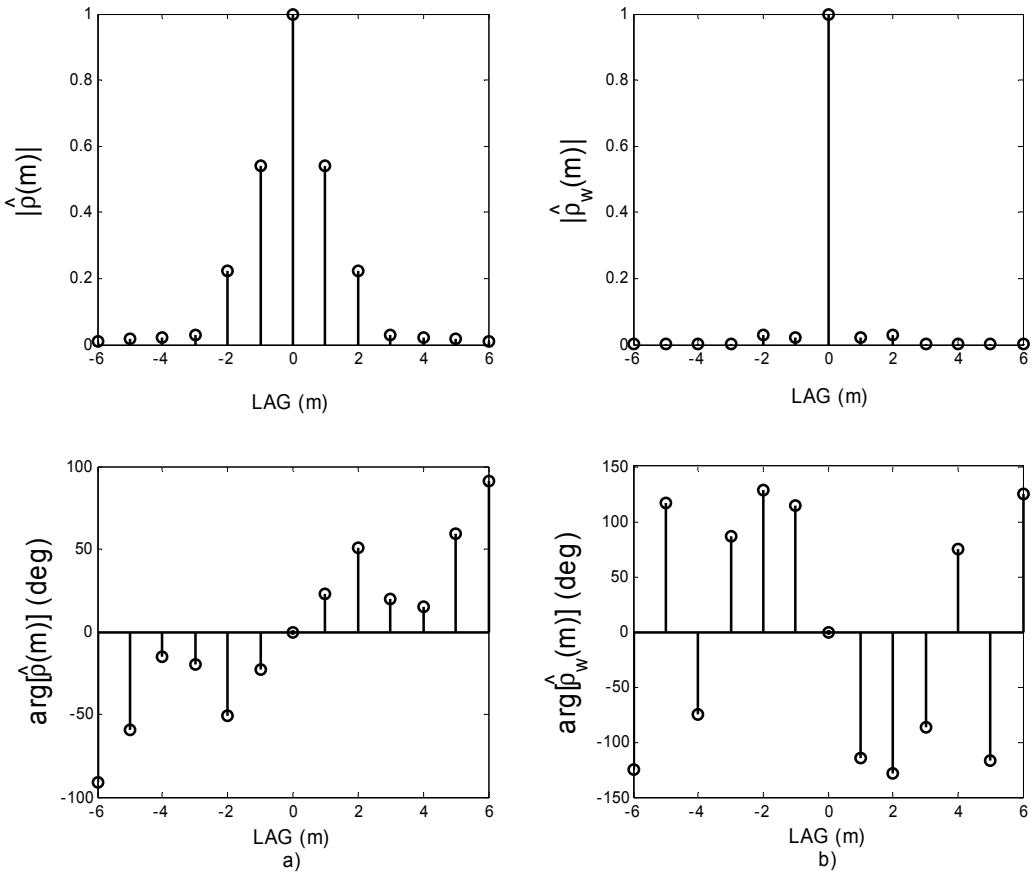

Figure 2. Magnitude and argument of the autocorrelation (*a*) before and (*b*) after whitening for $L = 3$, obtained from time series of weather data. The short pulse was transmitted and one lag corresponds to ~ 0.57 ：s.

Appendix C

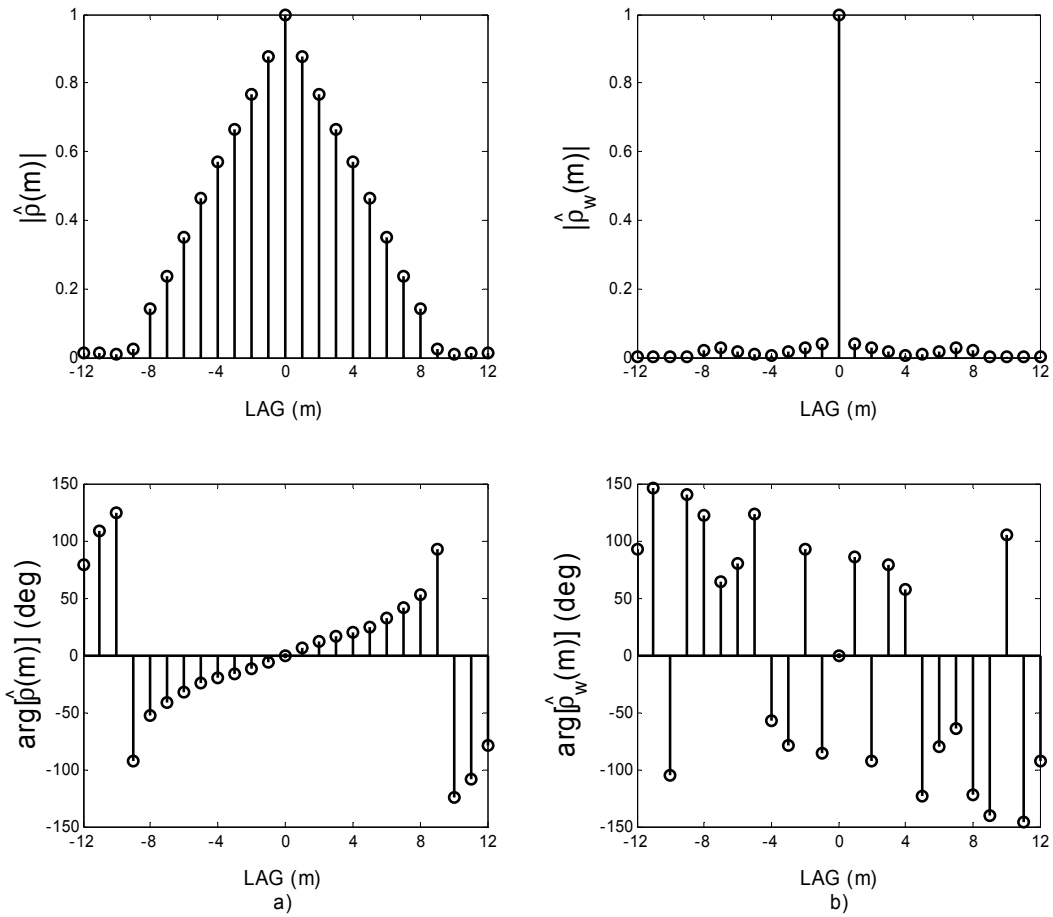

Figure 3. Magnitude and argument of the autocorrelation (*a*) before and (*b*) after whitening for $L = 9$, obtained from time series of weather data. The transmitted pulse was long and one lag corresponds to ~ 0.57 ：s.

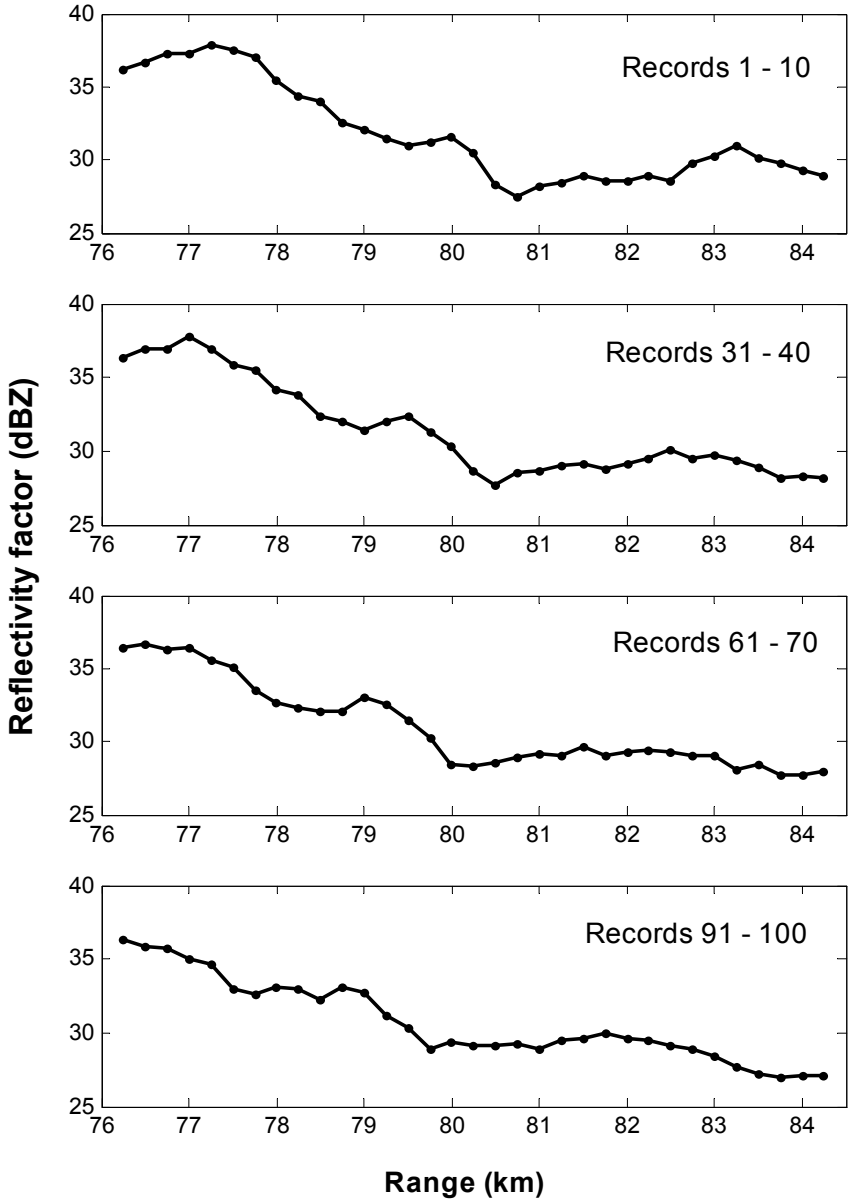

Figure 4. Estimates of reflectivity factor on sets of 10 records spaced apart by 20 s, using an oversampling factor $L = 3$ (SNR > 35 dB).

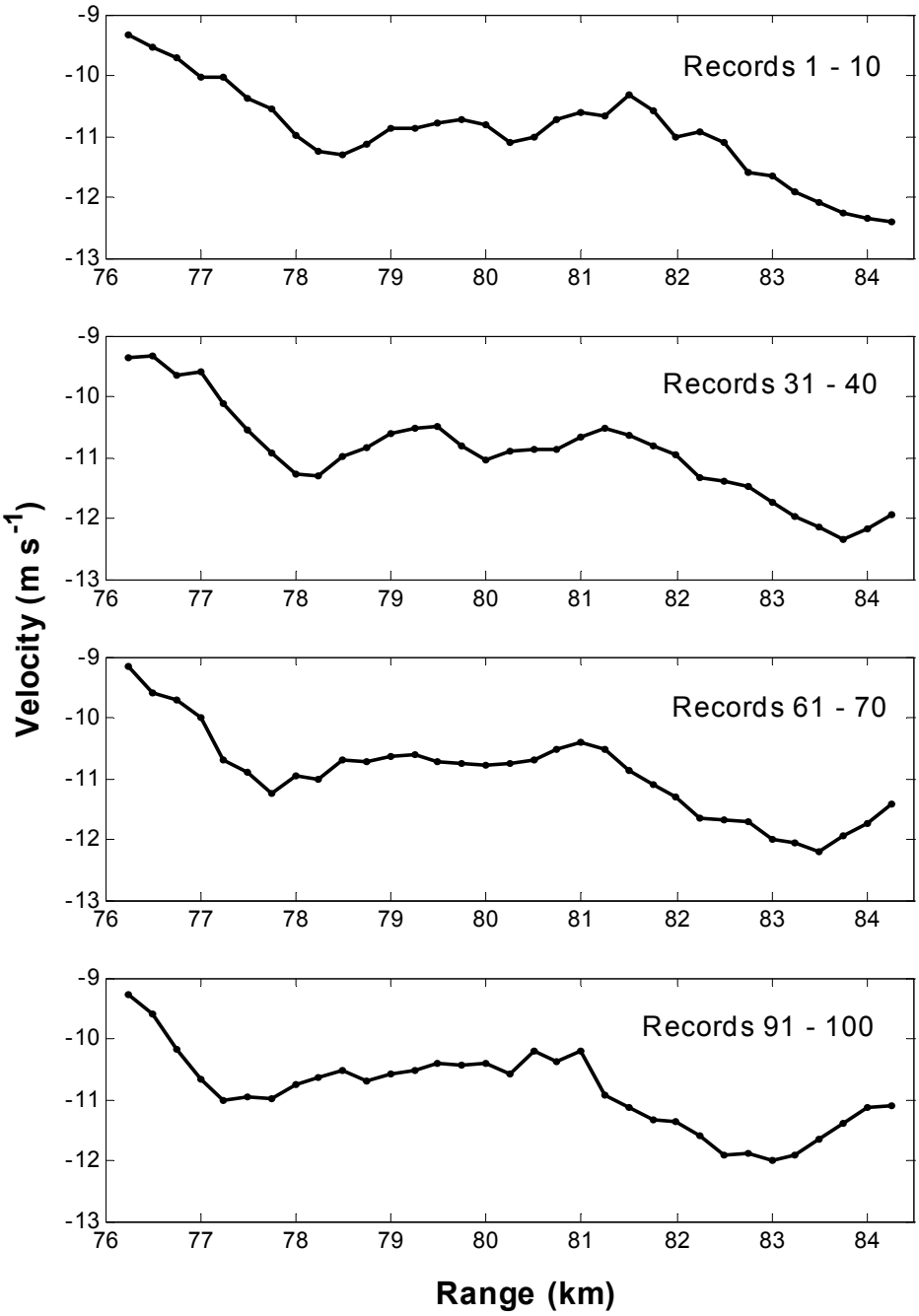

Figure 5. Estimates of mean Doppler velocity on sets of 10 records spaced apart by 20 s, using an oversampling factor $L = 3$ (SNR > 35 dB).

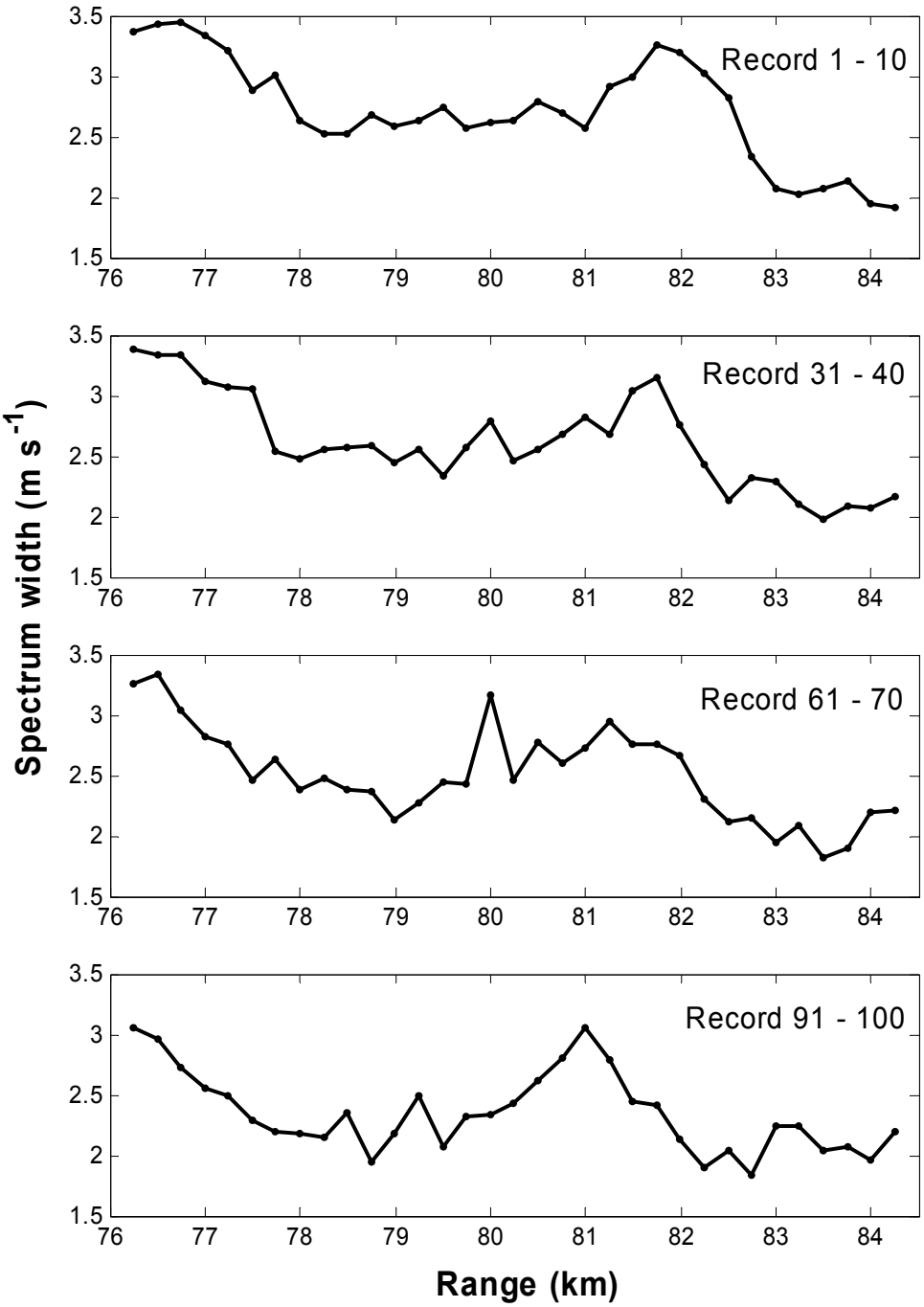

Figure 6. Estimates of Doppler spectrum width on sets of 10 records spaced apart by 20 s, using an oversampling factor $L = 3$ (SNR > 35 dB).

Appendix C

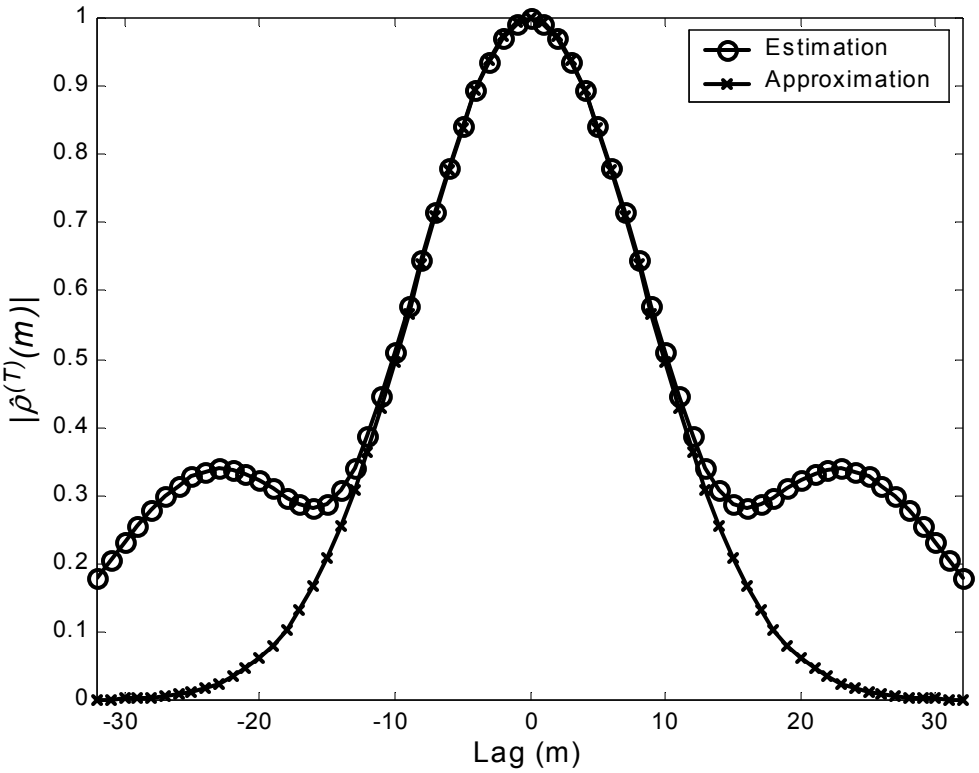

Figure 7. Estimated and approximated autocorrelation coefficient along sample time for the difference threshold set at 30%.

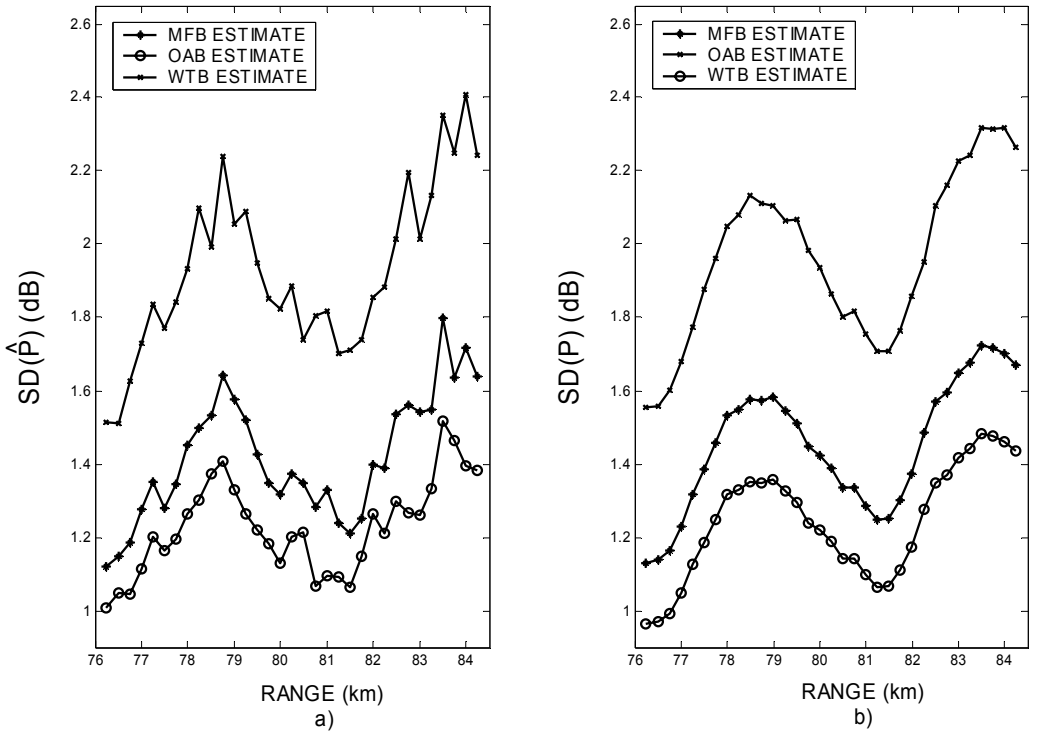

Figure 8. (*a*) Experimental and (*b*) theoretical normalized standard deviation of power estimates in dB for an oversampling factor of $L = 3$.

Appendix C

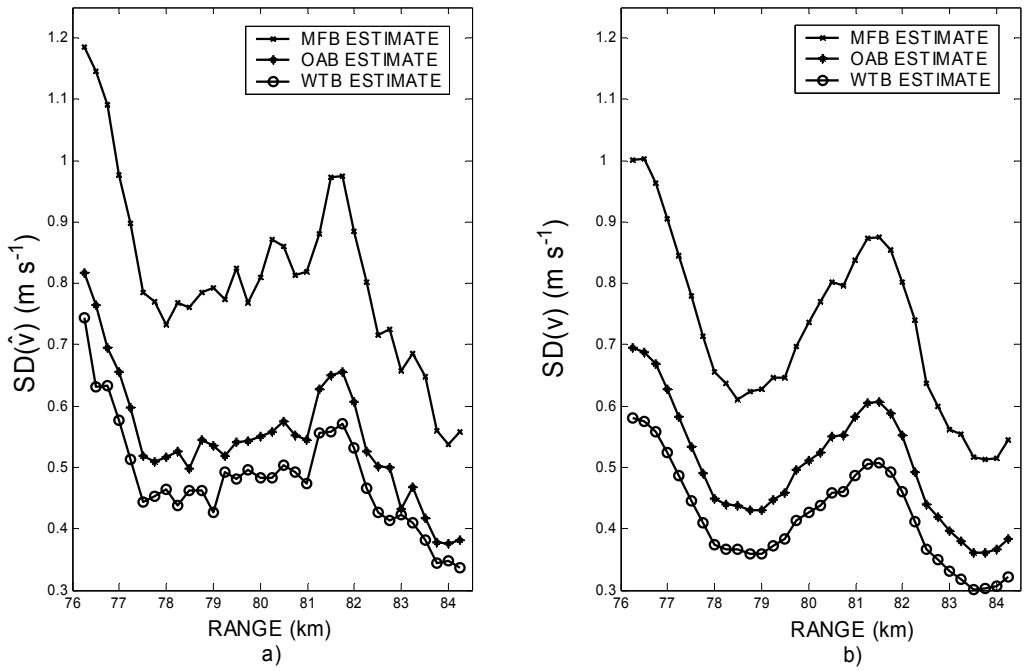

Figure 9. (*a*) Experimental and (*b*) theoretical standard deviation of velocity estimates for an oversampling factor of $L = 3$.

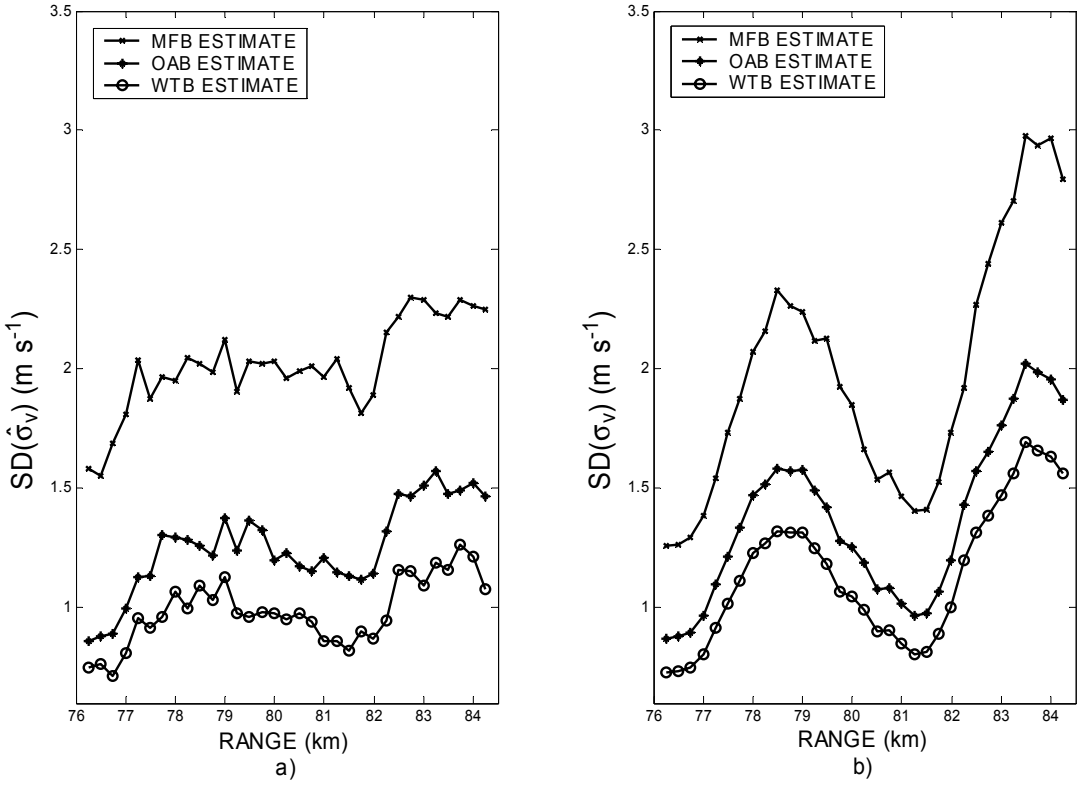

Figure 10. (*a*) Experimental and (*b*) theoretical standard deviations of Doppler spectrum width estimates for an oversampling factor of $L = 3$.

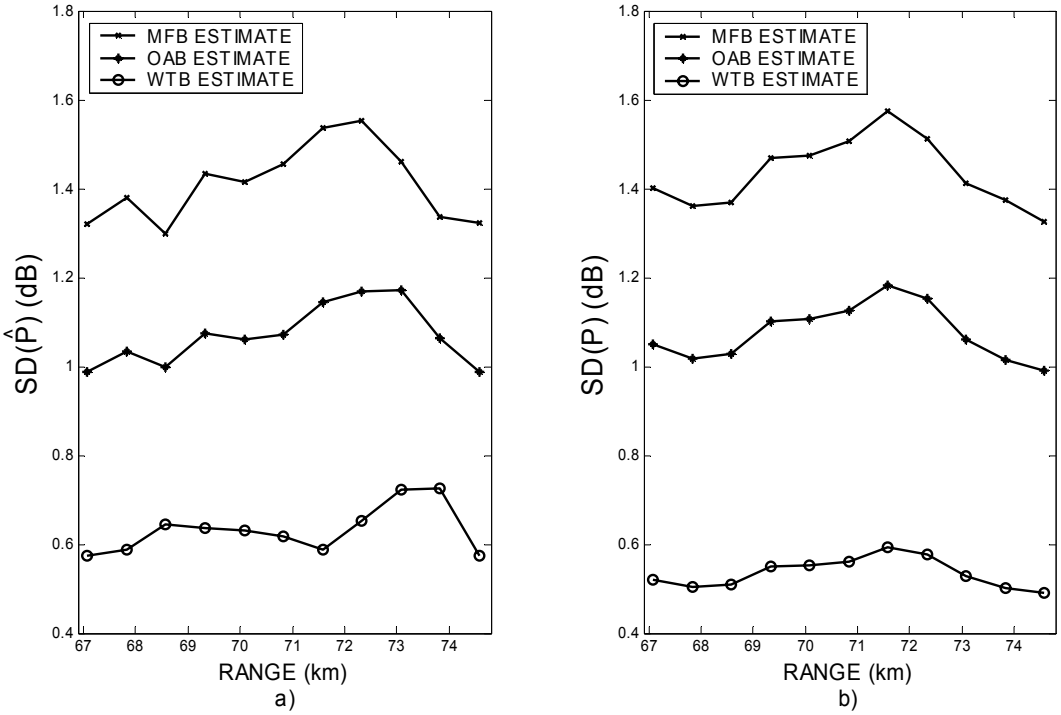

Figure 11. (*a*) Experimental and (*b*) theoretical normalized standard deviation of power estimates in dB for an oversampling factor of $L = 9$.

Appendix C

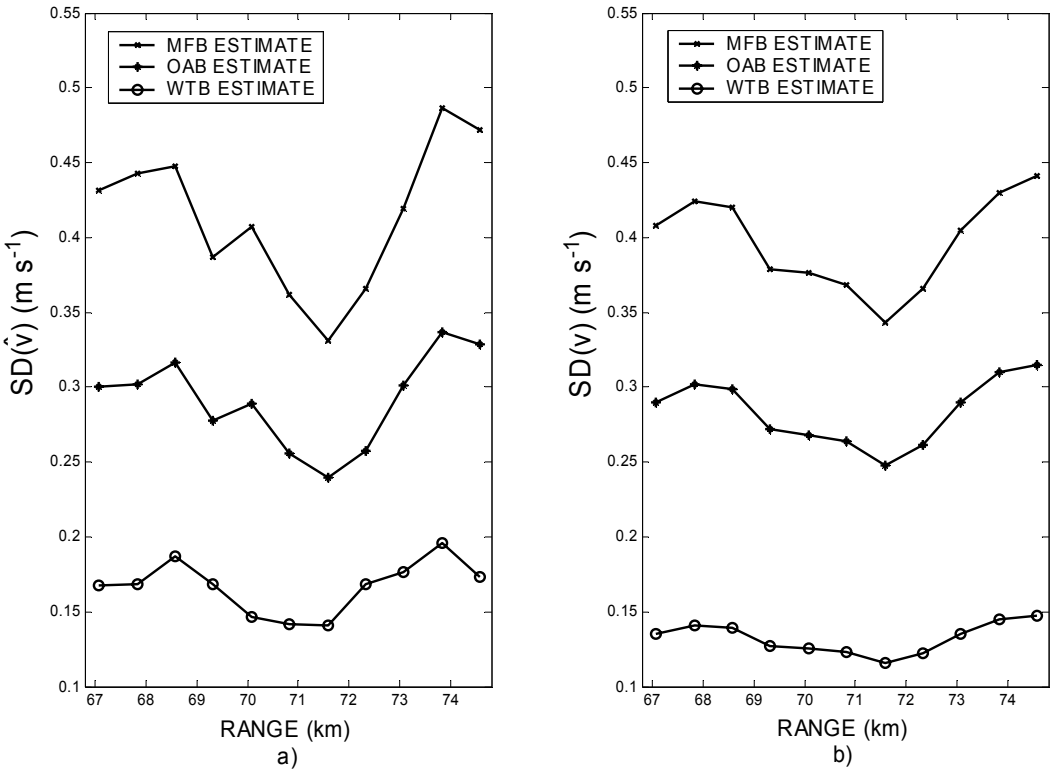

Figure 12. (*a*) Experimental and (*b*) theoretical standard deviation of velocity estimates for an oversampling factor of $L = 9$.

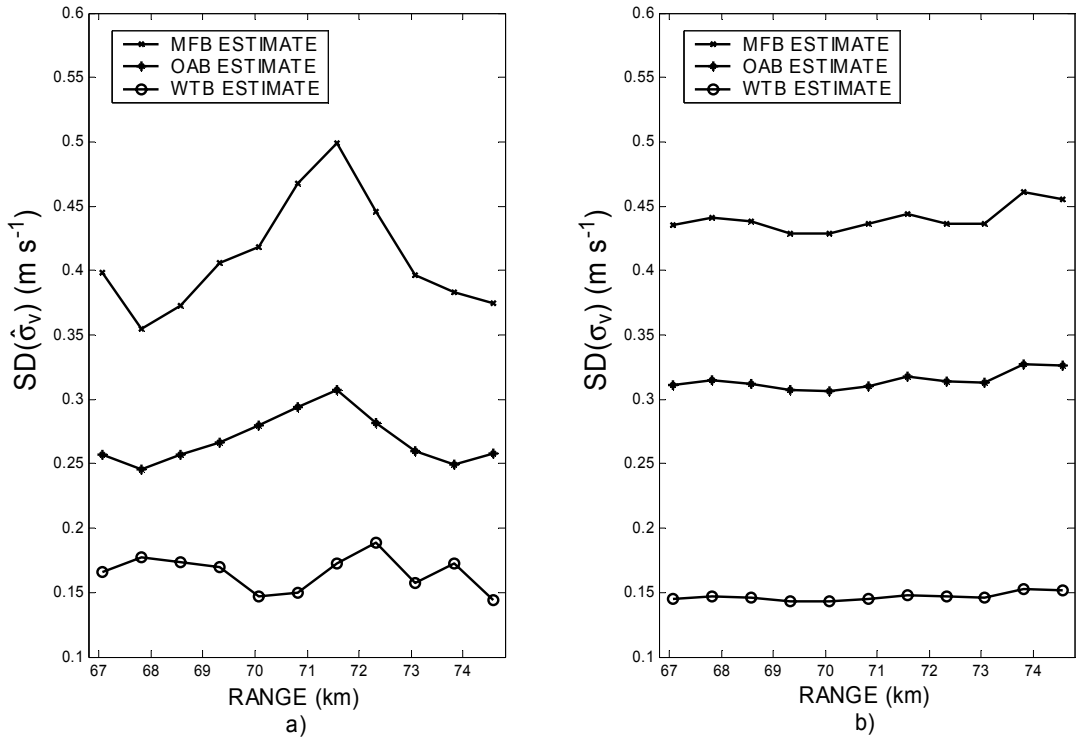

Figure 13. (*a*) Experimental and (*b*) theoretical standard deviations of Doppler spectrum width estimates for an oversampling factor of $L = 9$.

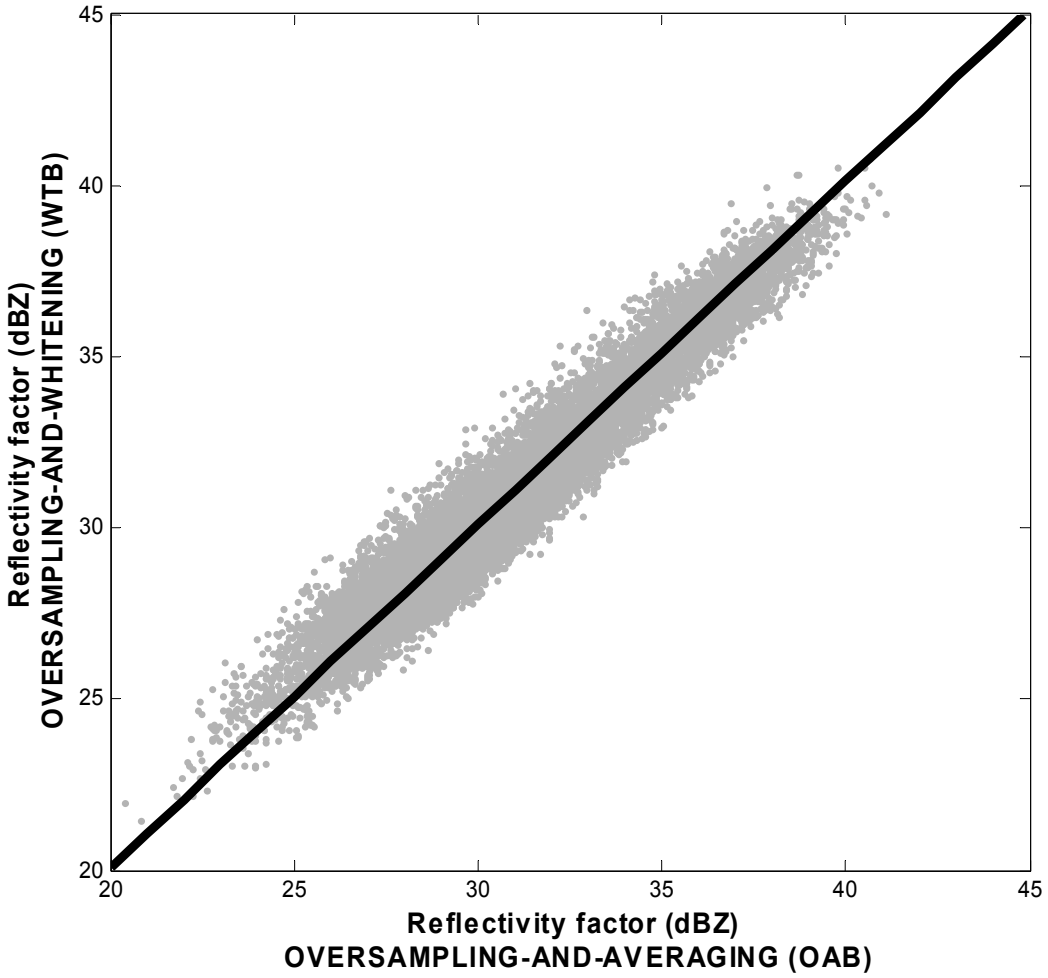

Figure 14. Scatter plot of WTB versus OAB power estimates. The solid line is the best fit in the least squares sense.

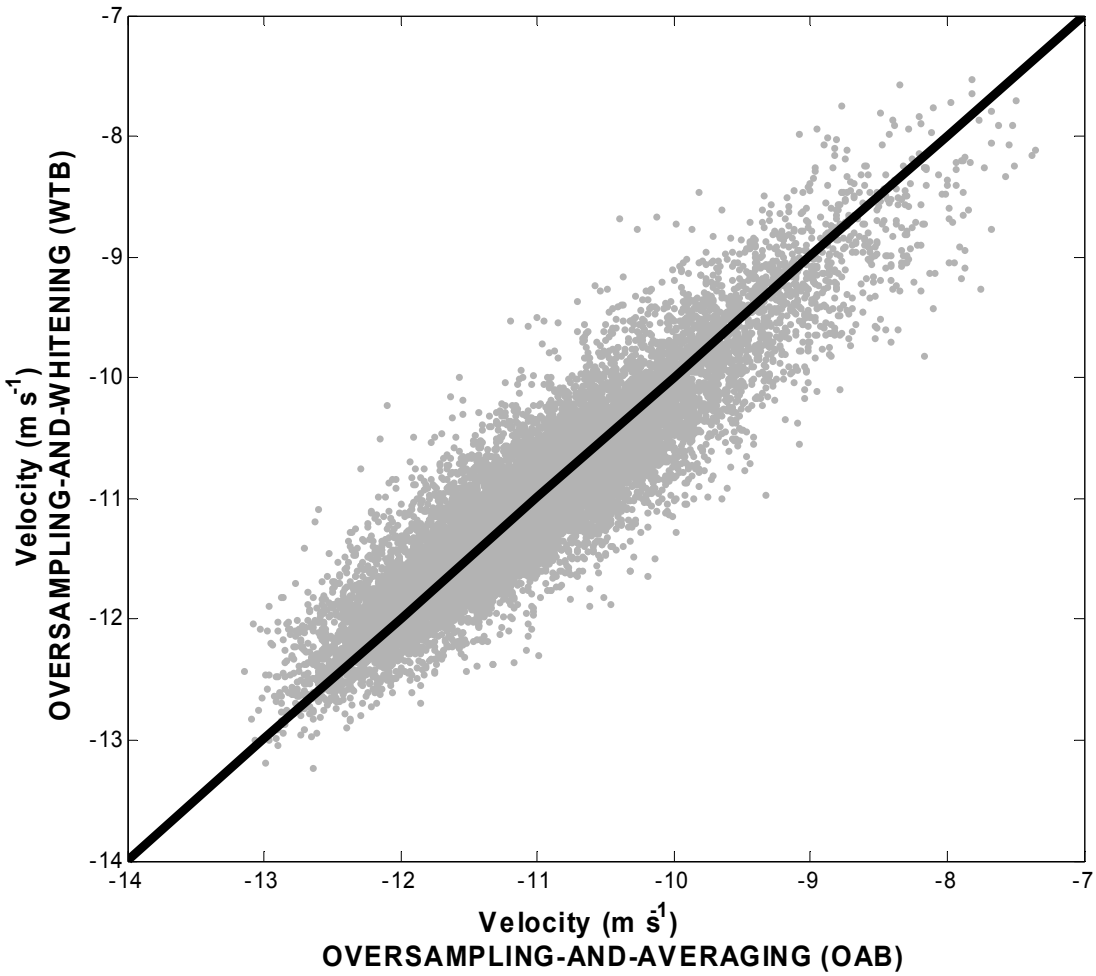

Figure 15. Scatter plot of WTB versus OAB velocity estimates. The solid line is the best fit in the least squares sense.

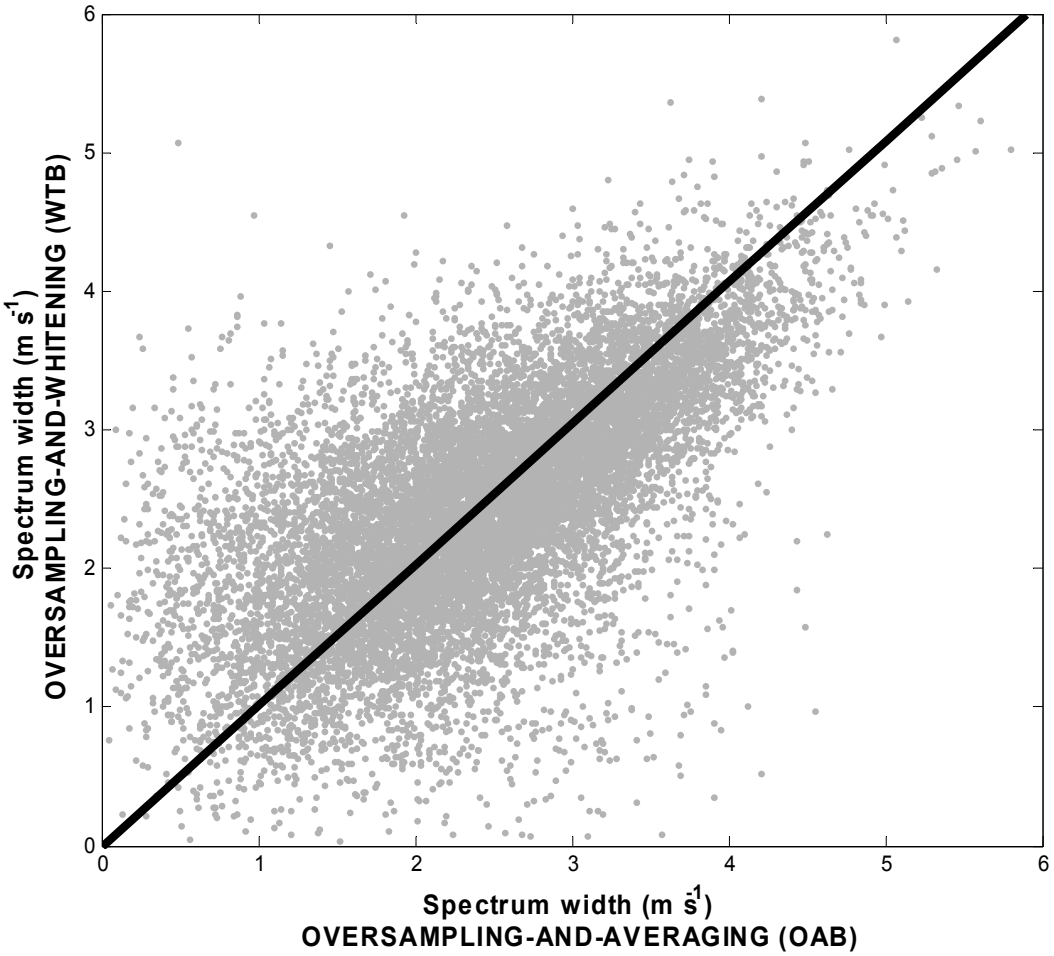

Figure 16. Scatter plot of WTB versus OAB spectrum width estimates. The solid line is the best fit in the least squares sense.

Appendix C

	$\frac{\mathrm{var}\left(\hat{X}_{MFB}\right)}{\mathrm{var}\left(\hat{X}_{OAB}\right)}$	$\frac{\mathrm{var}\left(\hat{X}_{MFBt}\right)}{\mathrm{var}\left(\hat{X}_{OABt}\right)}$	$\frac{\mathrm{var}\left(\hat{X}_{MFB}\right)}{\mathrm{var}\left(\hat{X}_{WTB}\right)}$	$\frac{\mathrm{var}\left(\hat{X}_{MFBt}\right)}{\mathrm{var}\left(\hat{X}_{WTBt}\right)}$	$\frac{\mathrm{var}\left(\hat{X}_{OAB}\right)}{\mathrm{var}\left(\hat{X}_{WTB}\right)}$	$\frac{\mathrm{var}\left(\hat{X}_{OABt}\right)}{\mathrm{var}\left(\hat{X}_{WTBt}\right)}$
X = P	2.105955	2.073276	3.071418	2.970985	1.436999	1.432994
X = v	2.238192	2.082410	2.942816	2.983750	1.317445	1.432994
X = σ_v	2.791660	2.092170	4.655921	2.998174	1.722260	1.432994

Table 1. Variance ratios obtained for $L = 3$. The acronyms in the subscript are defined as follows: MFB – matched-filter-based estimate; OAB– oversampling-and-average-based; WTB – whitenening-transformation-based; t - theoretical.

Appendix D

Winter Storm Studies: Video Disdrometer Measurements

30 September 2003

Edward A. Brandes and Kyoko Ikeda
National Center for Atmospheric Research
P.O. Box 3000
Boulder, CO 80307

1. Introduction

A 2D-video disdrometer developed by Joanneum Research Inc., located in Graz, Austria, has been operating at NCAR's Marshall observation site since July 2002. Hydrometeor observations from more than a dozen storms were collected during the winter of 2002-2003. The data are being used to study shape characteristics of frozen hydrometeors, particle canting angles, terminal velocities, and densities. The disdrometer observations are needed to verify polarimetric radar signatures and particle distribution information retrieved from radar measurements. The ultimate goals are to determine if polarimetric radar measurements can be used to estimate the density of frozen hydrometeors and visibility in snowstorms and to improve the quantification of winter precipitation.

Here we present a description of the disdrometer and show sample hydrometeor images. System bias corrections are discussed, and examples from winter storms are given.

2. Disdrometer description

The disdrometer consists of two line-scan cameras providing front (camera A) and side (camera B) views of hydrometeors falling into the instrument. Each camera has a single line of 700 photo-detectors positioned opposite a light source. Hydrometeors falling through the measuring area block the light source, shadowing some of the photo-detectors. The number of blocked photo-detectors is recorded for each camera at a frequency of 34.1 kHz. The sampling creates image projection slices of the hydrometeors.

Information provided on individual hydrometeors includes silhouette images, height and width information from each camera, and the particle terminal velocity. Hydrometeor widths are computed from the number of shadowed photo-detectors. Particle heights are determined from the number of blocked line scans and the scan line height. Particle terminal velocity is computed from the vertical distance between the two camera planes and the time the hydrometeor takes to break each plane. Other hydrometeor parameters obtained are the particle axis ratio, canting angle, and horizontal velocity. The instrument has a measuring surface area of 10 cm x 10 cm.

Images of various hydrometeor types are shown in Fig. 1. The top left images show a moderate-size aggregate. The maximum height and width are 5.1 and 5.4 mm, respectively, from camera A and 5.1 and 4.7 mm from camera B. The fall velocity was 1.5 m s^{-1}. A raindrop having an equivalent volume diameter of ~3.5 mm is shown in the top right images. The oblate shape typical of large drops is reproduced. Images at the lower left are from a hailstone with a diameter of ~7 mm and having a fall velocity of 10.1 m s^{-1}. Images at the lower right show a snow pellet from a mixed-phase precipitation event. The equivalent-volume diameter and fall velocity are 3.3 mm and 3 m s^{-1}, respectively.

2. Calibration and data processing

Disdrometer observations of particle size are verified by dropping calibration spheres with known diameters (0.5–10 mm) into the instrument after mechanical and optical alignments have been checked. The measurements are compared with the nominal sizes to determine correction factors. Typically, our system yields uncalibrated particle heights that are ~10 percent taller than true size. A smaller adjustment is normally required for particle width.

Calibration shapes for verifying particle axis ratios are not available. Instead, this measurement is verified with raindrops. For light wind conditions and in the absence of drop collisions the relationship between drop flattening and drop size is well known. Fig. 2a shows the axis ratio with respect to estimated equivalent-volume diameters after dimension corrections were applied. The agreement between the axis ratios and the empirical relationship from Brandes et al. (2002) is excellent for the 17 March 2003 dataset. Offsets for the other two cases may be caused in part by drifts in the calibration and varying wind conditions. It is clear that the instrument has trouble with small particles. Part of the problem is related to spatial quantization (~0.15 mm for particle width). Data editing procedures are still under development.

Figure 2b shows the relationship between raindrop size and terminal velocity. The latter have been reduced to sea level. The Marshall site is located at an elevation of 1.742 km MSL. Lower air density causes fall speeds to be about 6% greater than at sea level. Except for the small drops, the observed terminal velocities closely follow the relationship from Brandes et al. (2002).

In summary, the instrument yields valid axis ratios and particle terminal velocities. Departures from expected values are predominately with small particles. Fortunately, radar measurements respond primarily to the larger particles that are well sampled. Direct comparisons between radar measurements and computed radar parameters determined from disdrometer observations are impacted by wind conditions, particularly for snowflakes because of their small terminal velocity.

3. Examples

On 17–18 March 2003, a dataset was collected from a storm in which precipitation began as rain and later changed to snow (Fig. 3). Eventually over 30 inches of snow was produced—immobilizing some Front Range communities. Rain began at the disdrometer site just before 2200 UTC on 17 March when the temperature was 5°C (Fig. 3). Over the next four hours, the temperature fell only 1°C. Wet snow first appeared at ~0200 UTC. Mixed-phase precipitation (rain and snow) continued until 0545 (UTC) when the temperature lowered to 1°C. Fig. 4 shows a sampling of particle fall velocities observed between 0220 and 0250 UTC. A mixture of rain and drizzle drops, partly-melted (mixed-phase) aggregates, and small snowflakes is evident. The unadjusted terminal velocities for the drops roughly follow the curves given by Atlas et al. (1973, in red) and Gunn and Kinzer (1949, in yellow)]. Wetted aggregates having diameters of ~2 mm fall with velocities between 1–2 m s^{-1} slower than raindrops of equivalent size. Terminal velocities for the snowflakes in the 0.5 and 2.0 mm size range are clustered near 1.0 m s^{-1} and show only a slight tendency to increase with size. After 0545 UTC, all hydrometeors were snowflakes with maximum sizes of ~5 mm. Size distributions were close to exponential (e.g., Fig. 5a). Although the total number of rimed aggregates and precipitation intensity increased

with time, the distribution remained exponential (Fig. 5b). Changes in terminal velocity and the size distribution corresponded with changes in crystal habit and the degree of riming and aggregation reported by on-site observers.

A case of a mixed-phase precipitation changing to snow occurred on 6 April 2003 (Fig. 6). Weather conditions were characterized by light winds (generally < 3 m s^{-1}) and decreasing temperatures. The disdrometer began detecting partly frozen hydrometeors at ~0330 UTC. Temperature decreased from 3 to 1°C in one hour (Fig. 6a). By 0436 UTC, snow aggregates became dominant. Fig. 6b presents the precipitation rate (liquid equivalent) taken as the average of three GEONOR gauges. The panel also presents an estimate of hydrometeor bulk density computed from volumetric data provided from the disdrometer (Fig. 6c) and one-minute interval liquid equivalent snowfall amounts from the gauges. The bulk density is ~1 g cm^{-3} during the mixed-phase period and about 0.25 g cm^{-3} for the snow portion of the event. Obviously, these values are too high. The “apparent” volume from the disdrometer could be too small either due to missed smaller particles or bias in estimates of individual particle volumes. The issue is being investigated.

Visibility data available from a HSS VPF-730 sensor can be compared to the disdrometer measurements. The optical distance measured by the sensor (Fig. 6d) exceeded 30 km prior to the onset of mixed-phase precipitation. Visibility rapidly decreased to an average of ~2.3 km during the mixed-phase precipitation stage. A significant further decrease in visibility from 2 km to 0.5 km began at 0440 UTC—roughly coinciding with the change to all snow. Temporal variations in snowfall rate and one-minute total snow volumes are correlated with visibility during the snow period. Rasmussen et al. (1999) previously studied the relationship between the (liquid equivalent) snowfall rate and visibility and concluded that visibility is dependent not only on cross-sectional area (or “apparent” volume) of snowflakes but also on crystal type, fall speed, degree of aggregation and riming, and time of day. Typically, for a given snowfall rate, the visibility increased when rimed and compact particles (e.g., graupel) were present due to their small cross-sectional areas and larger fall speeds. On the other hand, dry snowflakes are loosely packed and fall at a much slower rate (~1 m s^{-1}), causing reduced visibility. Yet another factor appears to be the relative humidity, which can be inferred from Fig. 6a. This suggests a multiple sensor approach may be needed to "predict" visibility.

4. Concluding remarks

The hope is that success achieved in improving the quantification of rainfall and retrieving drop-size distribution information from polarimetric radar measurements can be extended to winter storms. Current efforts seek to establish the shape and fall velocities of the various hydrometeor types and to determine disdrometer capabilities to retrieve this information. If particle distributions in winter storms are indeed close to exponential, the retrieval of the governing parameters that define the distribution from polarimetric measurements should be facilitated. Plans call for placing the disdrometer near NCAR's polarimetric radar as part of the WISP04 field program. As a first step, radar measurements and radar parameters computed from the disdrometer observations are to be compared.

REFERENCES

Atlas, D., R. C. Shrivastava, and R. S. Sekhon, 1973: Doppler radar characteristics of precipitation at vertical incidence. *Rev. Geophys. Space Phys.*, **11**, 1–35.

Brandes, E. A., G. Zhang, and J. Vivekanandan, 2002: Experiments in rainfall estimation with a polarimetric radar in a subtropical environment. *J. Appl. Meteor.*, **41**, 674–685.

Gunn, R., and G.D. Kinzer, 1949: The terminal velocity of fall for water drops in stagnant air. *J. Meteor. Soc.*, **6**, 243–248.

Rasmussen, R. M., J. Vivekanandan, J. Cole, B. Myers, and C. Masters, 1999: The estimation of snowfall rate using visibility. *J. Appl. Meteor.*, **38,** 1542–1563.

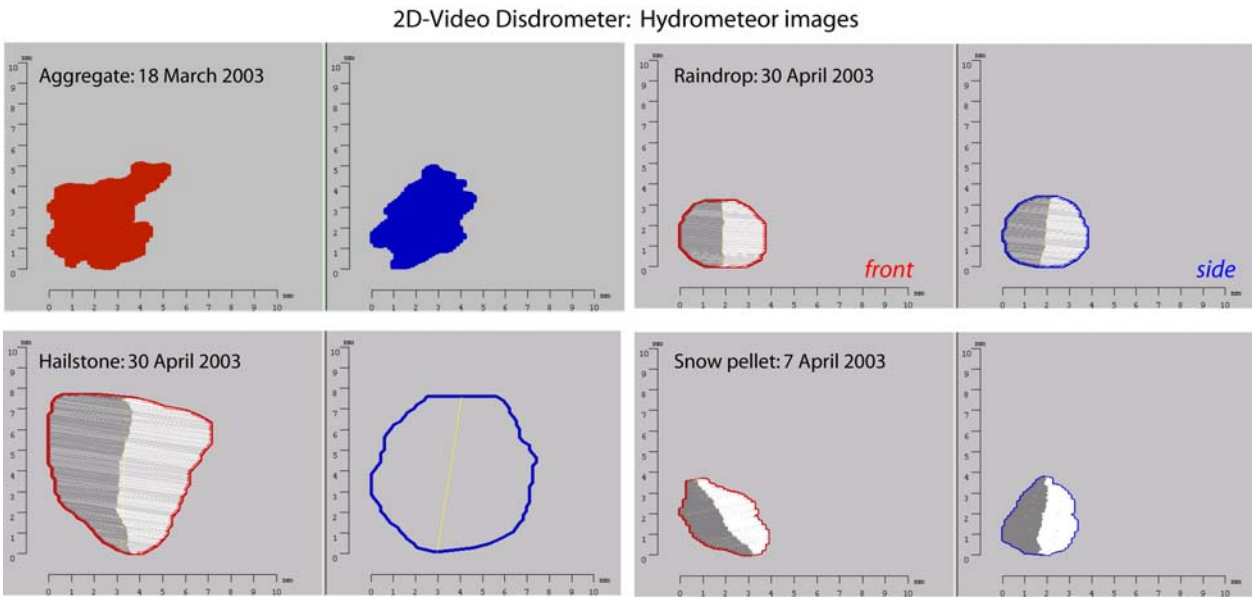

FIG. 1: Sample hydrometeor images (front and side views) for indicated particle types.

a)

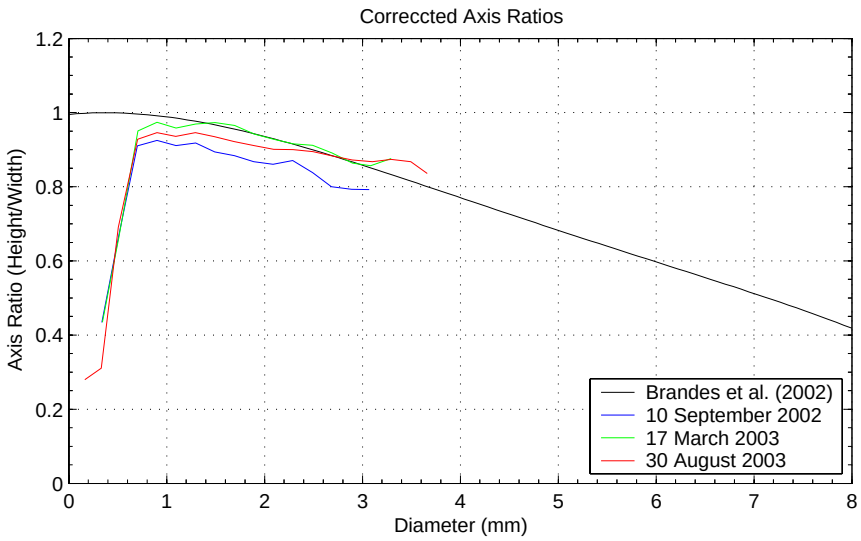

b)

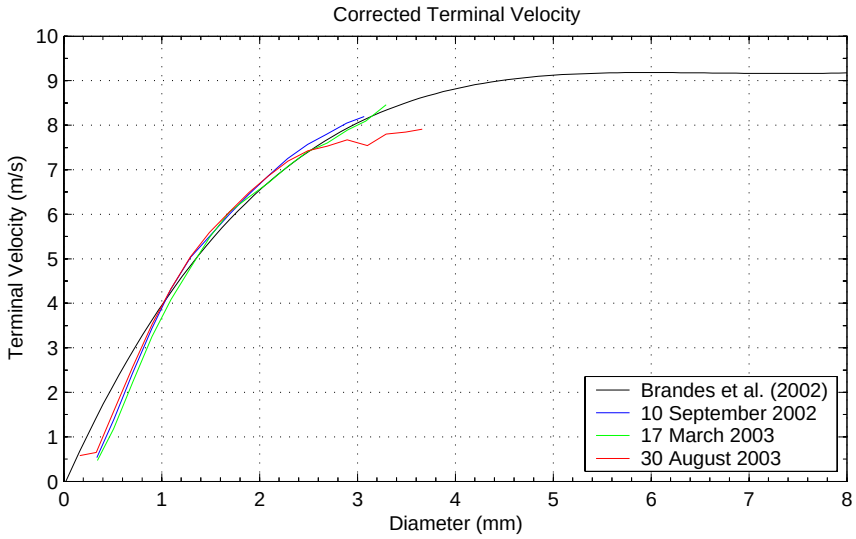

FIG. 2: Observed raindrop axis ratios (panel a) and terminal velocities (b) plotted versus equivalent-volume diameter. Size and air density corrections have been applied. Curves show expected relations from Brandes et al. (2002).

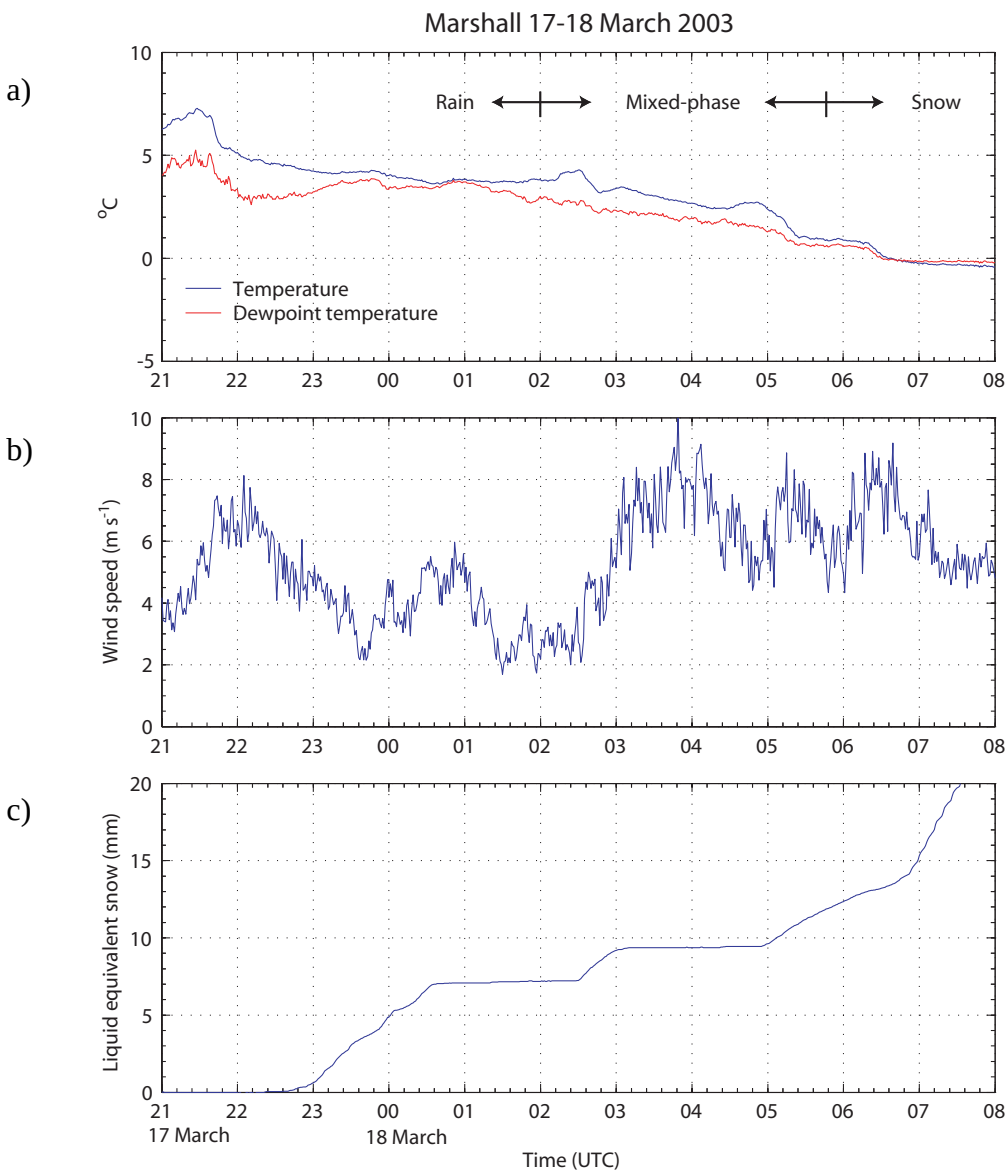

FIG. 3: Surface temperature and dew point (panel a) in ^{o}C, wind speed (b) in m s^{-1}, and liquid-equivalent accumulative snow amount (c) in mm from 2100 UTC 17 March to 0800 UTC 18 March 2003. Characteristic precipitation types are indicated.

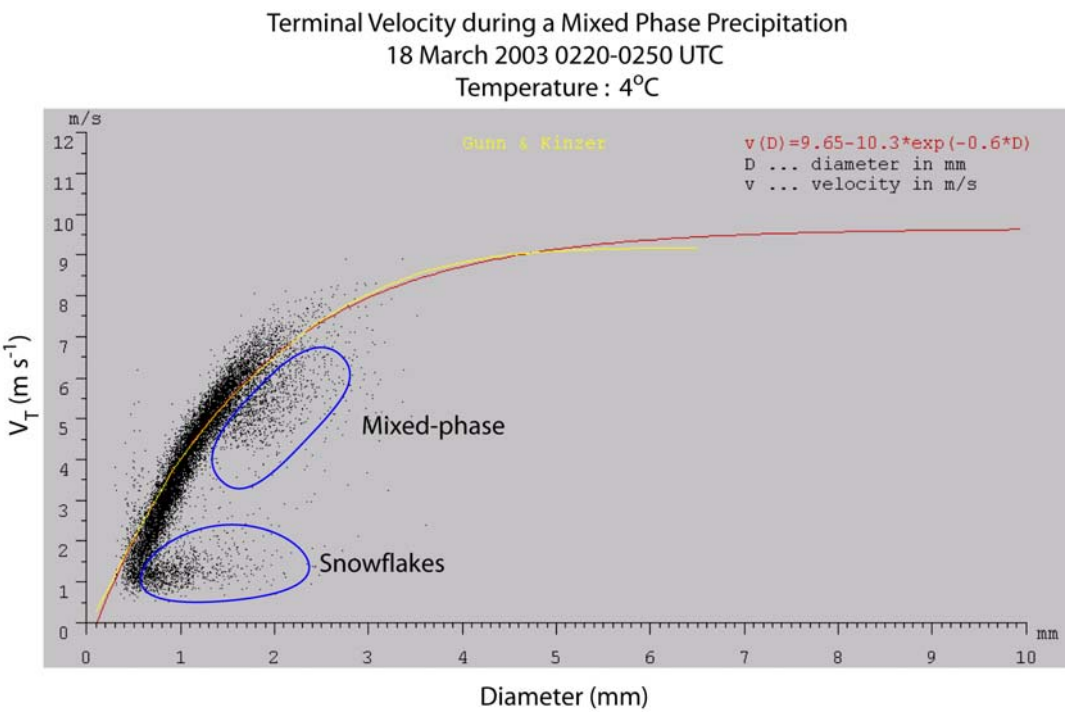

FIG. 4: Terminal velocity versus diameter from the video disdrometer display software for 0220-0250 UTC on 18 March 2003. The curves are terminal velocity–diameter relations from Atlas et al. (1973) [red] and Gunn and Kinzer (1949) [yellow].

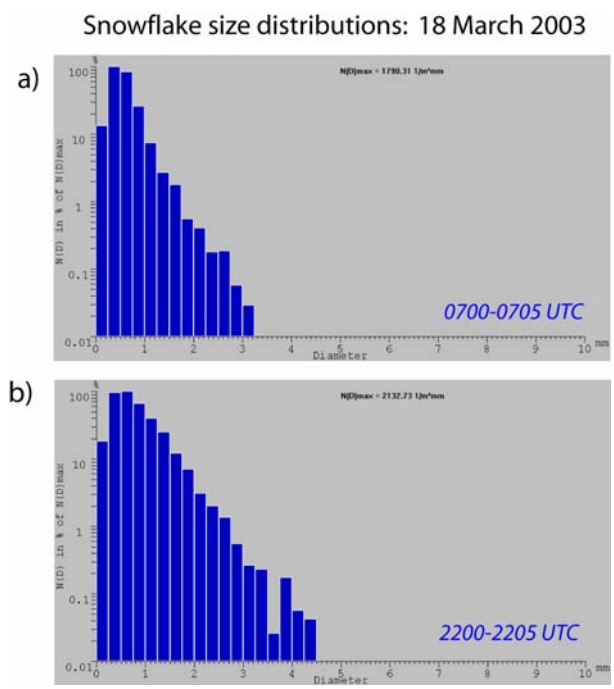

Fig. 5: Five-minute averaged snowflake distributions for 0700–0705 UTC (a) and 2200–2205 UTC (b) on 18 March 2003.

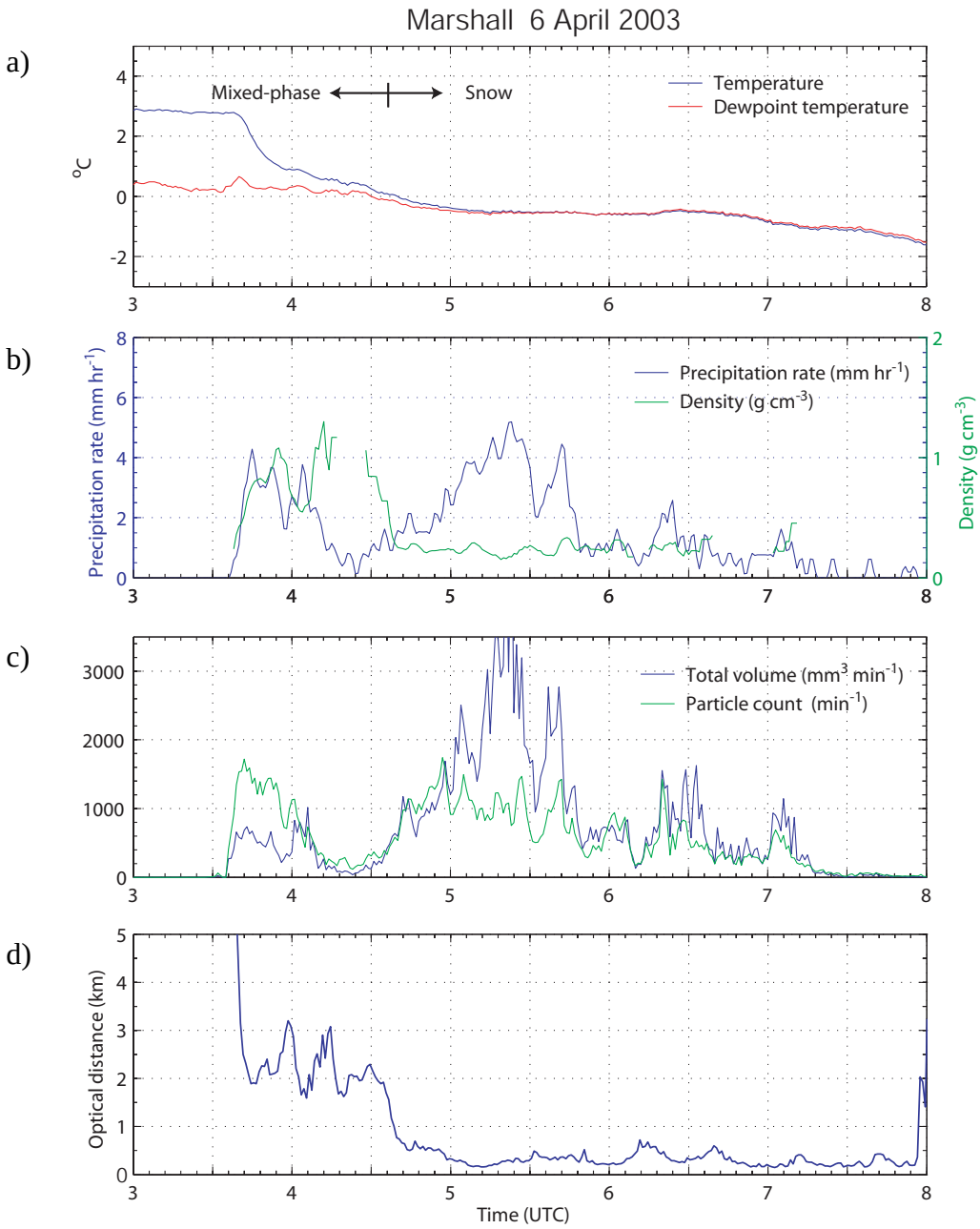

FIG. 6: Surface temperature and dew point (a) in ^{o}C, liquid equivalent precipitation rate in mm h^{-1} and one-minute averaged hydrometeor bulk density in g cm^{-3} (b), one-minute total hydrometeor volume in mm^3 min^{-1} and particle number count in min^{-1} (c), and optical distance in km (d) from a visibility sensor. The change from mixed-phase to snow is indicated. (6 April 2003)

Appendix E

Hail Detection with Polarimetric Radar

30 September 2003

Edward A. Brandes

Research Applications Program
National Center for Atmospheric Research

Alexander V. Ryzhkov

Cooperative Institute for Mesoscale Meteorological Studies, University of Oklahoma
and
National Severe Storms Laboratory

1. Introduction

Algorithms to detect hail with polarimetric measurements are based largely on the departure of measurements from the "rain-only" case.[1] Detection is, for example, readily accomplished with the radar reflectivity at horizontal polarization (Z_H) and differential reflectivity (Z_{DR}) measurement pair. The presence of hail causes reflectivity to become large because of the 6th power dependency on the size of hydrometeors illuminated by the radar beam. Differential reflectivity (in dB) is defined as $10\times\log(Z_H/Z_V)$ where Z_V is the reflectivity at vertical polarization and Z_H and Z_V have units of mm^{-6} m^{-3}. Raindrops tend to flatten in the horizontal as they fall causing Z_{DR} to have positive values, generally in the range 0.3 to 3 dB, depending on the reflectivity magnitude. Hail tends to tumble as it falls creating a random distribution of axis orientations. For tumbling hail, Z_H and Z_V are similar in value; and differential reflectivity becomes small compared to the rain case.

The linear depolarization ratio (LDR) and co-polar correlation coefficient (ρ_{HV}) also hold promise for hail detection. LDR (in dB) is defined as $10\times\log(Z_{VH}/Z_H)$, where Z_{VH} is the cross-polar return measured in the vertical for a transmitted horizontally polarized signal. The LDR signal arises from aspherical particles that are canted with respect to the transmitted energy or tumble as they fall. Magnitudes for hail and mixed-phase precipitation typically are >-25 dB but can approach -10 dB for large hail. The signal for rain is <-25 dB. The presence of hail reduces ρ_{HV} for precipitation media composed of rain from ~0.99 to about 0.90. Also, the differential propagation phase (Φ_{DP}) can be used for hail detection. The parameter is insensitive to the presence of small hail that tumbles, but it is sensitive to hail in the Mie scattering range through a backscattering phase shift.

Hail detection with polarimetric radar has distinct advantages over techniques based on radar reflectivity. Reflectivity-based techniques typically assume a threshold value (e.g., 55 dBZ) that if exceeded indicates hail. Experience has shown that the threshold varies for different climatological regions and that the threshold for specific days is determined by meteorological conditions. Further, the current WSR-88D algorithm (Witt et al. 1998) makes designations based

[1] Additional reviews of polarimetric radar techniques for detecting hail are given by Balakrishnan and Zrnić, 1990) and Smyth et al. (1999).

on storm structure and environmental factors which are difficult to quantify. The algorithm predicts the probability of hail (any size) and the probability of severe hail (hail with diameters >19 mm). Designations are made for storms—the hail location is not specified. In contrast, hail designations with polarimetric measurements are based on hydrometeor geometry. The precise hail location can be specified, and size can be estimated from radar measurements rather than inferred from environmental factors.

2. Hail differential reflectivity

A simple hail-detection algorithm was proposed by Aydin et al. (1986) who defined a hail differential reflectivity parameter (H_{DR}) given by

$$H_{DR} = Z_H - f(Z_{DR})$$

where

$$\begin{aligned} f(Z_{DR}) &= 27 \text{ dB} & Z_{DR} &\le 0 \text{ dB} \\ f(Z_{DR}) &= 19*Z_{DR} + 27 \text{ dB} & 0 \le Z_{DR} &\le 1.74 \text{ dB} \\ f(Z_{DR}) &= 60 \text{ dB} & Z_{DR} &> 1.74 \text{ dB} \quad . \end{aligned}$$

The units of Z_H and Z_{DR} are dBZ and dB, respectively. The segmented line $f(Z_{DR})$ attempts to separate rain-only and hail-contaminated polarimetric measurements when plotted in Z_H–Z_{DR} space. The line was determined with disdrometer observations from rainstorms observed in Illinois and Colorado. A positive value of H_{DR} indicates hail. The magnitude of H_{DR} provides an estimate of hail size (Brandes and Vivekanandan 1998). Although the boundary accounts for measurement errors in Z_H and Z_{DR} and allows for drop oscillations, Aydin et al. assumed that drop shapes were determined primarily by forces of surface tension and hydrostatic pressure (Green 1975).

Subsequent studies have shown that radar-apparent mean drop shapes are more spherical in the mean than the shapes of Green. A relation that approximates these shapes is (Brandes et al. 2002)

$$R = 0.9951 + 0.02510D - 0.03644D^2 + 0.005030D^3 - 0.000249D^4 \quad , \qquad (1)$$

where R is the drop axis ratio (vertical dimension divided by the horizontal dimension) and D (in mm) is the drop equivalent-volume diameter. Figure 1 shows a plot of reflectivity and differential reflectivity as computed from disdrometer observations obtained in Florida. The discriminator of Aydin et al. results in a number of false hail designations in the 30–50 dBZ range. The curved line represents the lower boundary of the rain regime. The equation for the line, determined experimentally, with Z_H in dBZ is

$$Z_{DR} = \exp(3.12*10^{-4}Z_H^2 + 6.48*10^{-2}Z_H - 3.87) \quad . \qquad (2)$$

This curve better captures the shape of the Z_H–Z_{DR} distribution and represents an improvement over the boundary of Aydin et al.—particularly for reducing false alarms at moderate reflectivity values. Hail-contaminated radar measurements, particularly when large hail is present, would

normally lie to the right of and below the curve. Application to a severe hailstorm is shown in Fig. 2. Data points to the right of the curve result from the negative correlation between Z_H and Z_{DR} that occurs when hail is present, whereby hail increases Z_H because of its size and reduces Z_{DR} because it tumbles.

Raindrop measurements close to the boundary given by (2) tend to be characterized by drop-size distributions (DSDs) that are essentially in equilibrium, that is, a rough balance exists between drop breakup and accretion. These measurements have a minimum median drop diameter (D_0) and maximum number concentration for a given reflectivity value. Radar data points to the right of the curve not contaminated by ground clutter or influenced by side lobes almost certainly associate with hail.

There is a potential problem with the above approach. Unfortunately, little rain falls with an equilibrium drop distribution. Indeed, the variability among data points in Fig. 1 attests to the large spatial and temporal fluctuations in DSDs. The leading edge of strong convection is often characterized by DSDs with small numbers of large drops that can result in observations well above the rain–hail boundary in Fig. 2. For example, consider a reflectivity measurement of 50 dBZ paired with a differential reflectivity of 2.5 dB. If hail were added to the measurement volume, Z_H would increase and Z_{DR} would decrease. The hail-contaminated measurement would move downward and to the right on the figure but would not necessarily be displaced across the rain–hail boundary. Hence, some hail-contaminated data points may reside above the boundary.

3. Differential propagation phase and radar reflectivity

For raindrops a differential phase shift (Φ_{DP}) occurs between propagating horizontally and vertically polarized waves that at a distance r is given by

$$\Phi_{DP}(r) = \phi_0 + \delta(r) + \int_0^r K_{DP}(r)dr$$

where ϕ_0 is the radar hardware offset between signals at the two polarizations, δ is the backscatter differential phase shift, and K_{DP} is the two-way specific differential phase due to propagation. K_{DP} is the range derivative of Φ_{DP}, which in the absence of backscatter phase shifts generally increases monotonically with range. Hail that is spherical or tumbling will not contribute to K_{DP}. Oriented hail will have little impact if it is dry because of its small refractive index. Wetted hail in the Mie scattering range (hail with a diameter greater than 0.07 times the radar wavelength) typically produce negative values of δ and can cause Φ_{DP} to decrease with range.

Balakrishnan and Zrnić (1990) proposed to identify hail with departures in Z_H and K_{DP} measurement pairs from the rain-only case. The presence of hail increases Z_H because of the D^6 dependence. If the hail tumbles or is dry, it makes negligible contribution to K_{DP}. Thus, the K_{DP} value calculated from the radar measurements of Φ_{DP} will be smaller than that expected for the measured Z_H if only rain were present. This approach was examined by Ryzhkov and Zrnić (1994). Their Fig. 6, which has many of the characteristics seen in Fig. 2, shows that observations from the rainy regions within a storm did not agree very well with the theoretical rain-only relation. They cite potential problems with radar calibration and speculate that the measurements were influenced by the presence of ice cores. A contributor to the problem could

be the use of a Marshall-Palmer DSD with Green's (1975) axis ratios.

4. Fuzzy logic approach

Recognizing that polarimetric signatures for hail are not always unique and overlap those for other hydrometeors, fuzzy logic approaches using the full suite of polarimetric measurements have been proposed (e.g., Vivekanandan et al. 1999). Membership functions are employed to determine the degree to which a particular measurement represents the likelihood of hail. For example, the membership function for reflectivity may assign a membership value of 0 for a reflectivity value less than 45 dBZ essentially indicating that hail is unlikely. The value may be 1 for a reflectivity greater than 50 dBZ. The membership function might increase linearly for intermediate values. Membership values for differential reflectivity are determined according to the magnitude of the observed reflectivity. Small Z_{DR} at low reflectivity would be an indication of small drops, but the same value at high reflectivity would be indicative of tumbling hail. Each radar parameter is weighed and the most likely hydrometeor type selected.

The current NCAR hydrometeor classification algorithm (HCA) attempts to make designations for hail and rain–hail, graupel–hail, and graupel–rain mixtures. An example of hail detection is presented in Fig. 3. The various panels show the radar measurements and present a detailed "prediction" of hydrometeor types. Regions of hail, rain–hail, graupel–hail, and graupel–rain are indicated. Hail regions are surrounded by rain–hail regions. There are significant areas of graupel–hail at the periphery of the general hail region. Finally, a few designations indicate a graupel–rain mixture. The designations seem plausible. However, verification of the various categories will require a focused effort. For aviation purposes a simple designation for hail—perhaps with a size estimate—may be more appropriate.

5. Consistency method

This method is a variation of that using radar reflectivity and specific differential propagation phase. Consistency among Z_H, Z_{DR}, and K_{DP} dictates that any two of these parameters can be used to determine the third parameter (Goddard et al. 1994). For example, K_{DP} can be calculated from Z_H and Z_{DR} with (Vivekanandan et al. 2003)

$$K_{DP} = 3.32\times10^{-5} Z_H Z_{DR}^{-2.053} \quad , \qquad (3)$$

where the units of terms are linear and drop axis ratios given by (1) are used. Calculated values of K_{DP} can be compared with the measured values, and a hail parameter (HP) determined as

$$HP = K_{DP,m} - K_{DP,c} \quad ,$$

where $K_{DP,m}$ is the radar determined specific differential phase based on measurements of Φ_{DP} and $K_{DP,c}$ is the estimated value computed with (3) from radial distributions of Z_H and Z_{DR}. The presence of hail will generally reduce $K_{DP,m}$ relative to $K_{DP,c}$. HP should be close to 0° km^{-1} for rain. Significant departures of HP from 0° km^{-1}, beyond that expected from statistical error, would indicate hail.

Figure 4 presents a radial segment of measurements obtained for the storm in Fig. 3. The dips in the Z_{DR} trace between 40 and 41.5 km and between 42 and 47 km and the coincident

large values of Z_H are suggestive of hail. Note the large spatial variance in the radar measurements and the absence of distinct hail signatures in ρ_{HV} and LDR. Hail and graupel designations with the NCAR HCA and HP values along the radial are shown in Fig. 5. Negative HPs are truncated at -50° km^{-1}. These large negative values are due to the slightly negative Z_{DR}s that often characterize large hail. Rain rates computed from the Z_H–Z_{DR} measurement pairs are astronomical.

The HP parameter essentially predicts hail in the same locations as the fuzzy logic and H_{DR} methods. However, ambiguities about whether or not the measurement represents simply hail or mixtures of hail and other hydrometeors are avoided, and rain-only and hail contaminated regions are clearly separated. The approach is simpler than the fuzzy logic method in that it has fewer tuneable parameters. Moreover, the magnitude of HP is an indicator of hail size. A caveat with this method concerns the high noise level in radar-derived values of K_{DP}. To reduce the error considerable filtering of the measured Φ_{DP} is required. Filtering reduces the magnitude of peak K_{DP} values and spreads the signal into surrounding areas of smaller K_{DP}. Hence, the first signs of a hailfall may be missed. On the other hand, the size of the hail region may be overestimated resulting in a buffer zone about the hail shaft.

6. Planned research

Fortunately, the suite of polarimetric measurements provides redundant information regarding hailfalls. While all polarimetric parameters afford improvement when combined with radar reflectivity, the optimum parameter mix in an algorithm is yet to be determined. Existing radar datasets and in situ verification from field programs conducted in Florida, Colorado, and Oklahoma are available for analysis. A plan for testing candidate algorithms is being developed. The polarimetric measurements should also support the development of an algorithm component for estimating hailstone size.

REFERENCES

Aydin, K, T. A. Seliga, and V. Balaji, 1986: Remote sensing of hail with a dual linear polarization radar. *J. Climate and Appl. Meteor.,* **25,** 1475–1484.

Balakrishnan, N., and D. S. Zrnić, 1990: Estimation of rain and hail rates in mixed-phase precipitation. *J. Atmos. Sci.,* **47,** 565–683.

Brandes, E. A., and J. Vivekanandan: 1998: An exploratory study in hail detection with polarimetric radar. *Preprints,* 14th International Conference on Interactive Information and Processing Systems for Meteorology, Oceanography, and Hydrology. Phoenix, Arizona, Amer. Meteor. Soc., 287–290.

Brandes, E. A., G. Zhang, and J. Vivekanandan, 2002: Experiments in rainfall estimation with a polarimetric radar in a subtropical environment. *J. Appl. Meteor.,* **41,** 674–685.

Goddard, J. W. F., J. Tan, and M. Thurai, 1994: Technique for calibration of meteorological radars using differential phase. *Electron. Lett.,* **30,** 166–167.

Green, A. W., 1975: An approximation for shapes of large drops. *J. Appl. Meteor.,* **14**, 1578–1583.

Ryzhkov, A. V., and D. S. Zrnić, 1994: Precipitation observed in Oklahoma mesoscale systems with polarimetric radar. *J. Appl. Meteor.,* **33,** 455–464.

Smyth, T. J., T. M. Blackman, and A. J. Illingworth, 1999: Observations of oblate hail using dual polarization radar and implications for hail-detection schemes. *Q. J. Roy. Meteor. Soc.,* **125,** 993–1016.

Vivekanandan, J., G. Zhang, S. M. Ellis, D. Rajopadhyaya, and S. K. Avery, 2003: Radar reflectivity calibration using differential propagation phase measurement. *Radio Sci.,* **38,** doi:10.1029/2002RS002676.

Vivekanandan, J., D. S. Zrnić, S. M. Ellis, R. Oye, A. V. Ryzhkov, and J. Straka, 1999: Cloud microphysics retrieval using S-band dual-polarization measurements. *Bull. Amer. Meteor. Soc.,* **80,** 381–388.

Witt, A., M. D. Eilts, G. J. Stumpf, J. T. Johnson, E. D. Mitchell, and K. W. Thomas, 1998: An enhanced hail detection algorithm for the WSR-88D. *Wea. Forecasting,* **13,** 286–303.

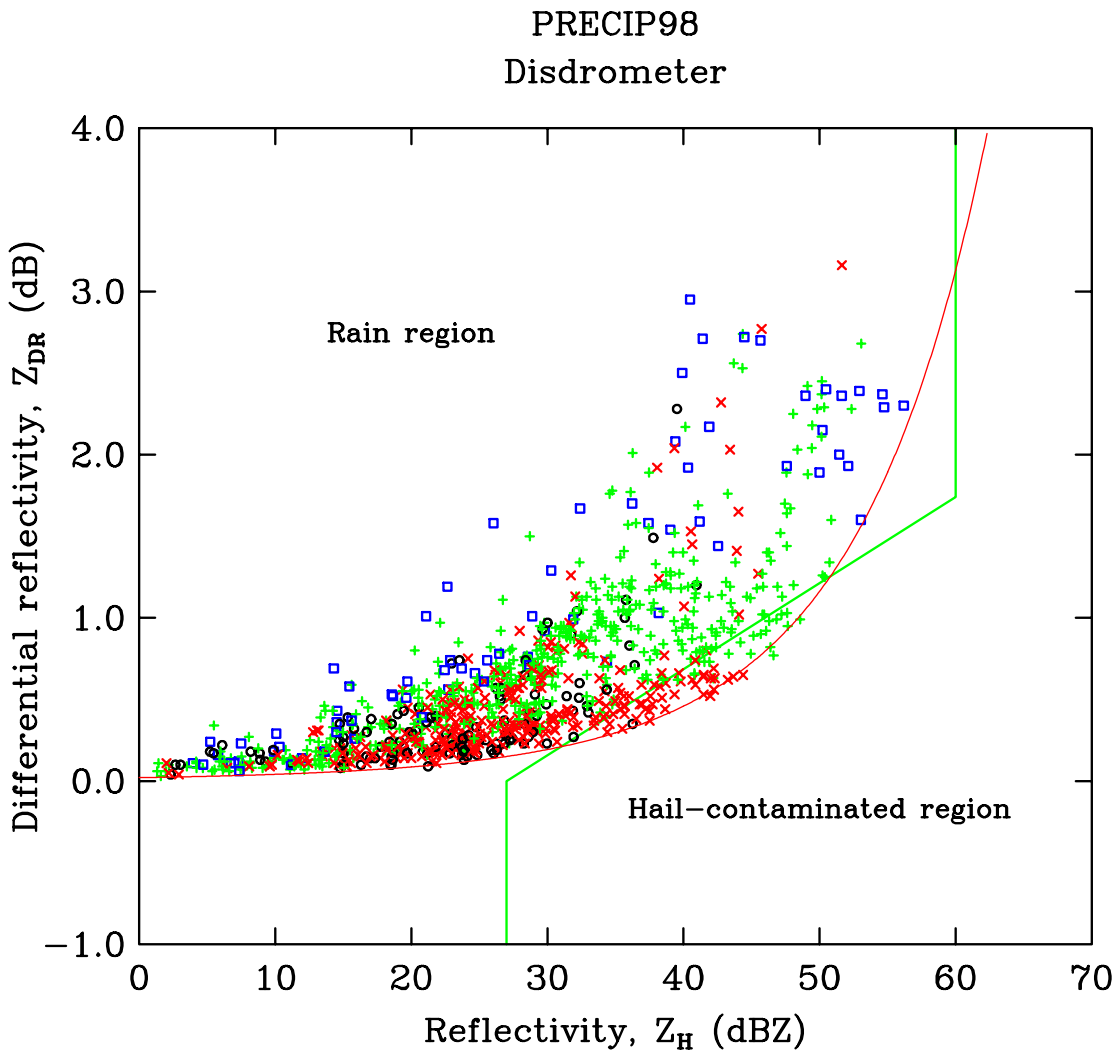

FIG. 1: Disdrometer calculations of radar reflectivity and differential reflectivity for Florida thunderstorms. The segmented green line is the rain–hail discrimination boundary of Aydin et al. (1986). The smooth curve [Eq. (2)] represents the limits of the rain measurements.

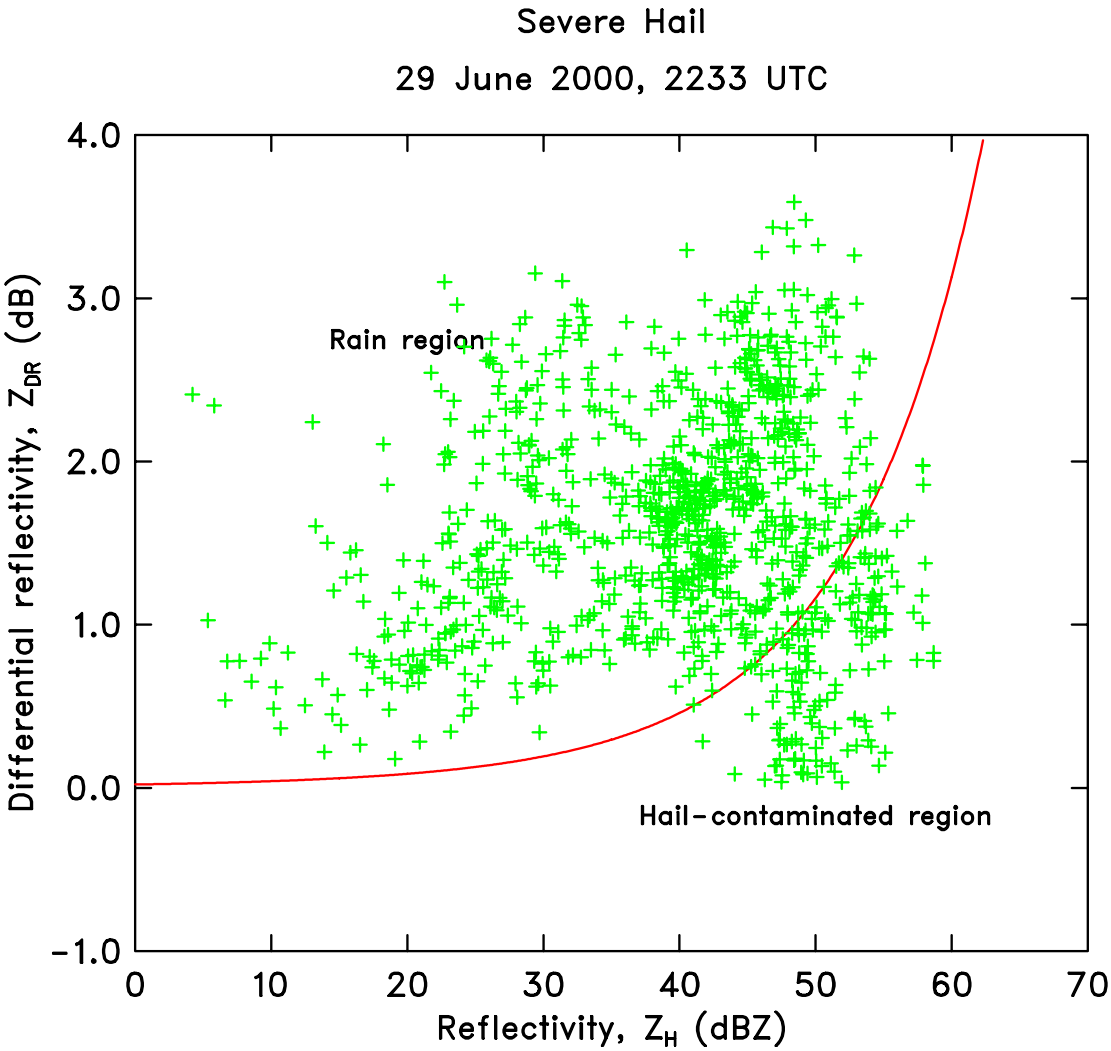

FIG. 2: Radar measurements of reflectivity and differential reflectivity for a severe hail storm that occurred in eastern Colorado.

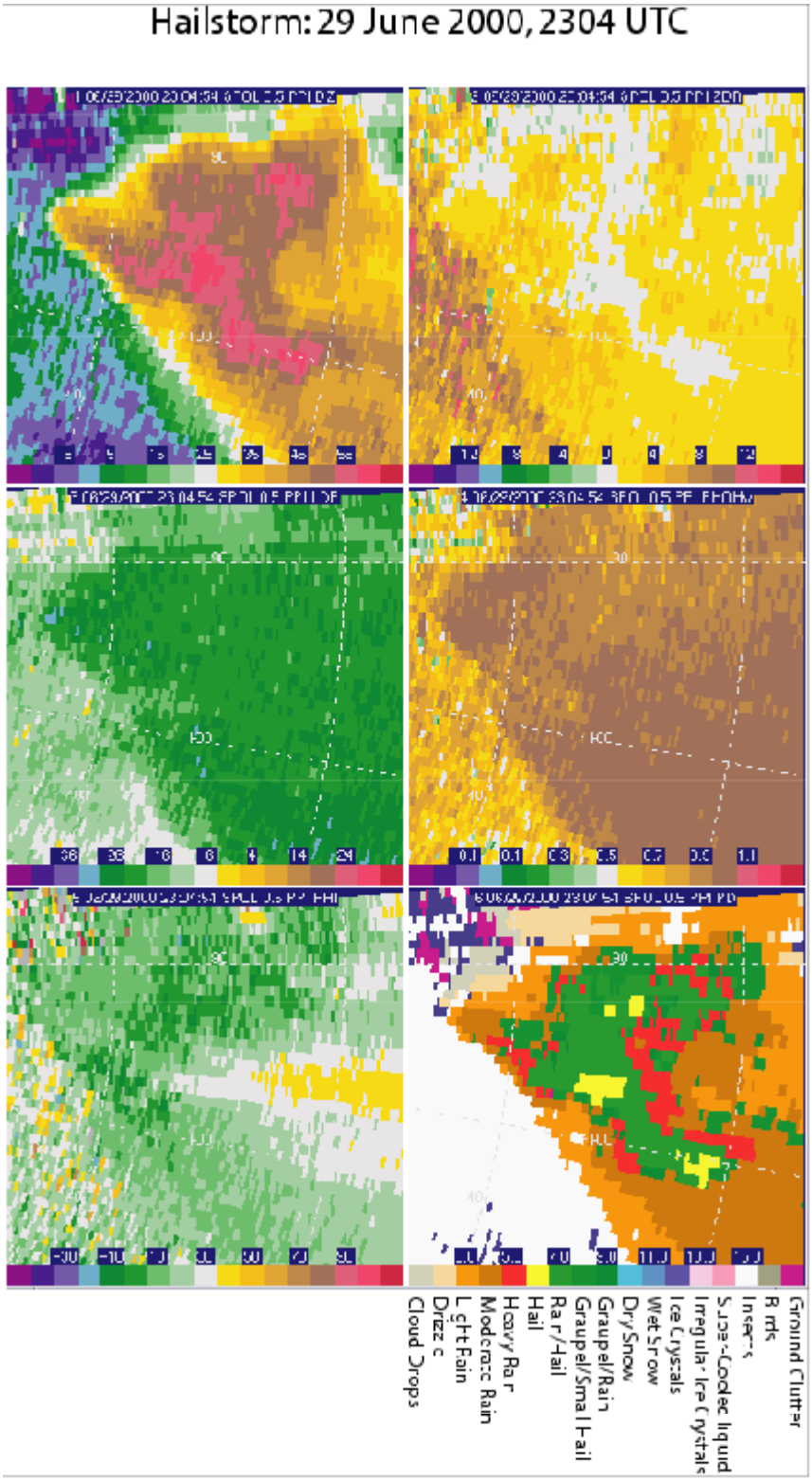

Fig. 3: Polarimetric radar measurements from NCAR's S-Pol radar and hydrometeor designations for the hailstorm in Fig.2.

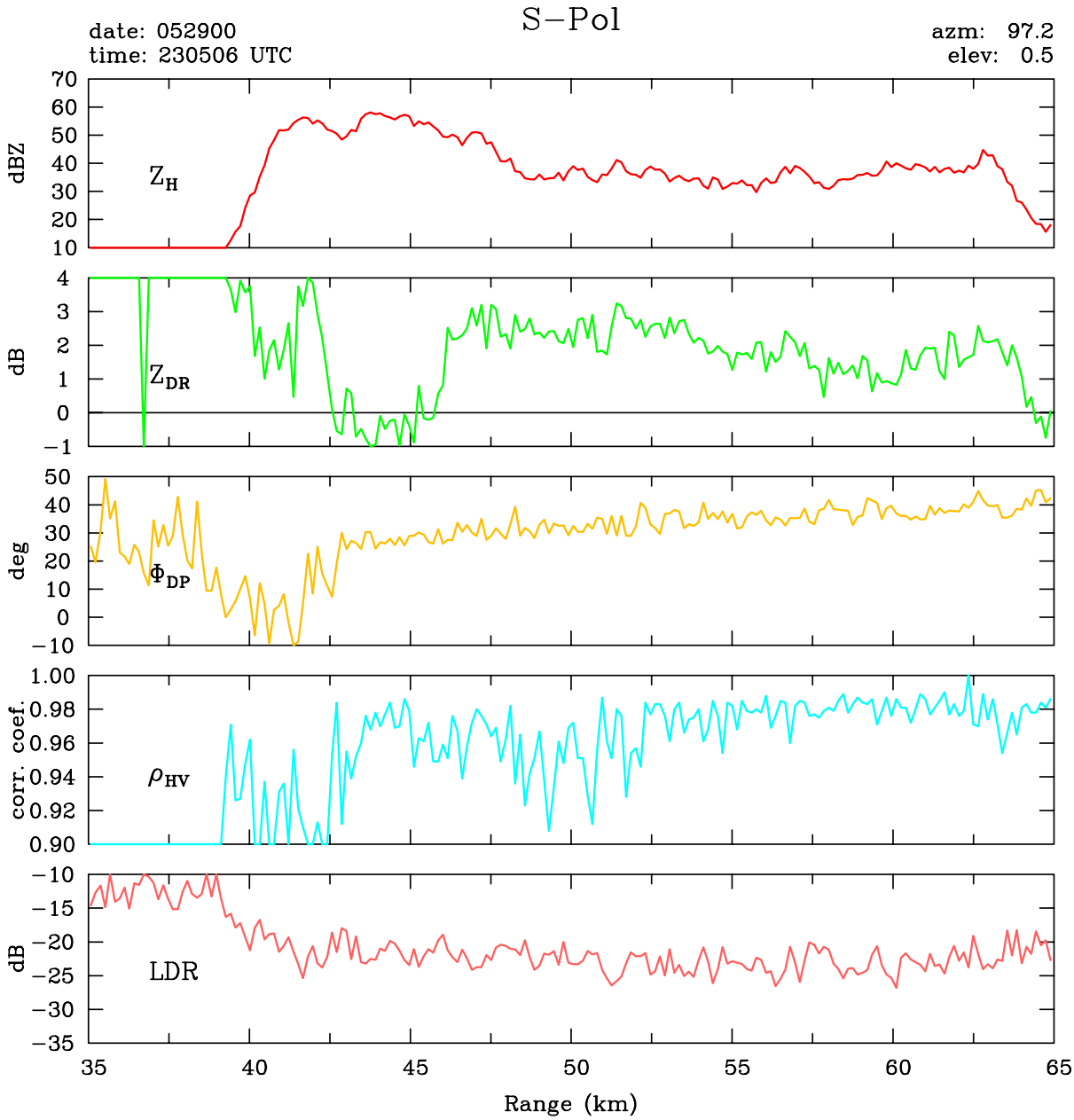

Fig. 4: Radial distributions of radar measurements at an azimuth of 97.2^o and an antenna elevation angle of 0.5^o for the hailstorm in Fig. 3.

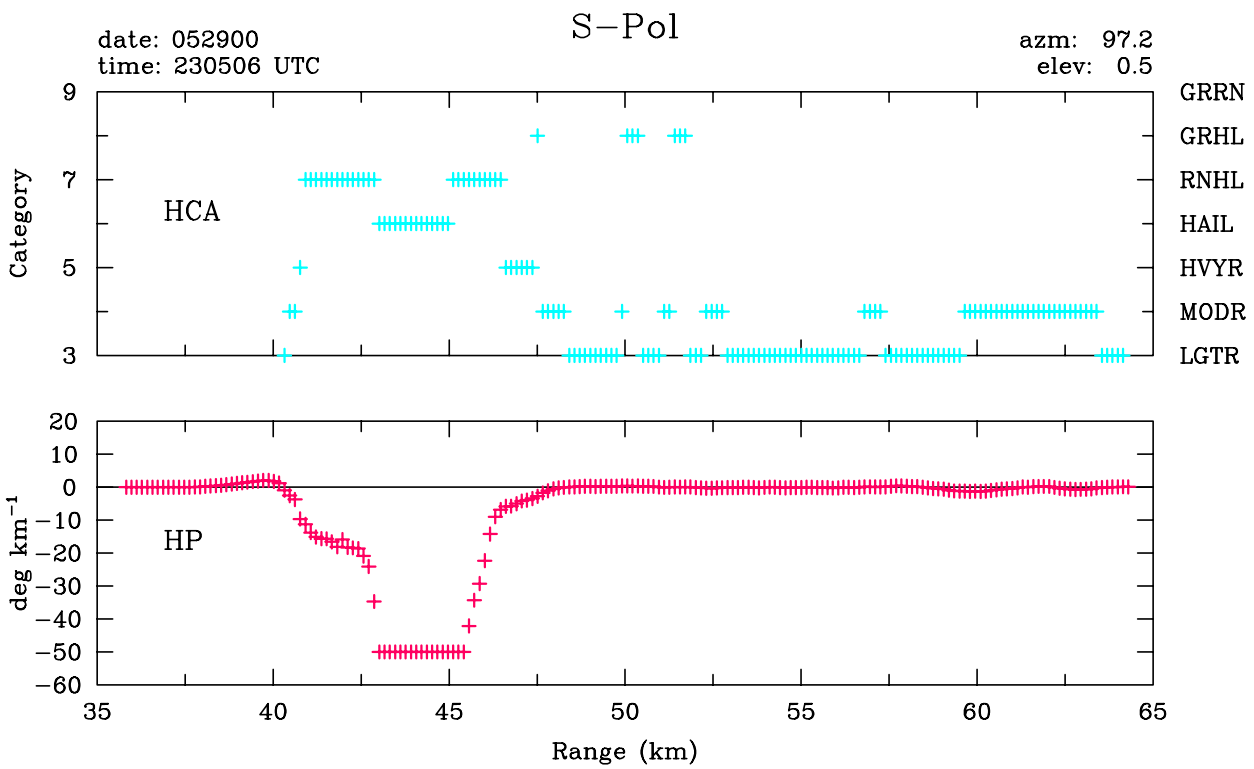

Fig. 5: The hydrometeor designations and distribution of HP for the ray in Fig. 4. Specific designations are for graupel–rain (GRRN), graupel–hail (GRHL), rain–hail (RNHL), hail, heavy rain (HVYR), moderate rain (MODR), and light rain (LGTR).

Appendix F

Improvements to the NCAR Freezing-Level Algorithm

Edward A. Brandes and Kyoko Ikeda

30 September 2003

Research Applications Program
National Center for Atmospheric Research
P. O. Box 3000
Boulder, CO 80307

1. Introduction

An automated method for estimating freezing-level heights would have several benefits. Alerts could be provided for those engaged in snow removal and aircraft deicing operations. Freezing-level heights are required for designating potential icing layers in storms and for verifying predictions of 0°C levels with numerical models. Knowing whether or not a melting layer exists is important to ascertain if radar-observed precipitation is rain or snow and for its quantification. The freezing level is also a component of polarimetric algorithms for general hydrometeor classification. If the 0°C level can be obtained from radar measurements, dependence on pilot reports and infrequent and widely-spaced atmospheric soundings would be lessened.

2. Background

Polarimetric radar measurements are particularly sensitive to the large wetted hydrometeors that characterize melting layers. Moreover, measurements of linear depolarization ratio (LDR) and co-polar correlation coefficient (ρ_{HV}) often provide definitive melting-layer signatures when hydrometeor types may preclude a signature in radar reflectivity (Z_H) measurements (e.g., when small graupel are present) or when hydrometeor advection alters the reflectivity profile. A freezing-level algorithm that combines the information from Z_H, LDR, and ρ_{HV} measurements has been under development (Brandes and Ikeda 2003). The algorithm finds the height at which the maximum melting-layer signatures appear in vertical profiles of these parameters and compares the profiles to an idealized melting-layer model in order to determine the goodness of fit. The freezing level is estimated with each parameter profile that matches the idealized profile. Final designations are based upon knowing the statistical relation between the depression of the maximum signature and the true 0°C level and weighing each parameter according to how well it matches the model profile. Typically, numerous estimates can be made in a region of widespread precipitation, and the variance among the estimates is a measure of the confidence that can be placed in the retrieval. The spatial distribution of the 0°C level is readily obtained which should be useful in frontal situations. Designations can generally be made to radar distances of 60 km or more and are believed accurate to within 100-200 m.

Early versions of the algorithm assumed that the offset (depression) of the maximum melting-layer signature for each parameter from the 0^oC level was fixed. Mean offsets had been found with soundings and in situ measurements from research aircraft. However, the depressions tend to increase as precipitation intensity increases.

3. Algorithm upgrade

To determine the relationship between the depression of the brightband reflectivity maximum from the 0^oC level and precipitation intensity, summary profiles of Fabry and Zawadzki (1995) were used. They constructed reflectivity profiles for various precipitation intensities from 350 h of measurements obtained with a vertically pointing radar having a height resolution of 15 m. It was assumed that the upper break point in the profiles occurred at the 0^oC level. Depressions for their profiles are plotted in Fig. 1. A least-squares fit gave

$$d_1 = 0.0886 - 0.000400 Z_H + 0.000112 Z_H^2 \qquad (1)$$

where d_1 in km is the depression of the reflectivity maximum from the estimated 0^oC level and Z_H is in dBZ. A sampling of depressions from field experiments conducted in Florida and Brazil, for which sounding data were available, is also shown. The unedited depressions agree quite well in the mean with the observations of Fabry and Zawadzki.

Depressions for LDR and ρ_{HV} melting-layer signature maxima are also functions of precipitation intensity. The depressions tend to be slightly larger than those for radar reflectivity. Unfortunately, a comparable dataset of high-resolution measurements at zenith for these parameters is not available. Instead, tilt measurements from NCAR's S-Pol radar were used to compute the depressions of LDR and ρ_{HV} melting-layer extremes from that for reflectivity. The distribution is shown in Fig. 2. A polynomial fit was applied to the data and the result added to (1). The derived relation is

$$d_{2,3} = 0.121 + 0.00445 Z_H + 0.000200 Z_H^2 \quad . \qquad (2)$$

The variables d_2 and d_3 are the depressions of LDR and ρ_{HV} melting-layer signature maxima from the 0^oC level, respectively. Expressions (1) and (2) are valid for brightband reflectivity maxima of 20 to 50 dBZ. Plans call for further testing of the freezing-level algorithm on an independent dataset to be collected during the upcoming WISP04 field program.

4. Application to a polarimetric WSR-88D

The freezing-level algorithm was applied to a dataset obtained with the WSR-88D (KOUN) modified by the National Severe Storms Laboratory for polarimetric measurements. The observations were from the trailing portions of a mesoscale convective system. Parameters available for analysis were radar reflectivity, differential reflectivity, co-polar correlation coefficient, and differential propagation phase. [The linear depolarization ratio is not available under the current proposed WSR-88D

upgrade.] Each tilt sequence consisted of 15 constant antenna elevation scans from 0 to 19.5^o. The measurement range resolution is 267 m.

Rather than construct vertical profiles of the measurements at specific locations on a rectangular grid, height profiles were made from the distribution of measurements along radial rays at antenna elevations $\geq 4.5^o$. All measurements depict the melting layer (e.g., Fig. 4). Figure 5 presents measurement profiles averaged over the azimuthal sector between 50 and 60°. Pronounced melting-layer signature maxima for reflectivity and co-polar correlation coefficient are clearly seen. Signatures for differential reflectivity and differential propagation phase are also evident. Generally, greater meteorological variability makes it more difficult to retrieve the 0°C level with the latter parameters. Hence, freezing-level designations in Fig. 3 are based on Z_H and ρ_{HV} measurements alone. Designations, shown only for elevation angles of 4.5, 6.5, 8.7, and 12.0, are plotted at the range where the radar beam intersected the freezing level. Unfortunately, in situ measurements corresponding to the analysis time are not available. The KOUN sounding for 0000 UTC detected the freezing level at 4.18 km. In summary, the algorithm should work well with measurements from a polarimetric WSR-88D.

Acknowledgment. The KOUN data used in this report were graciously provided by Alexander Ryzhkov of the National Severe Storms Laboratory.

REFERENCES

Brandes, E. A., and K. Ikeda, 2003: Freezing-level estimation with polarimetric radar. (In preparation)

Fabry, F., and I. Zawadzki, 1995: Long-term observations of the melting layer of precipitation and their interpretation. *J. Atmos. Sci.,* **52,** 838–851.

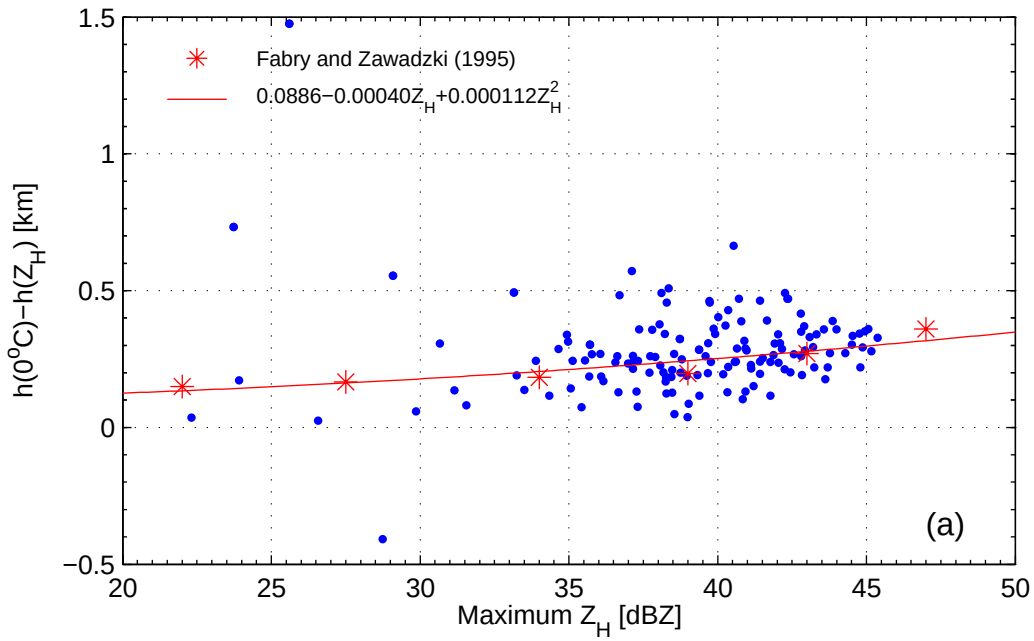

FIG.1: Height depressions of maximum brightband reflectivity from the 0°C level.

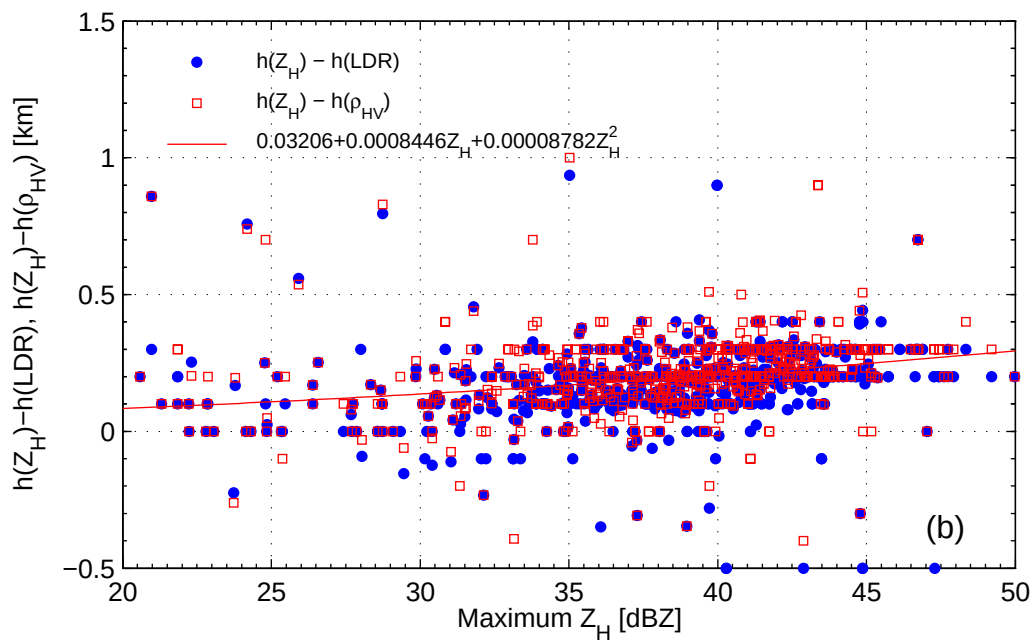

FIG. 2: Height depressions of maximum melting-layer signatures for linear depolarization ratio and co-polar correlation coefficient from the radar reflectivity brightband maximum.

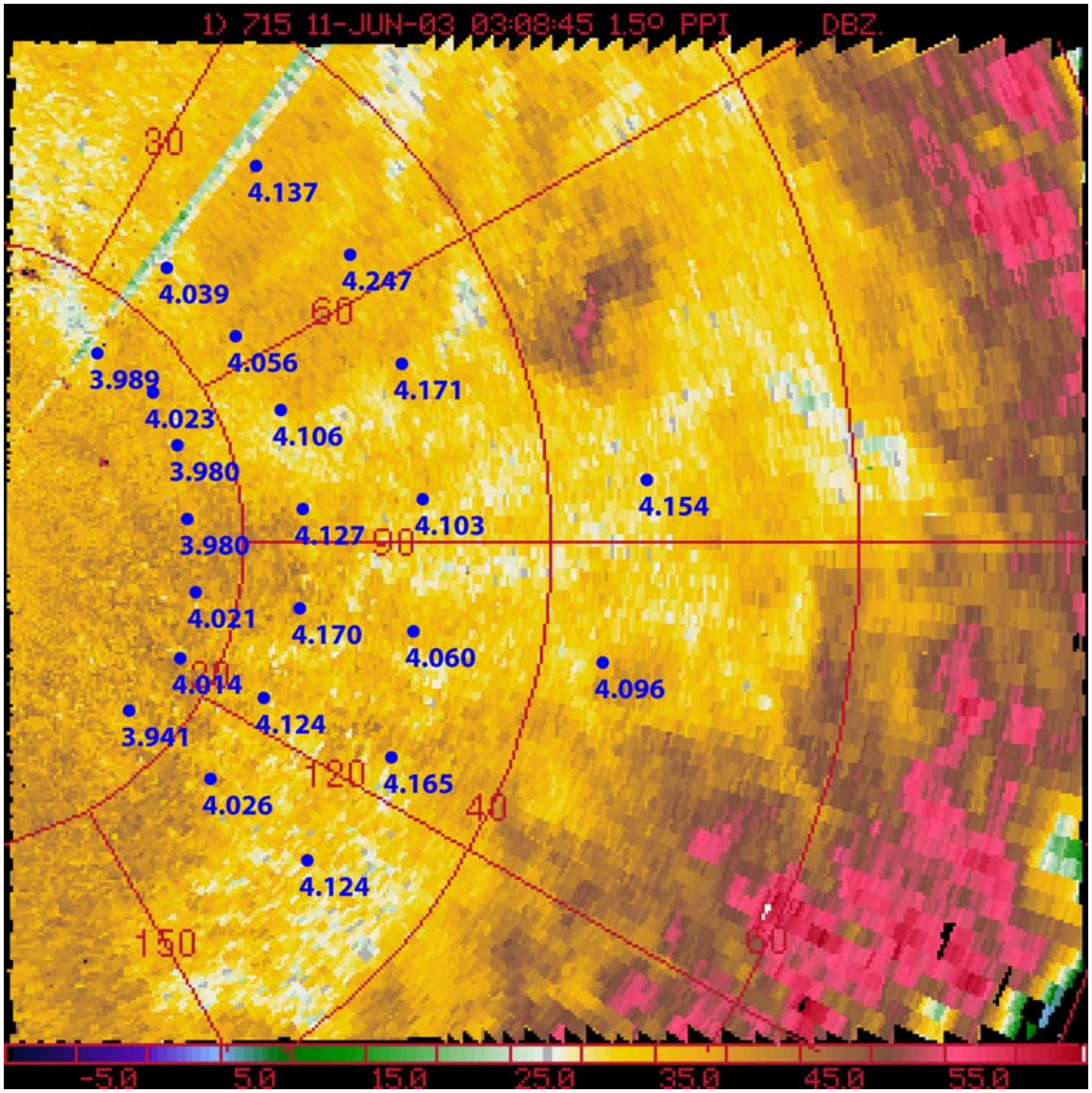

FIG. 3: Radar reflectivity measurements made from the NSSL polarimetric WSR-88D (KOUN) at 1.5^{o} antenna elevation for a scan beginning at 030845 UTC on 11 June 2003. Freezing-level detections based on radar reflectivity and co-polar correlation coefficient measurements are over laid.

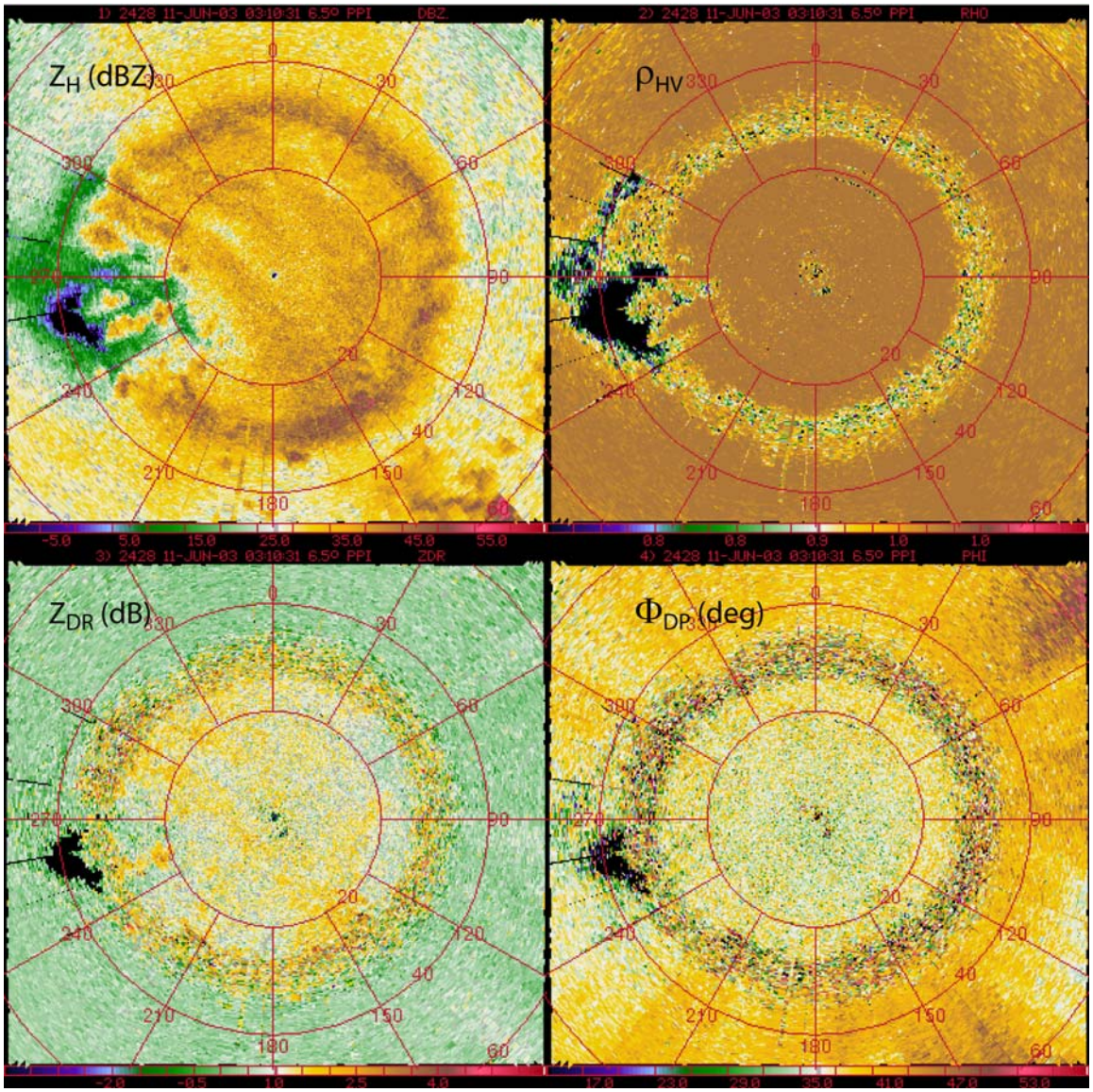

FIG. 4: The distribution of polarimetric measurements radar reflectivity (Z_H), correlation coefficient (ρ_{HV}), differential reflectivity (Z_{DR}), and differential propagation phase (Φ_{DP}) for the 6.5^o elevation scan beginning at 031031 UTC. Note the ring-like melting-layer signatures at a range of 30 km.

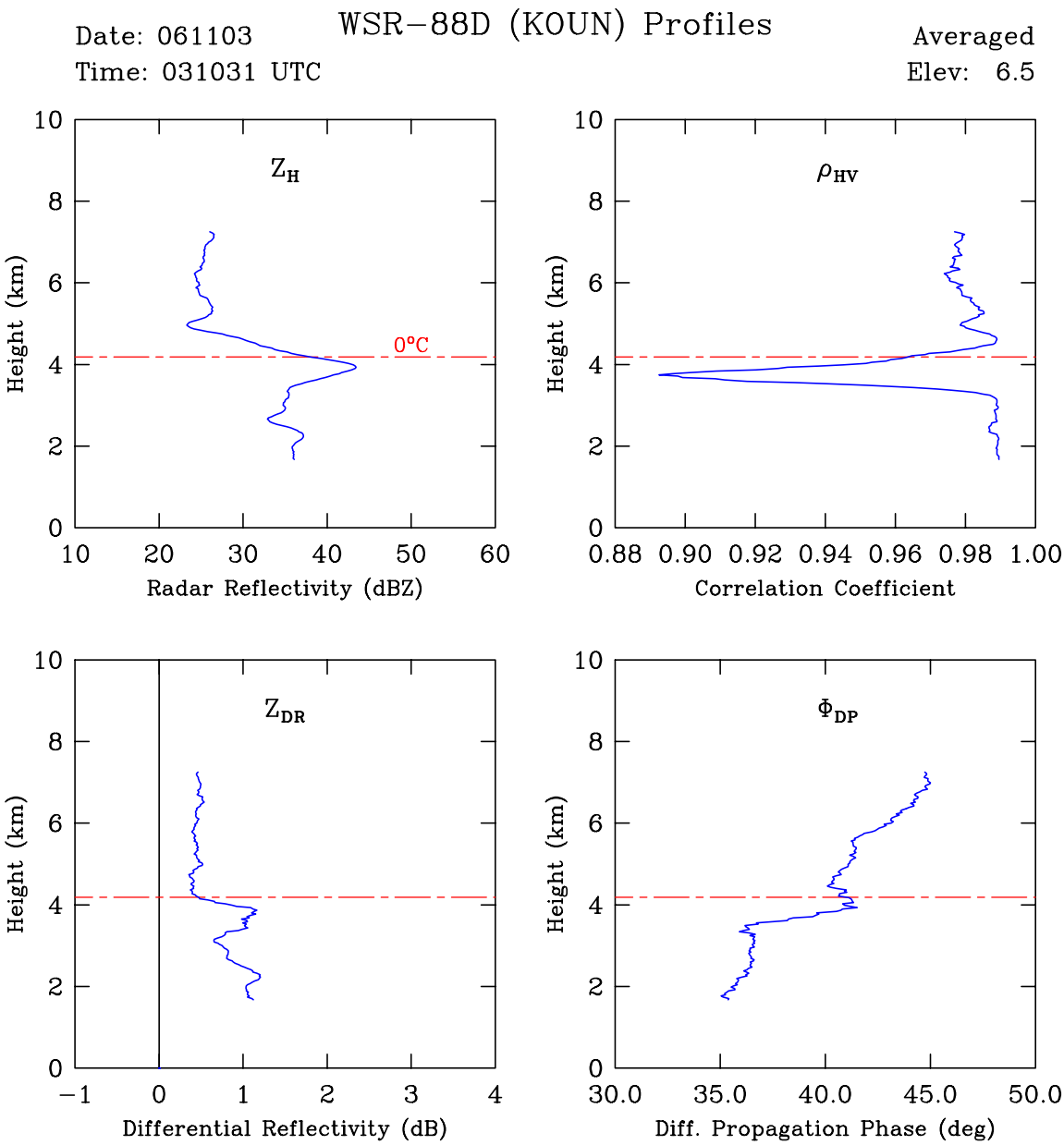

FIG. 5: Parameter profiles obtained with the NSSL polarimetric WSR-88D at 031031 UTC. The observed 0°C level, determined from the KOUN 0000 UTC sounding, was 4.18 km MSL (horizontal line). The algorithm estimated freezing-level height for the data shown is 4.25 km.

Multiscale Storm Identification and Forecast

V Lakshmanan[1], R. Rabin[2], V. DeBrunner[3*]

Abstract

We describe a recently developed hierarchical K-Means clustering method for weather images. that can be employed to identify storms at different scales. We describe an error-minimization technique to identify movement between successive frames of a sequence and show that we can use the K-Means clusters as the minimization kernel. A Kalman filter is used to provide smooth estimates of velocity at a pixel through time. Using this technique in combination with the K-Means clusters, we can identify storm motion at different scales and choose different scales to forecast based on the time scale of interest.

The motion estimator has been applied both to reflectivity data obtained from the National Weather Service Radar (WSR-88D) and to cloud-top infrared temperatures obtained from GOES satellites. We demonstrate results on both these sensors.

1. Introduction

The segmentation of weather imagery is a fundamental problem to automated weather analysis, as has been pointed out in Peak and Tag (1994); Lakshmanan et al. (2000); Johnson et al. (1998). There are numerous pattern recognition algorithms that have been developed on weather images, such as for rainfall estimates (Lai et al. 2000), and cloud classification (Lee et al. 1990), but segmentation techniques for weather images have not been addressed. This is true even of work that attempts to factor out weather-related effects in satellite imagery of land (Markus and Cavalieri 2000; Narasimhan and Nayar 2000).

In the meteorological community, the importance of multiscale segmentation has been often noted (Johnson et al. 1998; Wolfson et al. 1999; Lakshmanan et al. 2000). In (Peak and Tag 1994), the authors detail the difficulties that traditional segmentation algorithms have with satellite weather images because of the textural nature of clouds. As a result, a complex technique consisting of a sequence of fixed thresholds, followed by a neural network that decides how and when to prune or merge the resulting regions

*[1]Corresponding author address: lakshman@ou.edu. V Lakshmanan is at the Cooperative Institute of Mesoscale Meteorological Studies, U. Oklahoma (OU) and is also affiliated with NOAA/OAR/National Severe Storms Laboratory (NSSL). [2]Robert Rabin is with NSSL and the Cooperative Institute of Meteorological Satellite Studies (CIMSS) at the University of Wisconsin, Madison. [3]Victor DeBrunner is with the Department of Electrical and Computer Engineering at OU.

is proposed (Peak and Tag 1994). We show here that using a hierarchical technique in combination with a texture segmentation algorithm makes segmentation of satellite weather images possible such that even small cloud features can be identified.

The textural nature of weather imagery makes robust segmentation for storm tracking purposes very difficult. For storm tracking to be useful, the identification and tracking algorithm should be completely automated. The identification algorithm should not require training, i.e. the algorithm should not expect to see examples of all the "objects" it must identify. Storm "cells" (small scale features) should be capable of being identified. Because the notion of scale is natural in the storm tracking context, we would like to add the requirement that storms at various scales be identified, with their hierarchical structure intact. A multiscale tracking algorithm would be a significant improvement over current tracking schemes which concentrate either on small scales(e.g: (Johnson et al. 1998)) or on large scales (e.g: (Wolfson et al. 1999)).

In the United States, the operational way to identify storms from radar images involves the use of multiple thresholds and counting runs of values above a threshold along a radial. The centroids are then used as a proxy for the storms (Johnson et al. 1998) and tracked either on the basis of proximity to expected position or through a linear programming approach (Dixon 1994). The change in position is extrapolated.

Identification and tracking algorithms for satellite weather imagery have been implemented for mesoscale convective systems (Morel et al. 1997) – where the features of interest (storm anvils colder than 240K) are on the scale of about 10,000 km^2. Our goal, however, is to identify storm scale features, features on the scale of about 10 km^2.

Another technique (French et al. 1992) is to use neural networks to model input reflectivity fields as a set of nodes and to forecast reflectivity locations in the future based on the evolution of the nodes required to model successive frames. The problems with this technique are that it requires training a neural neural network in real-time, and that a trained neural network can not be used to forecast fields which have not been tracked.

A third technique is to use rectangular sub-grids and to find the maximum correlation within a search radius (Rinehart and Garvey 1978; Tuttle and Gall 1999). A modification of this technique is to pre-filter the data so as to track only the larger scales (Wolfson et al. 1999; Lakshmanan 2000). It is also possible to use sub-grids ranging in size from that of the entire image to small (say, 16km x 16km) grids, and to compute motion estimates at each of these scales. Smoothness criteria can be used to constrain these estimates at different scales.

Identifying, matching and extrapolating storm core locations is suitable for small scale storms. The large scale features and cross-correlation technique is suitable for longer forecasts, but with loss of detailed motion estimates. An assumption here is that the storms are of the scale of the sub-grid, not larger. The multiscale estimation is suitable also for large scale forecasts, but with less precise detailed motion estimates.

When used for advection, all the correlation techniques rely on reverse projection, so there needs to be wind speed at the spot where the storm is moving to. Methods rely on correlation estimates of rectangular templates also assume that all pixels within that rectangular template are moving together.

We use a hybrid approach where motion estimates are made for groups of storms (rather than for sub-grids of the image), but at various scales. The motion estimate

for a storm cell is the movement that minimizes the mean-absolute-error between the current frame and corresponding pixels in the previous frame, except that the template is not a rectangular sub-grid of the image, but is instead the actual shape of the storm cell.

Instead of simply matching storm cells across frames, motion estimates are made by finding the best match for the storm-template. Thus, the major steps in the technique are:

1. Find storms at different scales.
2. Estimate motion at the various scales.
3. Forecast for different periods using motion at different scales.

Because the motion estimates are made for storms, it is possible to interpolate between storm boundaries to obtain motion estimates at every part of the domain.

2. Hierarchical texture segmentation to identify storms

A K-Means clustering technique from Lakshmanan (2001); Lakshmanan et al. (2002) is used to identify components in vector fields. The technique provides nested partitions, i.e. the identified storms structures are strictly hierarchical. The technique works by clustering image values (reflectivity/infrared temperature, etc.) in the neighborhood of a pixel on two opposing criteria:

- Belong to same cluster as your neighbors.
- Belong to cluster whose mean is closest to your value.

Hierarchical segmentation is incorporated into the K-Means clustering technique by steadily relaxing inter-cluster distances.

The technique works by iteratively moving pixels between clusters minimizing

$$E(k) = \lambda d_m(k) + (1-\lambda) d_c(k) \qquad 0 \leq \lambda \leq 1 \tag{1}$$

where the distance in the measurement space is:

$$d_m(k) = \| \mu_k^n - T_{xy} \| \tag{2}$$

and the discontiguity measure is::

$$d_c(k) = \sum_{ij \epsilon N_{xy}} (1 - \delta(S_{ij}^n - k)) \tag{3}$$

A region growing algorithm is employed to build a set of connected regions, where each region consists of 8-connected pixels that belong to the same K-Means cluster. If a connected region is too small, then its cluster mean (the mean of the texture vectors at each pixel in the region) is compared to the cluster means of the adjoining regions and the small region is merged with the closest mean. The result of the K-Means

segmentation, region growing and region merge steps is the most detailed segmentation of the image.

The inter-cluster distances of all adjacent clusters (or regions) in the image are computed. A threshold is set such that half the pairs fall below this threshold. If a pair of clusters differs by less than this threshold, the clusters are merged and cluster means updated. This process is continued until no two adjacent regions are closer in cluster space than the threshold. When this process is complete, we have the next coarser scale of the segmentation. This process is repeated until no changes happen.

a. Weather Radar Images

Texture segmentation using Markov Random Field (MRF) models has been utilized to segment synthetic aperture radar (SAR) images, mainly because SAR images are characterized by a lot of speckle (Dong et al. 2001; Schroder et al. 1998; Smits and Dellepine 1999), a problem which is resolved through the use of neighborhood statistics. Another reason for using texture segmentation on SAR imagery is that the same MRF model used for segmentation can also be used for classifying the identified segments (Dong et al. 2001).

Texture segmentation has not been applied to weather radar data before. In weather radar data, especially in cases where there is significant precipitation, the problem of speckle does not arise except in the immediate vicinity of the radar. Hence, traditional texture segmentation provides no significant advantage. In fact, as shown in Figure 1e, even a scalar segmentation approach works quite well. What neither the scalar segmentation approaches, for example (Johnson et al. 1998), nor standard texture segmentation approaches (Blum and Rosenblat 1972; Hofmann et al. 1996; Ma and Manjunath 1997) can provide is a nested partition of identified segments. The watershed segmentation approach of Najman and Schmitt (1996) can provide a nested partition, but does not segment weather data well (See Figure 1f). As shown in Lakshmanan et al. (2002); Lakshmanan (2001), multiscale segmentation can be achieved by agglomerative K-Means clustering of texture vectors and slow relaxation of the allowed inter-cluster distance.

We wish to segment the reflectivity moment of radar elevation scans obtained from a Doppler Weather Service Radar (WSR-88D). The data have been mapped from polar coordinates into a Cartesian grid tangential to the earth's surface at the radar location where each pixel is a square area of one kilometer on each side. The pixel values, in dBZ, range from about $-7dBZ$ to about $64dBZ$, with the reflectivity values for some pixels missing. Missing values and all reflectivity values less than $0dBZ$ were thresholded to be $0dBZ$ before the segmentation process.

The radar elevations scans in this study were collected every 5-6 minutes. The weather surveillance radars used by the National Weather Service scan through thunderstorms starting at a low elevation angle, 0.5^o for Volume Coverage Pattern (VCP) 21, and after completing a full 360° azimuthal sweep, progressively increase the elevation angle until an upper limit is reached (19.5^o in VCP 21). See Figure 2 (Crum and Alberty 1993; Smith 1995). The data were remapped to a Cartesian plane and were then segmented using the K-Means clustering technique.

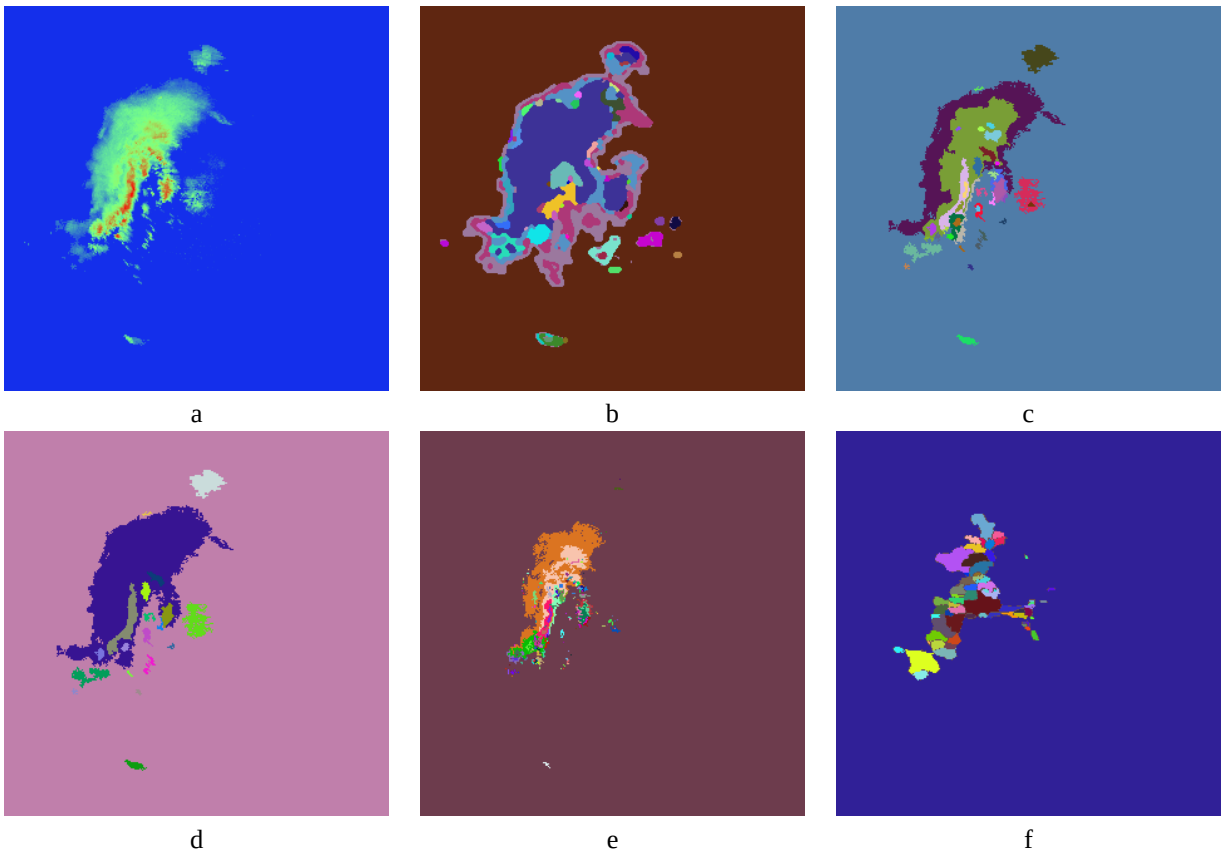

Figure 1: Segmenting a radar reflectivity image. (a) A radar reflectivity image, from Fort Worth May 5, 1995. (b) The result of segmenting the radar reflectivity image using the Markov Random Field (MRF) approach of Blum and Rosenblat (1972). (c) The result of segmenting the image using the method of this paper, tweaked to process the reflectivity range of interest. The most detailed scale is shown. (d) The next higher scale of segmentation using the method of this paper. (e) Simply separating the image into contiguous bands of $10dBZ$. (f) Using the watershed approach of Najman and Schmitt (1996).

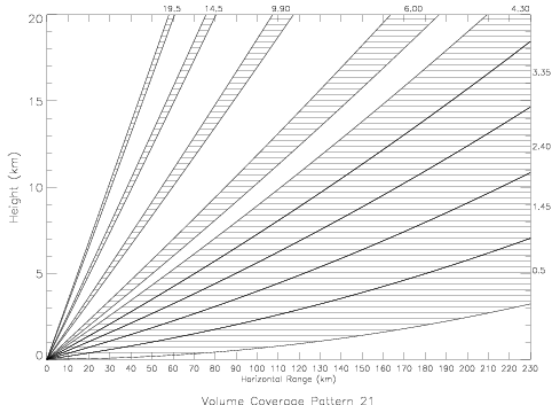

Figure 2: Volume Coverage Pattern (VCP) 21 of the WSR-88D, a weather surveillance radar used by the National Weather Service. The volume coverage is shown. The beamwidth is 0.95 degrees and there are 9 elevation scans in this VCP. Figure from Smith (1995).

b. Satellite Infrared Images

We demonstrate results of segmenting the infrared window channel (11μ) of GOES satellite imager data. The images are 200x300 with each pixel representing a $4km \times 4km$. The images are projected onto a plane tangential to the surface of the earth. The satellite data were collected over the continental United States using GOES-11 on March 29, 1998. The pixel values were also mapped from radiance values to equivalent black body temperature in degrees Kelvin before the segmentation. Images of the sequence are available at eight minute intervals.

The sequence of satellite images captures a day of significant thunderstorm activity. Several thunderstorms grow and decay during the day. The temperatures and sizes of the cloud tops in the images show relate in a bulk sense to the magnitude and extent of clusters of storm updrafts within the anvil clouds. Segmentation of this sequence should be able to consistently identify the thunderstorm cloud tops in the images. Ideally, when cloud tops appear to split or merge, the corresponding segmented regions should do the same. A very important requirement is that small changes in the storm structure should be reflected as small changes in the segmented region corresponding to the storm.

Studies (Browning 1979; Bellon and Zawadzki 1994) have shown that a single storm cell grows and decays in under an hour. Therefore, a storm cell can be expected to stay for no more than seven frames of the satellite sequence. However, a line of thunderstorms within which these cells crop up can be expected (Browning 1979) to persist for up to six hours. Also, the cloud top (anvil) may persist after the cell on radar decays. Therefore, the segmentation should lend itself to segmenting regions corresponding to larger scale features while identifying small scale features that are contained within the large scale feature but have shorter life-times.

A single infrared image was segmented using various segmentation methods in the literature. The results are shown in Figure 3c and d. The results of segmentation using the other approaches (Figure 3b,e and f. are poor in terms of the scale of the resulting regions. This is not surprising because the infrared satellite weather imagery has several characteristics that make it hard to segment: very low dynamic range (from about 225K to 240K) for the regions of interest, poor resolution as compared to the scale of the phenomena of interest, and high pixel value variance, even in the absence of edges. It is instructive to compare the poor performance of these algorithms on the satellite image (see Figure 3) with the performance of the same algorithms on radar reflectivity images in Section a.

The poor spatial resolution of the satellite image affects our algorithm also, in the scale of features that we can detect. Although we can detect features as small as 10 pixels in the image, this translates to about 40 km^2, a mid-size storm cell (although significantly more detailed than what could be obtained using earlier approaches). The pruning threshold of 10 pixels was set in the algorithm so that any statistics collected are somewhat reliable. One possible way to relax this threshold is by creating a pseudo-high resolution form of the original image, thus getting less square kilometers in the 10-pixel threshold. Unfortunately, on satellite weather images, even a pseudo-high resolution technique (Yao 1999) introduces unacceptable smoothing (Lakshmanan 2001), resulting in worse performance. A second possibility, one that we have not yet looked into because of the prohibitive cost for a continuously running system, is to obtain weather satellite data that has higher spatial resolution. A third possibility is to use the multi-channel nature of satellite weather information to form the pixel representation (instead of using a texture vector based on neighborhood statistics).

Instead of using only texture measurements from only the infrared channel, we used texture measurements (mean and variance) computed on four channels corresponding to 3.9, 6.7, 11 and 12 microns (near infrared, water vapor, window and "dirty window" respectively (Menzel and Purdom 1994)). Since every pixel of the segmented output actually corresponds to four relatively independent measurements (rather than just one), the minimum pruning size in the algorithm can be reduced from about 10 pixels to about 3. The result of using multi-channel information and a lower size threshold is shown in Figure 5 where it is compared to the segmented result if only the 11 micron image had been used.

Notice that the result of segmenting using all four channels (Figure 5f) has smaller regions than the result that uses only the infrared window channel. It is not clear, however, how significant these smaller features are in the context of thunderstorms.

3. Motion Estimation

Once the storms have been identified from the images, these storms are used as a template and the movement that minimizes the absolute-error between two frames is computed. For radar images, we used consecutive (5-6 min) volume scans.

Motion estimation is done by moving a template of the identified region at the appropriate scale around in the previous image. A matrix of mean absolute error at the different positions is obtained as shown in Figure 6

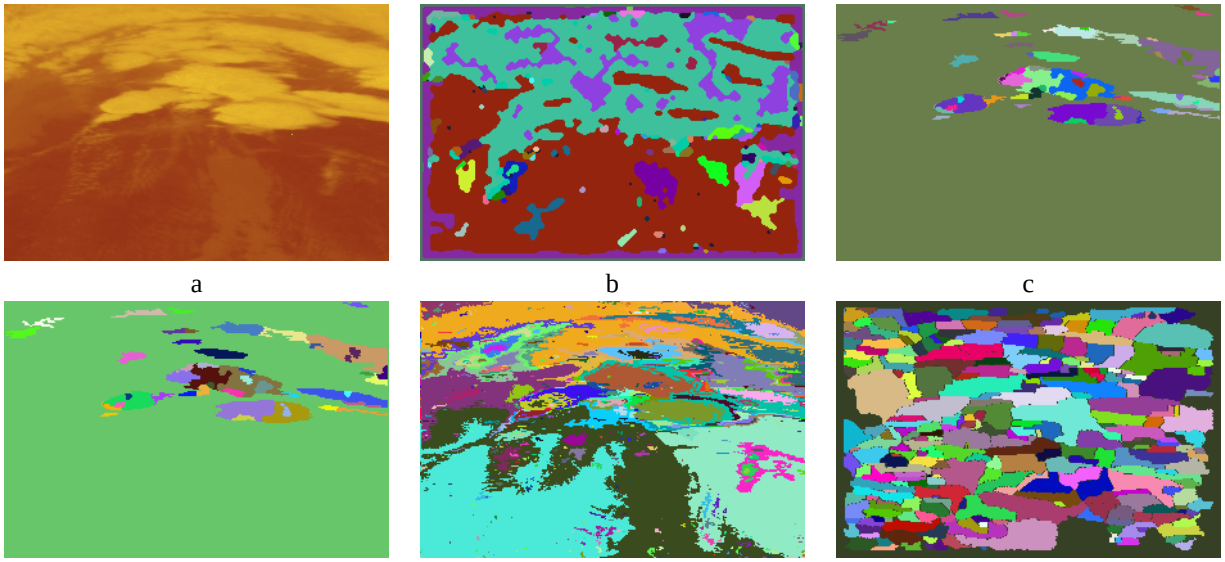

Figure 3: Segmenting an infrared satellite weather image. (a) The infrared image being segmented. Notice the various storms at the top of the image. The darker areas in the bottom correspond to ground. (b) The result of segmenting the image using the Markov Random Field (MRF) approach of Blum and Rosenblat (1972). There is no detail – it is effectively a binary segmentation. (c) The result of segmenting the image using the method of this paper (the most detailed scale). Notice the fine detail within the clouds. (d) The next higher scale of segmentation using the method of this paper. The strong storm cells being significantly colder are retained – the large cloud masses are merged. (e) Simply separating the image into contiguous bands of $1 Kelvin$. There is a lot of detail, but no organization. This is what you get using hierarchical thresholds. (f) Using the watershed segmentation approach of Najman and Schmitt (1996). Because of the textural nature of the data, the watershed algorithm has very poor performance.

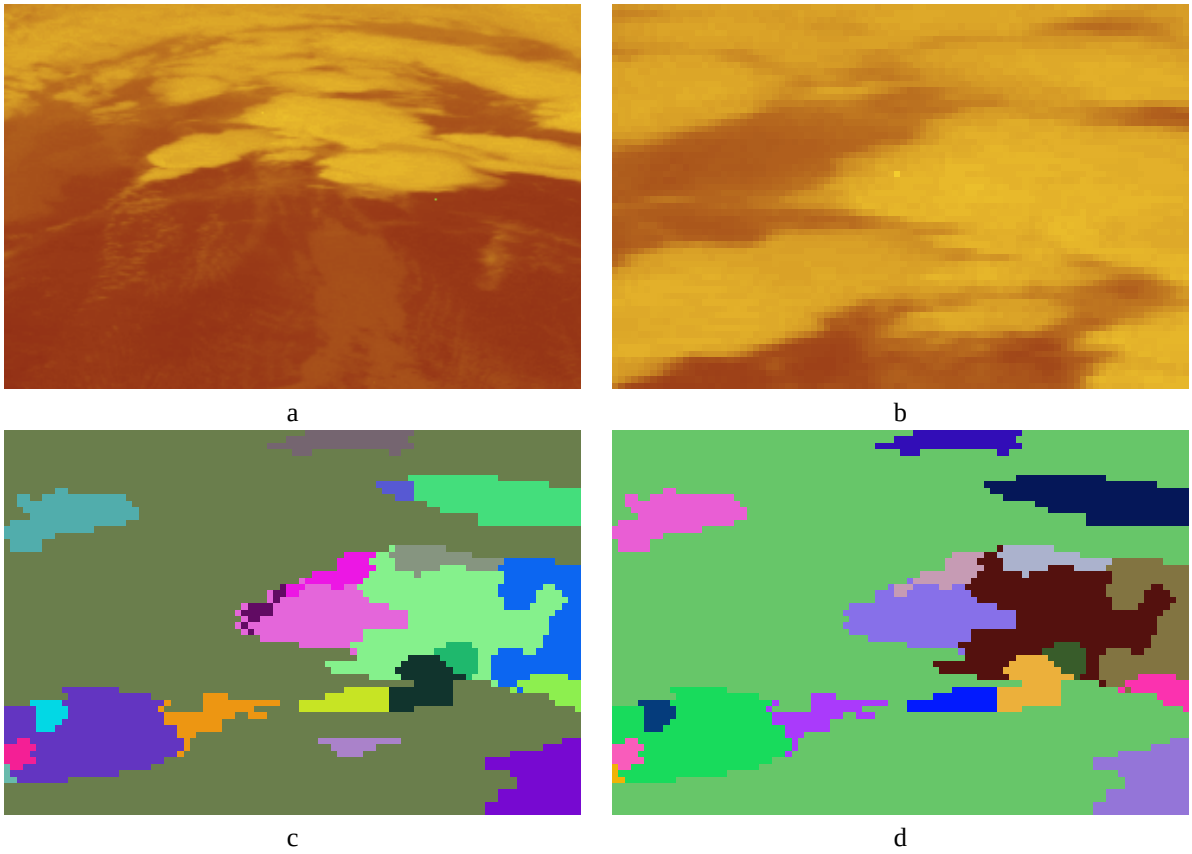

Figure 4: A close-in look at the results shown in Figure 3.. (a) The infrared image being segmented (same as Figure 3a). (b) A close-in look at the input satellite infrared image of (a). (c) A close-in look at the result of segmenting the image using the method of this paper (the most detailed scale). Notice the fine detail within the clouds. (d) A close-in look at the next higher scale of segmentation using the method of this paper.

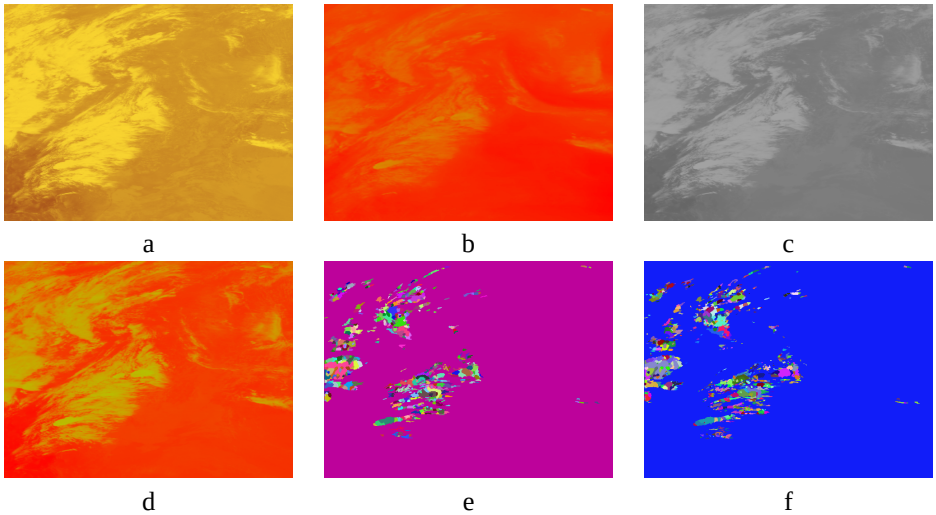

Figure 5: Using multi-channel satellite data for segmentation. (a) 3.9 micron infrared (b) 6.7 micron water vapor (c) 11 micron window (d) 12 micron dirty window channels of data. (e) Most detailed segmentation using only the 11 micron image (f) Most detailed segmentation using all four channels. The segmentation is more detailed than the segmentation that was achieved in (e), but whether these extra details are useful is yet to be determined.

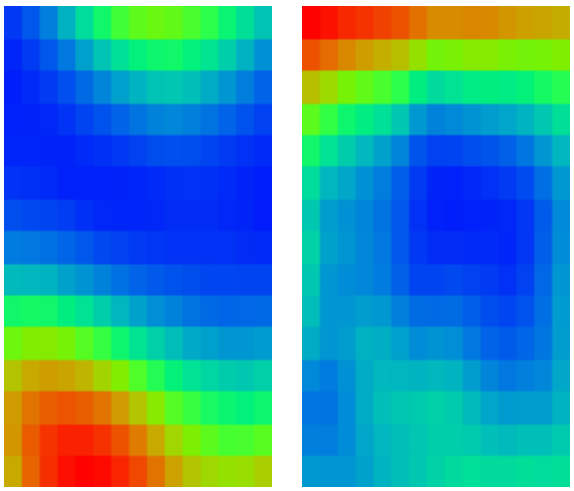

Figure 6: Matrix of mean absolute error by position. Larger errors are “warmer”. Two different locations are shown.

Instead of simply finding the absolute minimum, a smoother minimum of the absolute error field is sought. The field of absolute errors is minimized by weighting each value by how much it differs from the absolute minimum and finding the centroid.

For each storm template, we also get a growth/decay estimate. This is based on how much the average value inside the template changes based on the template at the best match.

Given the motion estimates for each of the regions in the image, the motion estimate at each pixel is determined through interpolation. At the pixel xy, the motion estimate u_{xy} is given by

$$u_{xy} = \frac{\Sigma_i u_i w_{ixy}}{\Sigma_i w_{ixy}} \tag{4}$$

where u_i is the motion estimate for the ith region and the weight of the this estimate at the point xy is given by:

$$w_{ixy} = \frac{N_i}{\| \, xy - c_i \, \|^2} \tag{5}$$

N_i is the number of pixels in the ith region, c_i its centroid and $\|$ denotes the Euclidean distance between the two points.

This motion estimate is for the pair of frames that were used in the comparison. We do temporal smoothing of these estimates by running a Kalman filter Kalman (1960) at each pixel of the motion estimate. The Kalman estimator is built around a constant acceleration model with the standard Kalman update equations Brown and Hwang (1997).

a. Short-term Forecast

The forecast of the fields is done based on the motion estimates, growth and decay heuristic and the current data. Forecasts can be made on fields other than the tracked field. For example, motion estimates can be derived from VIL and applied to radar reflectivity and probability fields of lightning and hail.

The forecast is done by first project data forward in time to a spatial location given by the motion estimate at their current location and the elapsed time. Locations not filled by this forward projection are filled by interpolating using an inverse square-distance metric of nearby filled locations.

The skill of this technique is quantititavely measured by comparing, for example, the 30 minute forecast against the actual field closest to 30 minutes ahead. For the mean absolute error results, the actual values are used. For the critical success index (CSI) results, the best match with a 5x5 window is used. Comparisions are made with a plain persistence, and with motion estimates derived by minimizing the correlation of a 5x5 template between the frames.

Results over a 60minute period on reflectivity from the Fort Worth radar on April 201995 are shown in Figures 7 and 8.

The CSI and MAE measure different aspects of the forecast accuracy. The MAE takes into account actual reflectivity values and is, therefore, a measure of how good the growth-and-decay aspect is. The CSI is a measure of predicting storm location. We are good at predicting storm location, but not so good at growth/decay.

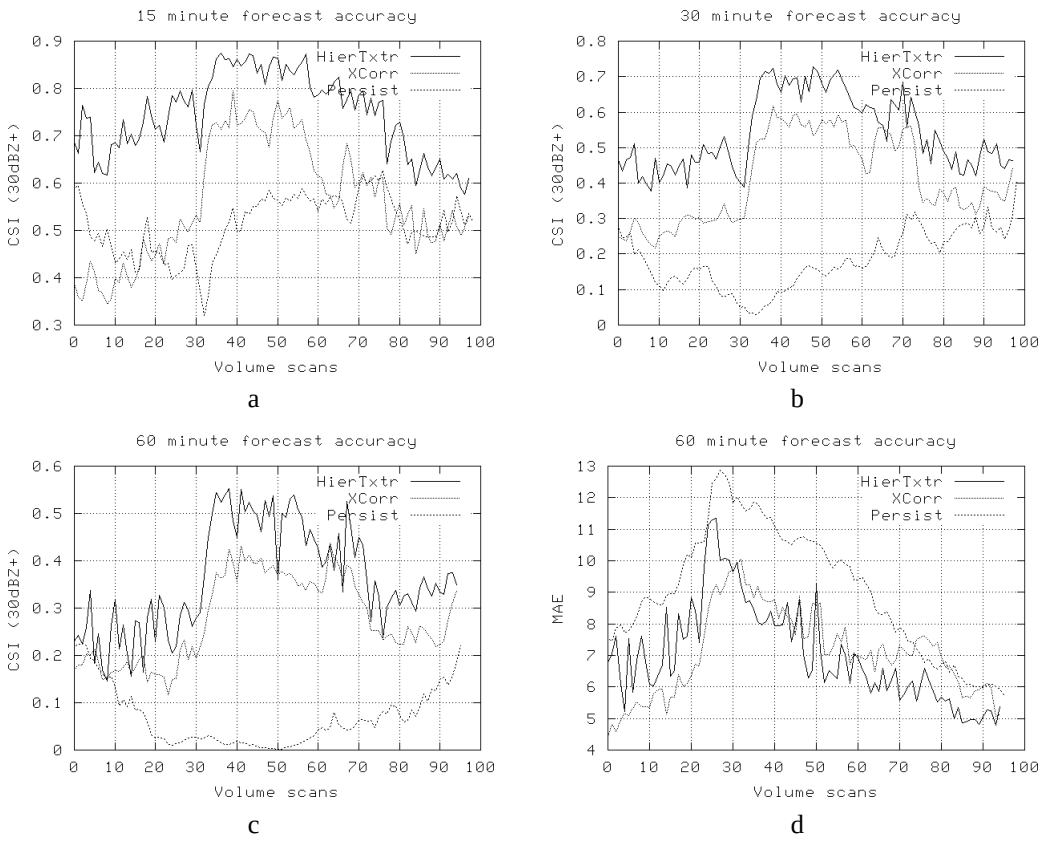

Figure 7: Skill at forecasting a radar reflectivity field compared to a persistence forecast and to a local correlation approach. (a) Values 30dBZ and above for 15 minutes (b) Values 30dBZ and above for 30 minutes (c) Values 30dBZ and above for 60 minutes (d) Mean absolute error in 60 minute forecast

A forecast based on satellite infrared temperature is shown in Figure 9. The data are taken from GOES-12 imagery on Oct. 9, 2001. The data provided were 100 seconds apart; we used every 4th frame of the sequence to compute motion estimates. Work to compute skill scores on satellite data is underway.

A version of this paper with color illustrations is available online at

`http://www.cimms.ou.edu/~lakshman/Papers/kmeans_motion.pdf`

4. Conclusions

It is possible to use a K-Means clustering to provide hierarchical identification of storms. The clusters can then be used to estimate the movement of the storm cores. A forecast that projects the movement of the storm cores linearly possesses some skill.

5. Acknowledgements

Funding for this research was provided under NOAA-OU Cooperative Agreement NA17RJ1227, FAA Phased Array Research MOU, and the National Science Foundation Grants 9982299 and 0205628.

References

Bellon, A. and I. Zawadzki: 1994, Forecasting of hourly accumulations of precipitation by optimal extrapolation of radar maps. *Journal of Hydrology*, **157**, 211–233.

Blum, J. and J. Rosenblat: 1972, *Probability and Statistics*. W.B. Saunders Company, 549 pp.

Brown, R. and P. Hwang: 1997, *Introduction to Random Signals and Applied Kalman Filtering*. John Wiley and Sons.

Browning, K.: 1979, The FRONTIERS plan: A strategy for using radar and satellite imagery for very-short-range precipitation forecasting. *The Meteorological Magazine*, **108**, 161–184.

Crum, T. and R. Alberty: 1993, The WSR-88D and the WSR-88D operational support facility. *Bulletin of the American Meteorological Society*, **74**, 1669–1687.

Dixon, M.: 1994, *Automated Storm Identification, Tracking and Forecasting – A Radar-Based Method*. Ph.D. thesis, University of Colorado and National Center for Atmospheric Research.

Dong, Y., A. Milne, and B. Forster: 2001, Segmentation and classification of vegetated areas using polarimetric sar image data. *IEEE Trans. Geosci. Remote Sensing*, **39**, 321–329.

French, M., W. Krajewski, and R. Cuykendall: 1992, Rainfall forecasting in space and time using a neural network. *J. Hydrology*, **137**, 1–31.

Hofmann, T., J. Puzicha, and J. Buhmann: 1996, A deterministic annealing framework for unsupervised texture segmentation. Technical Report IAI-TR-96-2, Institut fr Informatik III, U. Bonn, http://www-dbv.cs.uni-bonn.de/image/example4.html.

Johnson, J., P. Mackeen, A. Witt, E. Mitchell, G. Stumpf, M. Eilts, and K. Thomas: 1998, The storm cell identification and tracking algorithm: An enhanced WSR-88D algorithm. *Weather and Forecasting*, **13**, 263–276.

Kalman, R.: 1960, A new approach to linear filtering and prediction problems. *Trans. ASME – J. Basic Engr.*, 35–45.

Lai, E., P. Li, C. Chan, M. Chu, and W. Wong: 2000, Pattern recognition of radar echoes for short-range rainfall forecast. *15th Intl. Conf. on Pattern Recog.*, IEEE, volume 4, 299–302.

Lakshmanan, V.: 2000, Speeding up a large scale filter. *Journal of Oceanographic and Atmospheric Technology*, **17**, 468–473.

— 2001, *A Heirarchical, Multiscale Texture Segmentation Algorithm for Real-World Scenes*. Ph.D. thesis, U. Oklahoma, Norman, OK.

Lakshmanan, V., V. DeBrunner, and R. Rabin: 2002, Nested partitions using texture segmentation. *Southwest Symposium on Image Analysis and Interpretation*, IEEE, Santa Fe, New Mexico.

Lakshmanan, V., R. Rabin, and V. DeBrunner: 2000, Identifying and tracking storms in satellite images. *Second Artificial Intelligence Conference*, American Meteorological Society, Long Beach, CA, 90–95.

Lee, J., R. Weger, S. Sengupta, and R. Welch: 1990, A neural network approach to cloud classification. *IEEE Trans. on Geoscience and Remote Sensing*, **28**, 846–855.

Ma, W. and B. Manjunath: 1997, Edge flow: a framework of boundary detection and image segmentation. *Proc. IEEE International Conference on Computer Vision and Pattern Recognition*, San Juan, Puerto Rico, 744–749.

Markus, T. and D. Cavalieri: 2000, An enhancement of the NASA team sea ice algorithm. *IEEE Trans. on Geoscience and Remote Sensing*, **38**, 1387–1398.

Menzel, P. and J. Purdom: 1994, The first of a new generation of geostationary operational environmental satellites. *Bull. Amer. Meteo. Soc.*, **75**, 757–782.

Morel, C., F. Orain, and S. Senesi: 1997, Automated detection and characterization of MCS using the meteosat infrared channel. *Proc. Meteo. Satellite Data Users Conf.*, Brussels, 213–220.

Najman, L. and M. Schmitt: 1996, Geodesic saliency of watershed contours and hierarchical segmentation. *IEEE Trans. Patt. Anal. and Mach. Intell.*, **18**, 1163–1173.

Narasimhan, S. and S. Nayar: 2000, Chromatic framework for vision in bad weather. *IEEE Conf. on Comp. Vision and Patt. Recog.*, IEEE, volume 1, 598–605.

Peak, J. and P. Tag: 1994, Segmentation of satellite weather imagery using hierarchical thresholding and neural networks. *Journal of Applied Meteorology*, **33**, 605–616.

Rinehart, R. and E. Garvey: 1978, Three-dimensional storm motion detection by conventional weather radar. *Nature*, **273**, 287–289.

Schroder, M., H. Rehrauer, K. Seidel, and M. Dutcu: 1998, Spatial information retrieval from remote-sensing images – part ii: Gibbs-markov random fields. *IEEE Trans. Geosci. Remote Sensing*, **36**, 1446–1455.

Smith, T.: 1995, Visualization of WSR-88D data in 3d using application visualization software. *14th Conf. on Weather Forecasting*.

Smits, P. and S. Dellepine: 1999, Discontinuity-adaptive markov random field model for the segmetnation of intensity sar images. *IEEE Trans. Geosci. Remote Sensing*, **37**, 627–631.

Tuttle, J. and R. Gall: 1999, A single-radar technique for estimating the winds in tropical cyclones. *Bull. Amer. Met. Soc.*, **80**.

Wolfson, M., B. Forman, R. Hallowell, and M. Moore: 1999, The growth and decay storm tracker. *8th Conference on Aviation*, Amer. Meteor. Soc., Dallas, TX, 58–62.

Yao, M.: 1999, *Model-Based Methods for Image Interpolation and Enhancement That Retain Edge Information*. Ph.D. thesis, U. Oklahoma.

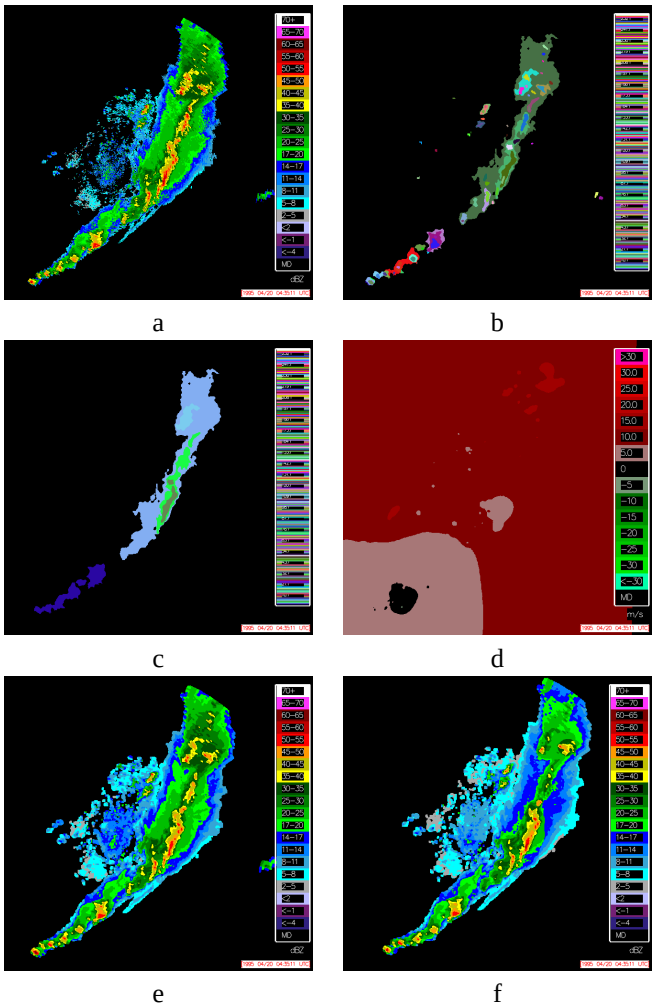

Figure 8: (a) Reflectivity data from KFWS, April 1995. (b) Most detailed scale of segmentation, used in forecasting under 30 minutes. (c) Coarse segmentation, used in forecasting more than 90 minutes. (d) Motion estimate (red is eastward motion) (e) 15min forecast (f) 60min forecast

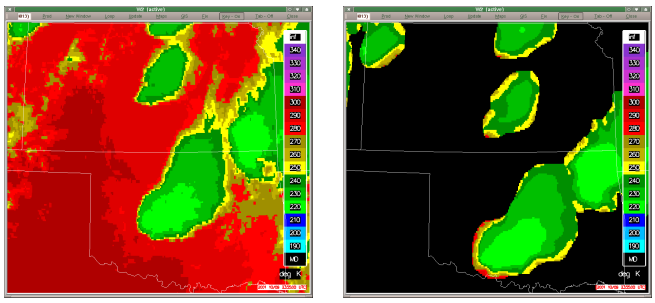

Figure 9: The original (left) and a 30 minute forecast of infrared temperature from Oct. 9, 2001.

Quality Control of Weather Radar Data Using Texture Features and a Neural Network

V Lakshmanan[1], Kurt Hondl[2], Gregory Stumpf[1], Travis Smith[1]

Abstract— **Weather radar data is subject to many contaminants, mainly due to non-precipitating targets (such as insects and wind-borne particles) and due to anamalous propagation (AP) or ground clutter. Although weather forecasters can usually identify, and account for, the presence of such contamination, automated weather algorithms are affected drastically. We discuss several local texture features and image processing steps that can be used to discriminate some of these types of contaminants. None of these features by themselves can discriminate between precipitating and non-precipitating areas. A neural network is used for this purpose. We discuss training this neural network using a million-point data set, and accounting for the fact that even this data set is necessarily incomplete.**

I. Introduction

From the point of view of automated applications operating on weather data, echoes in radar reflectivity may be contaminated. These applications require that echoes in the radar reflectivity moment correspond, broadly, to "weather". By removing ground clutter contamination, estimates of rainfall from the radar data using the National Weather Service (NWS) Weather Surveillance Radar-Doppler 1998 (WSR-88D) can be improved [1], [2]. A large number of false positives for the Mesocyclone Detection Algorithm [3] are caused in regions of clear-air return [4]. A hierarchical motion estimation technique segments and forecasts poorly in regions of ground clutter [5], [6]. Hence, a completely automated algorithm that can remove regions of ground clutter, anamalous propagation and clear-air returns from the radar reflectivity field would be very useful in improving the performance of other automated weather algorithms.

For a good review of the literature on ground clutter contamination, the interested reader is refered to [7]. Local neighborhoods in the vicinity of every pixel in the three weather radar moments were examined by [2] and used for automated removal of non-precipitating echoes. They achieved success by examining some local statistical features (the mean, median, and standard deviation within a local neighborhood of each gate in the moment fields) and a few heuristic features. [7] introduced the "SPIN" which is the fraction of gate-to-gate differences in a 11x21 local neighborhood that exceed a certain threshold (2dBZ in practice) to the total number of such differences. [2] introduced the "SIGN", the average of the signs of the gate-to-gate difference field within the local neighborhood. [7] used a decision tree to classify pixels into two categories – precipitation and non-precipitating while [2] used a fuzzy rule base using features that included the SPIN feature introduced by [7]. In addition to these elevation-based features, some vertical-profile features were also used – the maximum height of a 5dBZ echo was used by [7]. [2] discussed the use of vertical differences between the two lowest reflectivity scans.

Neural networks (NNs) have been utilized in a variety of meteorological applications. For example, NNs have been used for prediction of rainfall amounts by [8] and for identification of tornados by [9]. In fact, [10] attempted to solve the radar quality problem using neural networks. However, the performance of the neural network was no better than a fuzzy logic classifier (Kessigner, personal correspondence), and the neural network attempt was dropped in favor of the much more transparent fuzzy logic approach described in [2]. We propose some rationale for why our neural network approach achieves significantly better results than the network developed by [10] in Section III-A.

II. The Neural Networks

A. Inputs

Based on the extensive literature on descriptions of AP and ground clutter [7], we chose as inputs to the neural network the following: the data value, the mean, the median and the variance of each of the three moments (reflectivity, velocity, spectrum width)

[1]V Lakshmanan, Gregory Stumpf and Travis Smith are with the Cooperative Institute of Mesoscale Meteorological Studies (CIMMS), University of Oklahoma. [2]Kurt Hondl is with the National Severe Storms Laboratory, Norman, OK

at the lowest tilt of the radar. In addition, we took the same four values for the second lowest tilt of the radar. Finally, we computed some of the textural features that have been found to be useful in discriminating between precipitation and AP/GC. These were the SPIN [7], the gate-to-gate average square difference [2] and the SIGN [2]. We included the vertical gradient (difference between the reflectivities at the two lowest scans) as a separate input to the neural network.

In addition to these discriminants described in the literature, we considered a few others:

1. The maximum vertical reflectivity, over all the elevations.
2. The maximum reflectivity in the local neighborhood.
3. A weighted average of the reflectivity values over all the elevations where the weight of each data point is given by the height of that pixel above the radar. This takes into account the entire vertical profile instead of just the first two elevations.
4. The sum of all the heights at which an echo exists (reflectivity value greater than 0 dBZ) at the pixel.
5. The homogeneity of the reflectivity field defined as:

$$hom_{xy} = \frac{\sum_{i \epsilon N_{xy}} \frac{1}{1+(\frac{I_{xy}-I_i}{\overline{I_{xy}}})^2}}{card(N_{xy}) - 1} \quad (1)$$

where N_{xy} is the set of valid pixels (I_i) in the neighborhood, N_{xy}, of the pixel at (x, y) in the image, I_{xy} is the pixel value and $card(N_{xy}$ is the number of such neighbors.

6. Echo-size defined as the fraction of neighbors whose values are within 10dBZ of this pixel's reflectivity value.
7. Fraction of inflection points with inflections at 5,10 and 15dBZ thresholds. An inflection point is defined similar to the SPIN [7] except that the inflection is defined not in a polar neighborhood, but along the entire radial until that point.
8. Echo-top height defined as the maximum height of reflectivity above a certain threshold. We used both 5dBZ and 10dBZ thresholds.
9. To decorrelate the data value from the mean and median, the difference between the data value and the local mean was used.

B. Computation of Inputs

Velocity data can be range-folded (aliased). In the WSR-88D, at the lowest tilt, the velocity scan has a shorter range than the reflectivity one. We therefore divided the training pixels into two groups – one where velocity data were available and another where there was no Doppler velocity (or spectrum width) information. Thus, two separate neural networks were trained. In real-time operation, the appropriate network was invoked for each pixel depending on whether there were velocity data at that point. All the neural network inputs were scaled such that each feature in the training data exhibited a zero mean and a unit variance when the mean and variance are computed across all patterns.

Histograms of a few selected features are shown in Figure 1. It should be noted that these features are not linear discriminants by any means – it is the combination of features that gives the neural network its discriminating ability. The histogram of Figure 1d illustrates the result of several strategies we adopt during the training, so that higher reflectivities are not automatically accepted.

C. Network Architecture

We used a resilient backpropagation neural network (RPROP) as described in [11]. There was one hidden layer. Every input unit was connected to every hidden unit, and every hidden unit to the output unit. In addition, there was a short-circuit connection from the input units directly to the output unit, to capture any linear relationships i.e. the network was "fully connected" and completely "feed-forward". Every hidden node had a "tanh" activation function, chosen because of its signed range. The output unit had a sigmoidal activation function: $g(a) = (1 + e^{-a})^{-1}$ so that the outputs of the networks could be interpreted as posterior probabilities [12]. Each non-input node had, associated with it, a bias value which was also part of the training.

The error function that was minimized was a weighted sum of the cross-entropy (which [12] suggests is the best measure of error in binary classification problems) and the squared sum of all the weights in the network:

$$E = E_e + \lambda \Sigma w_{ij}^2 \quad (2)$$

The first term is a variation of the cross-entropy error suggested by [12] and is defined as:

$$E_e = -\sum_{n=1}^{N} c^n (t^n ln y^n + (1 - t^n) ln(1 - y^n)) \quad (3)$$

where t^n is the target value of the nth training pattern (0 if non-precipitating and 1 if precipitating) while y^n

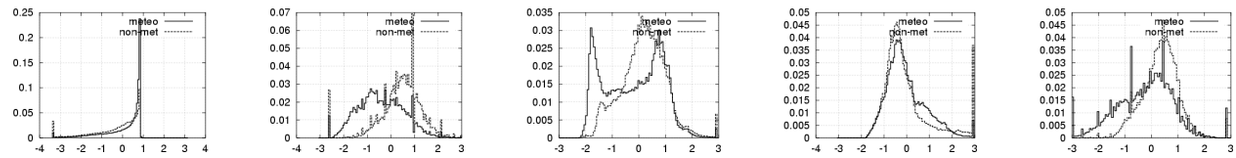

Fig. 1. Histograms of selected features on the training data set, after the features have been normalized to be of zero mean and unit variance. (a)Homogeneity (b) Radial inflections (c) Mean spectrum width (d) Mean reflectivity (e) SPIN. Note in (d) that, as a result of careful construction of the training set and selective emphasis, that the mean reflectivity histograms are nearly identical – this is not the apriori distribution of the two classes since AP is rare, and clear-air return tends to be smaller reflectivity values.

is the actual output of the neural network for that pattern input. N is the total number of patterns. The cost, c^n, captures the importance of that pattern. The second, square weights, term attempts to reduce the size of the weights, and thus improves generalization [13]. The relative weight, λ, of the two measures is computed every 50 epochs within a Bayesian framework with the assumption that the weights and the errors have Gaussian distributions, such that the ratio of their variances gives a measure of how much to decay the weights [14], [12]. We started by weighing the sum-of-weights twice as much as the cross-entropy term ($\lambda = 2$), updated λ based on the distribution of the weights and errors every 50 epochs and stopped the learning process at 800 epochs. We chose the final weights of the network from the epoch at which the *validation entropy error* was minimum, as will be discussed shortly.

The with-velocity network had 22 inputs, 5 hidden nodes and one output while the reflectivity-only network had 16 inputs, 4 hidden nodes and one output.

C.1 Validation

A validation set can ensure a network's generalization, typically through the use of early stopping methods [12]. In the neural network literature, a validation set is also utilized to select the architecture of the neural network [15]. We used a validation set that consisted of features derived from three volume scans that exhibited AP, convection and clear-air return.

We trained each network with three different numbers of hidden nodes. For each training run, we picked the result of training at the epoch that the validation error was at its minimum (See Figure 2). Thus, we used the validation set, both to determine when to stop, and to pick the final architecture of the neural network. Other than to choose the number of hidden nodes, we did not consider any alternate network topologies since, in theory at least, a single hidden layer is enough to interpolate any continuous function to arbitrary accuracy [12].

We used a testing set, independent of the training and validation sets, as decribed in Section III, and it is this independent set that the results are reported on.

D. Training

Eight volumes of WSR-88D data were selected. They covered a wide variety of weather and no-weather scenarios. A human interpreter examined these volume scans and drew polygons using the WDSS-II display [16] to select "bad" echo regions. An automated procedure used these human-generated polygons to classify every pixel into the two categories (precipitating and non-precipitating).

The data we have is not representative of true apriori probabilities, since each of the scenarios is a rare event. Patterns are assigned different importance factors c^n (See Equation 3). It is easy to see that if the cost factors are positive integers, the cost factor can be moved out of the error equation, by simply repeating the nth pattern $c^n - 1$ times. In addition to assigning different costs, we also wished to train the network with approximately the same number of patterns in both classes. Because our dataset is necessarily incomplete, we repeat the patterns so as to have a balanced distribution of patterns at every reflectivity value. In the velocity network (a proxy for pixels close to the radar), precipitating echoes are repeated $d/20$ times while non-precipitating echoes are repeated $d/10$ times where d is the reflectivity value. Thus, AP with high-reflectivity (examples of which are hard to find when training with very few radar volumes) is emphasized as are strong reflectivity cores. In the no-velocity network, non-precipitating echoes are repeated $3d/5$ times. As can be seen from Equation 3, the repeating of patterns has the same effect as imposing a cost factor to each pattern. We are, in essence, assigning a higher cost to misclassifying high-dBZ pixels than to misclassifying low-dBZ pix-

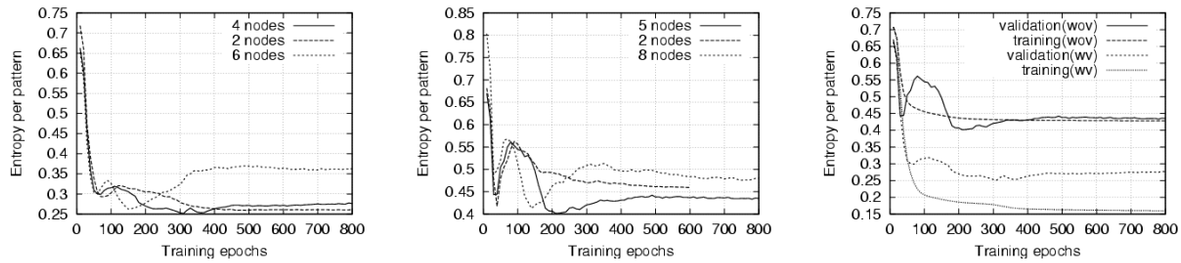

a b c

Fig. 2. Using a validation set to decide when to stop the training, and to decide on the number of hidden nodes. The y-axis is E_e/N – see Equation 3. (a) Validation error when training the without-velocity neural network. Final choice was 4 hidden nodes and the weights from the 310th epoch. (b) Validation error when training the with-velocity neural network. Final choice was 5 hidden nodes and the weights from the 210th epoch. (c) Training error vs Validation error for the final choices of hidden nodes. Note that the training error continues to decrease but the validation error starts to increase after a while, showing that the training is becoming counter-productive.

els. The histogram in Figure 1d shows the effect of this selective emphasis.

Some input vectors can be classified very easily because they are obvious. To avoid CPU cycles both in the training stage, and in the running stage, we pre-classify such pixels. Such pixels are not presented to the neural network in training, and pixels that match these criteria are pre-classified the same way in run-time as well. We discard shallow, low-reflectivity echoes and accept fast-moving and high-topped echoes.

In addition to emphasizing some pixels and pre-classifying others, we remove a third set of pixels from training altogether. In effect, we move them to an "ignore" category. These pixels are not presented to the network. The ignored pixels are those pixels for which the echo size is less than 0.2. Because of the way the echo size is defined, small echo sizes are points associated with speckle and are at the boundaries of storms where spatial statistics such as the mean and variance break down. To avoid the network expending cycles on these pixels, whose correct classification is not of paramount interest, these pixels are not part of the training at all.

In the process of training the networks, some of the computed inputs were removed and the neural network re-optimized. The probability of detection of precipitating echoes and the false alarm rates for both networks (with-velocity and reflectivity-only) were noted. If removing the input had no significant negative effect on the four statistics, the input was permanently removed.

Using this process, it was found that retaining just the mean and variance in the local neighborhood was enough – use of the median did not improve the capability of the neural network to learn the data, as measured by the probability of detection of precipitation, and the false alarm rate. We also found that the use of the maximum in the local neighborhood hurt trainability.

This pruning was not done in a rigorous manner. In particular, the numerous textural features were not pruned. We did not experiment with varying the set of features used for each moment – it is likely that we can use a different subset of features for the velocity than for the spectrum width, for example. Examination of the histograms did not yield many insights, since it is likely that it is a combination of features that possesses actual discrimination ability.

The final set of features used in the network for which results are reported were:

1. Lowest scan of velocity, spectrum width and the second lowest scan of reflectivity: local mean, local variance, difference between the data value and the mean
2. The lowest scan of reflectivity: local mean, local variance, difference between the data value and the local mean, REC Texture [2], homogeneity, SPIN [7], number of inflections at a 2dBZ threshold, SIGN [2], echo size.
3. Vertical profile of reflectivity: maximum value, weighted average, difference between data values at the two lowest scans, echo top height at a 5dBZ threshold.

During the process of training, we also discovered that one of the training cases was essentially untrainable. Rather than increase the complexity of the network, and risk a poor generalization, we chose to omit part of this data case from the training. The original reflectivity data, and the trained network's output on

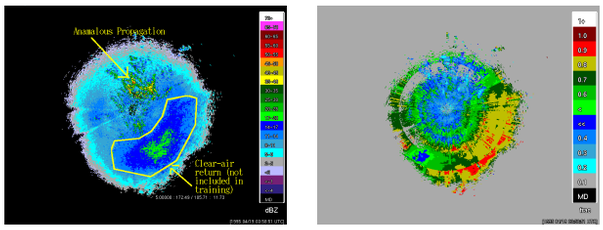

Fig. 3. Lowest scan of reflectivity from the KFWS radar at 1995/04/19 03:58:51UTC and the resulting classification of a network that included this data set in its training regimen. The network can learn to distinguish the AP, but not the clear-air return to the south-east of the radar. The unlearnable part of this volume scan (shown by the polygon) was removed from the training of the neural network.

the data, are shown in Figure 3.

Finally, to improve the robustness of the local statistics being computed, we set all pixels in the reflectivity fields which could conceivably have had a radar return (those pixels with a height below 12km) which had a radar return below the noise threshold (and was therefore set to missing) to be zero. Thus, the only missing data values correspond to atmospheric regions which are not sensed by the radar at all.

Although the neural network computes the posterior probability that given the input vector, the pixel corresponds to precipitating echoes, adjacent pixels are not truly independent. Hence, the final 2D polar grid of posterior probabilities are mean filtered, and it is this mean-field that is used to perform quality control on the radar data. If the mean-field value is greater than 0.5, the pixel is assumed to have good precipitating data, and all elevations at that location are accepted. Bad data values are wiped out en-masse, although some researchers (e.g: [7]) use data from higher elevations in such cases.

III. Results and Conclusions

A diverse set of volume scans of weather data were chosen and bad echoes marked on these volume scans by a human observer. The volume scans were processed using the trained neural network and using the Radar Echo Classifier [2]. Comparisions were made on a pixel-by-pixel basis of all pixels for which at least one of the elevations had a reflectivity value greater than zero dBZ. Performance is evaluated using the Receiver Operating Characteristics (ROC) curve [15], shown in Figure 4. In the ROC curve, the area under the curve can be taken as a measure of classifier skill (with areas above 0.5 showing considerable skill). Several thresholds are marked , so the sensitivity of classifier performance to the choice of threshold, as well as the effect of different thresholds may be gauged immediately.

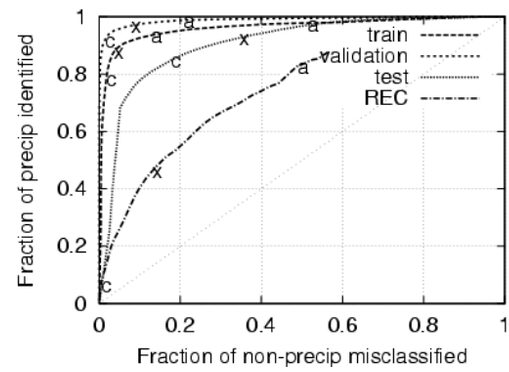

Fig. 4. A ROC curve showing the performance of the neural network on the training and testing data sets. Also shown, for comparision, is the performance of the Radar Echo Classifier. Three thresholds are marked on each of the curves – a indicates a 0.25 threshold, x a 0.5 threshold and c a 0.75 threshold. Classifiers with curves above the dashed diagonal can be considered skilled. The closer a classifier is squashed to the left and top boundaries of the graph, the better it is.

A. Comparision with Cornelius

As mentioned in the introduction, [10] utilized a neural network to solve the same radar quality problem. The network developed in this paper has a significantly better performance. The reasons probably include:

1. The choice of error function: we minimized a combination of cross-entropy and square-weights whereas [10] minimized the mean absolute error, using the cross-entropy only for stopping criteria. The cross-entropy is a better measure of performance for a classifier [12] and the use of a weight-decay allows greater generalization [13].
2. Our use of a separate validation set to determine stopping criteria, whereas [10] did not, relying instead on two measures of performance on the same data set.
3. We used 4 or 5 hidden nodes, whereas [10] with a lesser number of inputs than our network used 15 hidden nodes.
4. Our use of nearly all pixels (other than the pre-classified ones) in our data cases for training, whereas the pixels were chosen by hand or by random sampling by [10]. While a smaller selection improves training speed, the network is not trained on the full diversity of the data.
5. Our use of costs, (c_n in Equation 3) to direct the

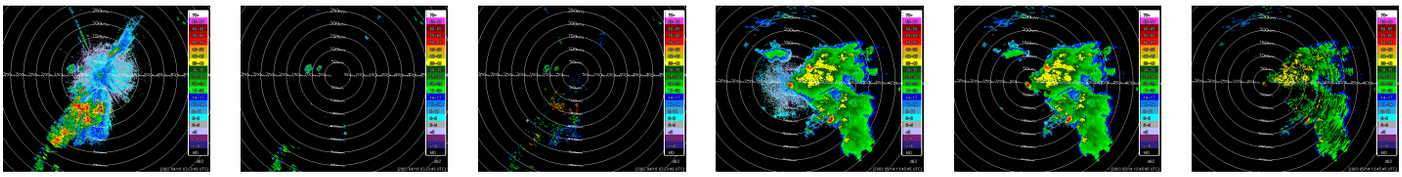

a b c d e f

Fig. 5. Testing cases: (a) A data case with significant AP (b) Edited using the neural network (c) Edited using REC. Note that some very high-reflectivity AP values remain. (d) Typical spring precipitation (e) Edited using the neural network (f) Edited using REC. Note that quite a few good echoes have been removed from the stratiform rain region.

network to expend its training where the errors are less tolerable.

In contrast, the additional local neighborhood and vertical profile features we used provide only a small, incrementatal benefit.

As can be readily seen, the neural network outperforms the fuzzy logic automated technique of [2], one of a a number of algorithms that perform similarly [17]. The first three images of Figure 5 show a case of significant AP/GC while the last three show a significant precipitation event. Looking at these images, it is possible to put the quantitative measures in context. We see that a lot of good data is misclassified by the Radar Echo Classifier. At the same time, the neural network makes its mistakes on lower reflectivity values, but gets higher reflectivity values (whether AP/GC or good data) correct more often. This is a consequence of how the network was trained.

IV. Acknowledgements

Funding for this research was provided under NOAA-OU Cooperative Agreement NA17RJ1227, FAA Phased Array Research MOU, and the National Science Foundation Grants 9982299 and 0205628.

References

[1] R. Fulton, D. Breidenback, D. Miller, and T. O'Bannon, "The WSR-88D rainfall algorithm," *Weather and Forecasting*, vol. 13, pp. 377–395, 1998.

[2] C. Kessinger, S. Ellis, and J. Van Andel, "The radar echo classifier: A fuzzy logic algorithm for the WSR-88D," in *19th IIPS Conference*, (Long Beach, CA), Amer. Meteo. Soc., 2003.

[3] G. Stumpf, C. Marzban, and E. Rasmussen, "The new NSSL mesocyclone detection algorithm: a paradigm shift in the understanding of storm-scale circulation detection," in *27th Conference on Radar Meteorology*, 1995.

[4] K. McGrath, T. Jones, and J. Snow, "Increasing the usefulness of a mesocyclone climatology," in *21st Conference on Severe Local Storms*, (San Antonio, TX), Amer. Meteo. Soc., 2002.

[5] V. Lakshmanan, R. Rabin, and V. DeBrunner, "Multiscale storm identification and forecast," *J. Atmospheric Research*, p. ??, In Press 2003.

[6] V. Lakshmanan, *A Heirarchical, Multiscale Texture Segmentation Algorithm for Real-World Scenes*. PhD thesis, U. Oklahoma, Norman, OK, 2001.

[7] M. Steiner and J. Smith, "Use of three-dimensional reflectivity structure for automated detection and removal of non-precipitating echoes in radar data," *J. Atmos. Ocea. Tech.*, no. 19, pp. 673–686, 2002.

[8] C. Venkatesan, S. Raskar, S. Tambe, B. Kulkarni, and R. Keshavamurty, "Prediction of all india summer monsoon rainfall using error-back-propagation neural networks," *Meteorology and Atmospheric Physics*, vol. 62, pp. 225–240, 1997.

[9] C. Marzban and G. Stumpf, "A neural network for tornado prediction," *J. App. Meteo.*, vol. 35, p. 617, 1996.

[10] R. Cornelius, R. Gagon, and F. Pratte, "Optimization of WSR-88D clutter processing and AP clutter mitigation," tech. rep., Forecast Systems Laboratory, Apr. 1995.

[11] M. Riedmiller and H. Braun, "A direct adaptive method for faster backpropagation learning: The RPROP algorithm," in *Proc. IEEE Conf. on Neural Networks*, 1993.

[12] C. Bishop, *Neural Networks for Pattern Recognition*. Oxford, 1995.

[13] A. Krogh and J. Hertz, "A simple weight decay can improve generalization," in *Advances In Neural Information Processing Systems* (S. H. Moody, J. and R. Lippman, eds.), vol. 4, pp. 950–957, Morgan Kaufmann, 1992.

[14] D. J. C. MacKay, "A practical Bayesian framework for backprop networks," in *Advances in Neural Information Processing Systems 4* (J. E. Moody, S. J. Hanson, and R. P. Lippmann, eds.), pp. 839–846, 1992.

[15] T. Masters, *Practical Neural Network Recipes in C++*. San Diego: Morgan Kaufmann, 1993.

[16] K. Hondl, "Current and planned activities for the warning decision support system-integrated information (WDSS-II)," in *21st Conference on Severe Local Storms*, (San Antonio, TX), Amer. Meteo. Soc., 2002.

[17] M. Robinson, M. Steiner, D. Wolff, C. Kessinger, and R. Fulton, "Radar data quality control: Evaluation of several algorithms based on accumulating rainfall statistics," in *30th International Conference on Radar Meteorology*, (Munich), pp. 274–276, Amer. Meteo. Soc., 7 2001.